

Multi-frequency, Multi-temporal, Brush Fire Scar Analysis in a Semi-Arid Urban Environment

by

Tamara Janelle Misner

B.S., University of Nebraska-Lincoln, 1998

Submitted to the Graduate Faculty of

Arts and Sciences in partial fulfillment

of the requirements for the degree of

Master of Science

University of Pittsburgh

2003

UNIVERSITY OF PITTSBURGH
FACULTY OF ARTS AND SCIENCES

This thesis was presented

by

Tamara Janelle Misner

It was defended on

December 3, 2003

and approved by

Mark B. Abbott

J. Ramón Arrowsmith

Michael S. Ramsey
(Thesis Director)

Multi-frequency, Multi-temporal, Brush Fire Scar Analysis in a Semi-Arid Urban Environment

Tamara Janelle Misner, M.S.

University of Pittsburgh, 2003

The number of forest fires has increased dramatically over the past five years in western areas of the United States, due to both human and natural causes. Urban areas, such as the city of Phoenix, continue to increase in size and population, with a majority of the development occurring in rural areas that have burned, or are threatened by brush fires. As people move into these environments there is an increased risk of damage to human property and lives due to fires. These areas have experienced a number of recent brush fires that have been expensive to fight, and caused a considerable amount of property damage. The ability to predict and control fires is thus increasingly important as urban centers encroach upon rural lands. Remote sensing can be utilized to characterize fire scarred areas, and predict areas that have an increased risk for burning again in the future. Advanced Spaceborne Thermal Emission and Reflectance Radiometer (ASTER), Landsat Thematic Mapper (TM), and Spaceborne Imaging Radar - C (SIR-C) remote sensing data have been combined with a geographic information system (GIS) to characterize fire scars in a semi-arid urban area outside of Phoenix, Arizona. This data was also used to quantify the relationship of fire scar age to vegetative recovery. In addition to the remote sensing aspect of this project, an initial geomorphological investigation was conducted to determine the effect of fire on sediment flux and landscape evolution. Detailed topographic surveys, combined with sediment trap data, were used to examine differences in erosion between burned and unburned catchments. These results have implications for potential flooding risks due to removal of vegetative cover by fires. By combining remote sensing data with a GIS database, and through comparison with geomorphic/sedimentological investigations, this work may permit city officials and urban planners to better calculate potential risks for both future fire and flood hazards within the region.

ACKNOWLEDGEMENTS

I would like to thank Dr. Michael Ramsey, for the opportunity to work on this project, for advice, and financial support. I would also like to thank my other committee members, Dr. Ramón Arrowsmith and Dr. Mark Abbott, for their contributions, time, and patience. Thanks also to Dr. Arrowsmith and his students for countless hours of fieldwork spent under the excruciatingly hot Arizona sun. Thanks to the Department of Geosciences at Edinboro University for providing lab support for grain size and total carbon analyses. Many thanks to the Department of Geology and Planetary Sciences, University of Pittsburgh, for providing technical and administrative support. Funding for this project was provided through a NASA Grant ID# NAG5-9438, and through the Department of Geology and Planetary Sciences in the form of teaching assistantships.

My gratitude goes to the following people: Eric Straffin for intellectual support, patience, encouragement, and for being my best friend; Jordan Misner for constant encouragement and late night phone calls that made sure I arrived safely home; Sally Kuhn for late night “remote sensing” discussions, practical jokes, friendship, and constant entertainment; my fellow Geology and IVIS Lab mates: Jessica Bluth, Jeff Byrnes, Sarah McElfresh, Jeff Mihalik, Shawn P. Wright, Danielle Deemer, and Nathan Stansell for friendship, technical support and encouragement; Dr. Naod Kebede (Edinboro University) for lab support; Dr. Stacey Levine (Duquesne University) for technical advice; and finally, to the Straffin family, especially Bryce, Ethan, Dean and Marita, for support and encouragement, as well as putting up with a step-mother/daughter-in-law who was often very sleepy, crabby, or all together absent for the past 2.5 years.

TABLE OF CONTENTS

INTRODUCTION	1
1.1. Remote Sensing	1
1.2. Geomorphology	3
BACKGROUND	4
2.1 Physiographic and Geologic Setting.....	4
2.2 Climate.....	6
2.2.1 <i>Precipitation</i>	6
2.2.2. <i>Temperature</i>	9
2.2.3. <i>El Niño - Southern Oscillation (ENSO)</i>	9
2.2.4. <i>Drought</i>	12
2.3 Vegetation.....	14
2.4 Fire Management.....	17
2.5 Previous Work	18
2.5.1 <i>Remote Sensing</i>	18
2.5.2. <i>Geomorphology</i>	19
METHODOLOGY	21
3.1. Fieldwork.....	21
3.1.1. <i>Field Validation</i>	21
3.1.2. <i>GPS and Spectral Measurements</i>	24
3.1.3. <i>Detailed Field Mapping</i>	28
3.1.4 <i>Sediment Transport and Erosion Monitoring</i>	28
3.2. Laboratory Analysis of Sediment Samples.....	31
3.3. Remote Sensing Data Sets	32
3.4. Data Processing.....	44
3.5. Vegetation Indices	45
3.6. Data Fusion	47
3.7. Classification.....	47
3.8. Classification Accuracy Assessment	51
3.9. Image Segmentation.....	52
3.10. Change Detection.....	52
3.11 Hazard Map.....	52
ANALYSIS & RESULTS	54
4.1 Geomorphology Results.....	54
4.2 Remote Sensing	63
DISCUSSION.....	82
5.1 Remote Sensing	82
5.2 Geomorphology	85
CONCLUSIONS AND FUTURE WORK.....	86
APPENDIX A.....	88

Appendix Title	88
BIBLIOGRAPHY	89

LIST OF TABLES

Table 1. Description of PDSI values.....	13
Table 2. Description of ASTER channels.....	32
Table 3. Description of Landsat TM 5 channels.....	33
Table 4. Grain size analysis statistics for burned catchment.	57
Table 5. Contributing area to each trap in burned catchment.	58
Table 6. Contributing area to each trap in unburned catchment.	59
Table 7. Grain size analysis statistics for unburned catchment.	59
Table 8. Percent LOI for burned and unburned areas.....	61
Table 9. Maximum likelihood classification accuracy results.....	64
Table 10. Fused data set description, and classification accuracy.....	68
Table 11. Accuracy results for decision tree classifier.	72
Table 12. Mean SAVI values for burned areas listed with unburned means for comparison.	72

LIST OF FIGURES

Figure 1. False color composite Advanced Spaceborne Thermal Emission and Reflectance Radiometer (ASTER) image of the Phoenix, Arizona valley with bands 2, 3, 1 in red, green, blue respectively.	2
Figure 2. Study area is located northeast of Phoenix Arizona.	5
Figure 3. Alluvium typically silt to pebble sized and composed predominantly of feldspars.	6
Figure 4. Phoenix is located in NOAA climate zone 6.	7
Figure 5. Average annual precipitation data, Climate Zone 6, 1900- 1989 (data from CLIMVISa).	8
Figure 6. Average annual temperature plotted with average annual precipitation, Climate Zone 6, 1896-2003 (data from CLIMVISb).	9
Figure 7. Differences in sea surface temperatures during, La Niña, normal conditions, and.	11
Figure 8. Illustrates changes in jet stream during El Niño and La Niña conditions (NOAA).	12
Figure 9. Average annual PDSI, Climate Zone 6, 1895-2003 (data from CLIMVISc).	13
Figure 10. Map of the Sonoran Desert (from Dimmit, 2000).	15
Figure 11. Stylized cross section along Upland Sonoran Desert bajada (from MacMahon, 2000).	16
Figure 12. Aerial and surface views showing vegetation type and abundance in burned versus unburned areas. Aerial photographs were collected by Dr. Ramon Arrowsmith (ASU) using a 35 mm camera attached to a weather balloon.	16
Figure 13. ASTER VNIR image, 15 m resolution with bands 3, 2, 1 in red, green, and blue respectively. GPS collected road data is overlain on this image, and the black box denotes the location of McDowell Mountain State Park showing the field site location.	22
Figure 14. Blue squares denote location of 90 by 90 meter pixel grid survey locations.	23
Figure 15. Balloon photography mosaic of Dynamite fire scar. Photos by Dr. Ramon Arrowsmith and Aaron Redman, ASU (pick up truck for scale).	24
Figure 16. GPS points that were collected to show sediment trap locations, catchment area, and survey points.	25
Figure 17. Dr. Michael Ramsey collecting ground cover spectra with the field spectrometer.	26
Figure 18. Vegetation and ground cover spectra collected with the field spectrometer. VNIR regions correspond to the spectral response regions of the ASTER VNIR data set. VNIR 1, 2, and 3 correspond to ASTER bands 1, 2, and 3 respectively.	27
Figure 19. Example of the inside of a small sediment trap, notice the mesh ramps for wildlife conservation.	29
Figure 20. Schematic example of sediment trap installation and location.	30
Figure 21. a) September 19, 2000 ASTER VNIR data set with band 3 in red, band 2 in green and band 1 in blue.	35
Figure 22. National Land Cover Data Set is derived from Landsat TM mosaics and has a spatial resolution of 30 meters.	40
Figure 23. Example vector data sets provided by ALRIS. Roads, urban areas and cities are shown.	41

Figure 24. USGS ten meter DEMs obtained from GIS Data Depotl. Four 7.5 minute USGS quadrangles were mosaiced and converted to grid files using ArcMap and ArcToolbox....	42
Figure 25. Slope mosaic of study area derived from USGS ten meter DEMs in ArcMap. Value is equal to slope measured in degrees.....	43
Figure 26. Flowchart describing image processing methodology employed in study.....	45
Figure 27. ASTER VNIR image overlain with training regions that were chosen based on field investigations.....	49
Figure 28. Average spectra for training regions over ASTER VNIR and SWIR, TIR, and SIR-C wavelengths.....	50
Figure 29. Decision Tree Tool example. White boxes represent expression or decision nodes, and colored boxes represent leaves or daughter classes.....	51
Figure 30. Contour map produced from the detailed field survey using GPS and an electronic total station illustrates the increased drainage density that is apparent in the burned area versus the unburned area.....	54
Figure 31. Average rainfall during sediment trap sampling event (data from McDowell Mtn. Park rain gauge.....	56
Figure 32. a) Sampling of large sediment trap, MMPU4, in unburned catchment. b) Sampling of small sediment trap, MMPU5, in unburned catchment.....	56
Figure 33. Grain size plot of burned catchment.....	57
Figure 34. Grain size plot for unburned catchment.....	58
Figure 35. Plot of average grain size in burned versus unburned catchments.....	60
Figure 36. Map showing the location of the regolith study transect in the burned area.....	62
Figure 37. Regolith curvature comparison for burned and unburned transects (from Arrowsmith, 2002).....	63
Figure 38. Maximum likelihood classification September 19, 2000, ASTER VNIR (bands 1-3).....	65
Figure 39. Maximum likelihood classification image of September 19, 2000 ASTER SWIR (bands 4-9).....	66
Figure 40. Maximum likelihood classification image Landsat TM (bands 1-5 & 7) September 8, 1999.....	67
Figure 41. Resulting maximum likelihood classification image of Fused data set 4 with a 9 X 9 window majority filter.....	69
Figure 42. Decision tree classification results.....	71
Figure 43. SAVI image data September 2000.....	73
Figure 44. SAVI image data September 2001.....	74
Figure 45. SAVI image data September 2002.....	75
Figure 46. ASTER Segmentation images were used to automatically outline fire scarred areas. Segmentation using ASTER near infrared.....	76
Figure 47. ASTER Segmentation images were used to automatically outline fire scarred areas. Segmentation using ASTER near infrared.....	77
Figure 48. Image segmentation using ASTER SAVI.....	78
Figure 49. Change detection image illustrates the pixels that changed class from the initial image data set to the final image data set. Green pixels were originally burned pixels that were classed as unburned desert vegetation in the 2002 image. Magenta pixels were originally burned pixels that were classed as urban in the 2002 image.....	79

Figure 50. Example hazard map with decision tree classification image overlain with road data, soil type, slope data and urban areas. Proximity of urban areas to burned areas is readily apparent. There is also an obvious lack of road coverage in the Fountain Hills area. Burned areas are more subject to future burn hazards than unburned areas. 81

INTRODUCTION

1.1. Remote Sensing

The number of forest fires has dramatically increased over the past five years in the western and southwestern areas of the United States (Grissino-Mayer and Swetnam, 2000). Some of these fires are human induced, but many are started by natural causes such as lightning strikes. Therefore, as people move into these environments there is an increased risk in damage to human property and lives. As a result, the ability to predict and control fires is becoming an increasing concern as urban centers begin to encroach on rural forest and range lands.

Previous work has mainly focused on using satellite imagery to detect fire scars and evaluate vegetation recovery in temperate and alpine ecosystems (Patterson and Yool, 1998; Jakubauskas et al., 1990). However, little work has been done to characterize fire scars in the arid southwest.

In December 1999 ASTER was launched on NASA's Terra platform. This sensor is a high-spatial resolution instrument, which collects information over multiple wavelength regions. The mission of this instrument is to gather baseline data of Earth's climate and surface conditions, and to monitor natural and manmade environmental hazards (Yamaguchi et al., 1998). Figure 1 is an ASTER image showing that recent fire scars can be easily detected using remote sensing techniques (Ramsey and Arrowsmith, 2001). Although scarred landscapes are easily identified with satellite imagery, difficulties arise where distinguishing burned areas from other landcover types (Brown, 1990; Chuvieco and Congalton, 1988; Florsheim et al., 1991). It is hypothesized that the increased spatial resolution and broader spectral range of ASTER will enable a more detailed characterization study of fire scarred landscapes, thereby increasing the accuracy of distinguishing fire scars from other land cover types.

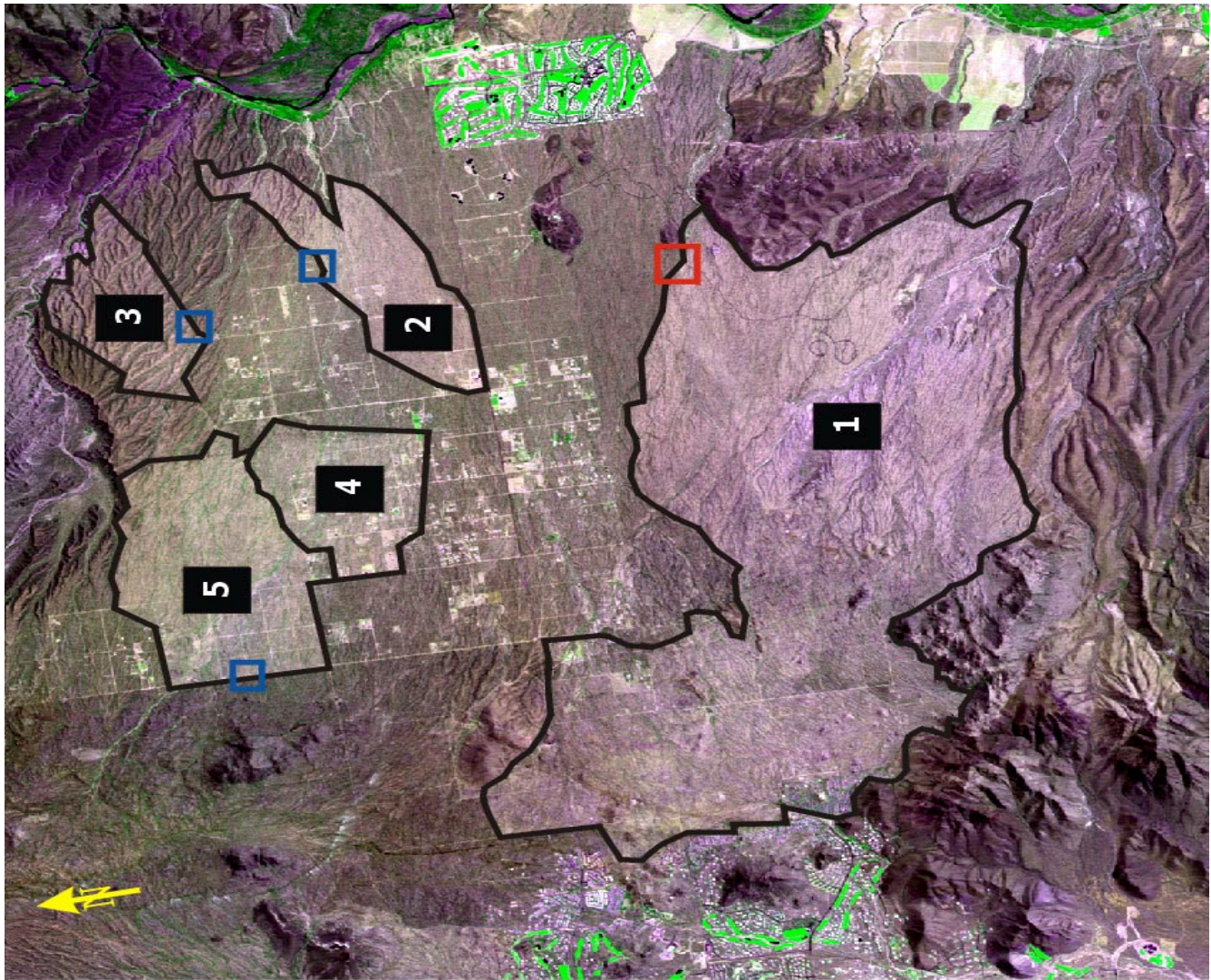


Figure 1. False color composite Advanced Spaceborne Thermal Emission and Reflectance Radiometer (ASTER) image of the Phoenix, Arizona valley with bands 2, 3, 1 in red, green, blue respectively.

This project focuses on using multispectral high resolution ASTER images as the primary data source for fire scar detection and characterization. The research presented here seeks to: (a) develop an automated classification system for detecting and characterizing fire scars in a semi-arid urban landscape using only ASTER imagery; (b) utilize data fusion techniques to increase classification accuracy; and (c) combine remote sensing data with a GIS database which can be compared with sedimentological data for future fire and flood hazard evaluation.

1.2. Geomorphology

Flooding is a potential environmental hazard following brush fires. In unburned areas, Ramsey and Arrowsmith (2001) noted a thin, fine grained, organic rich layer of sediment that is commonly associated with larger vegetation. This layer is typically eroded following a burn. Others have also noted that a decrease in vegetation and change in soil properties, as a result of burning, can lead to an increase in erosion during subsequent rainy seasons (Diaz-Fierros et al., 1987). However, little work has been done to investigate the effects of fire on semi-arid landscapes. In addition to the characterization of fire scars using remote sensing, this project conducted a preliminary investigation of landscape changes associated with burning by: (a) investigating the rate and development of channelization in response to burning; and (b) investigating the relationship between fires and sediment flux.

BACKGROUND

2.1 Physiographic and Geologic Setting

The study area is located northeast of Phoenix, Arizona (Figure 2) in the transition between Basin and Range and Central Highlands provinces (Menges and Pearthree, 1989). The area is bordered on the west by the McDowell Mountains that are a northwest-southeast trending range composed predominantly of Proterozoic metamorphic and plutonic rocks (Skotnicki, 1996). These rocks are primarily quartzites and rhyolites with minor mafic volcanics. Tertiary volcanics and conglomerates are the youngest rocks in this area. Landforms in the area are comprised mainly of alluvial fans that formed as a result of uplift and erosion of the surrounding mountains during the mid to late Pleistocene and early Holocene (Skotnicki, 1996). A majority of the alluvial deposits in the area are composed of gneissified coarse-grained granite from the northern McDowell Mountains. The alluvium is typically silt to pebble sized and composed predominantly of disaggregated feldspars (Figure 3).

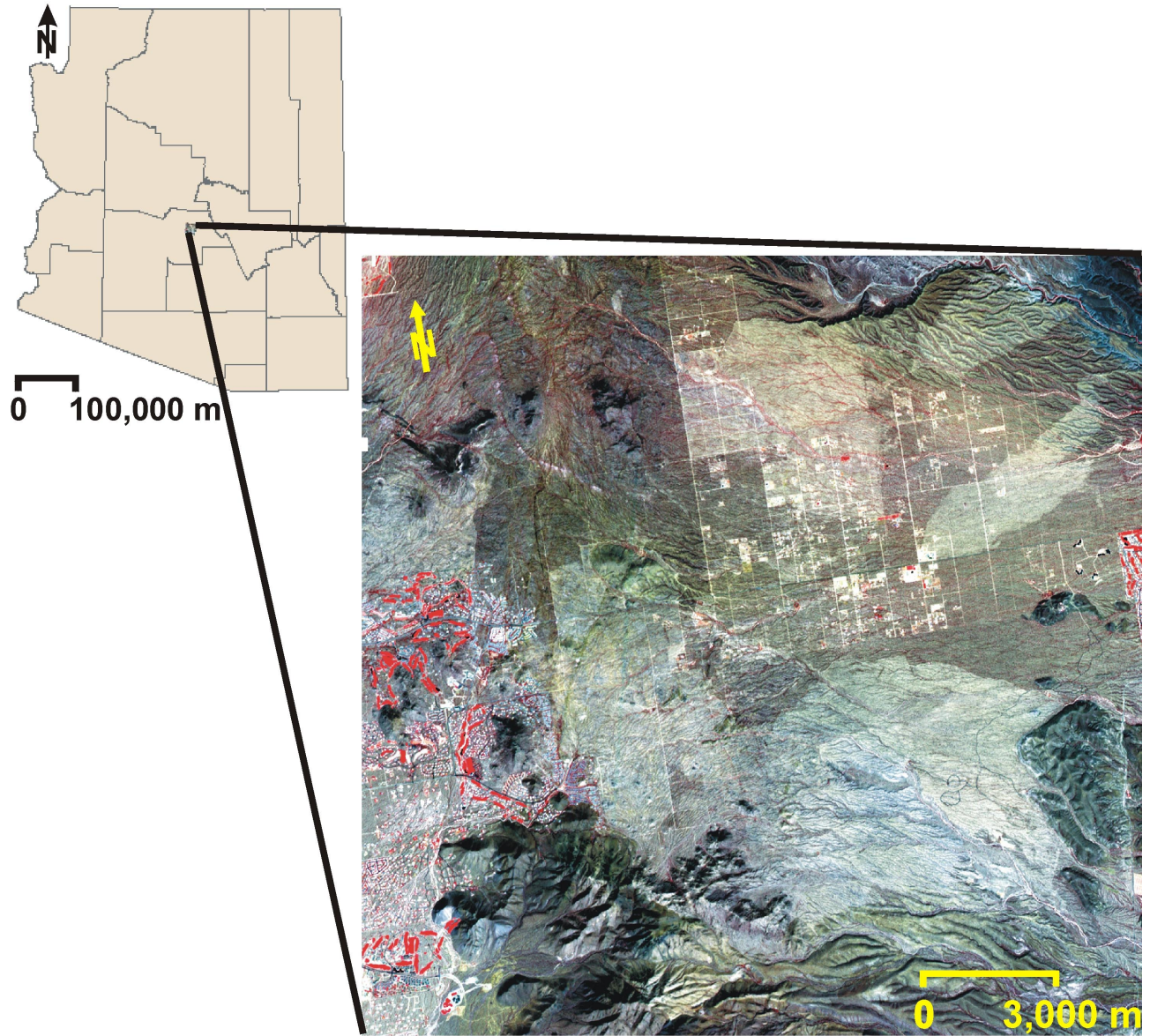


Figure 2. Study area is located northeast of Phoenix Arizona.



Figure 3. Alluvium typically silt to pebble sized and composed predominantly of feldspars.

Hendricks (1985) characterized the soils in the study area as Typic Haplargids based on soil taxonomy developed by the Natural Resources Conservation Service (NRCS). These soils occur on gently sloping (0 - 8%) valley plains and are moderately fine-textured. The mean annual soil temperature is 22° C, differing by approximately 5° C between summer and winter temperatures at the soil bedrock interface (Hendricks, 1985). The main mineral constituents of soils in the study area are quartz and feldspars (Reeves, 1999).

2.2 Climate

2.2.1 Precipitation

Arizona is divided into 7 climatological zones by the National Oceanic and Atmospheric Administration (NOAA). The study area is located in zone 6, and is considered semi-arid (Figure 4). The precipitation regime is characterized by bimodal rainfall with rainy seasons occurring from July to September and December to March. Average annual rainfall is 19.3

cm/year (Dimmitt, 2000), although rainfall intensity, variation and duration is highly variable for this area (Figure 5). Moisture is carried to Arizona by the jet stream from the Pacific Ocean, which drives the winter rainy season. Storms during the winter season are more regionally extensive and are large enough to impact even large river systems. Variables that influence rainfall intensity and duration during this time period include sea surface temperatures and changes in the jet stream (Pagano, 1999). Storms during the summer monsoon season obtain moisture from the Gulf of California and the Gulf of Mexico. These storms are extremely localized and short in duration. Variables such as ground surface temperatures and El Niño - Southern Oscillation influence storms during this season (Pagano, 1999).

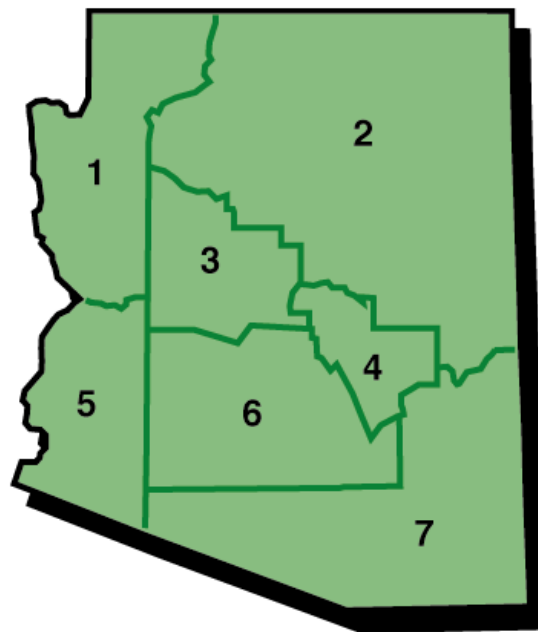


Figure 4. Study area is located in NOAA climate zone 6.

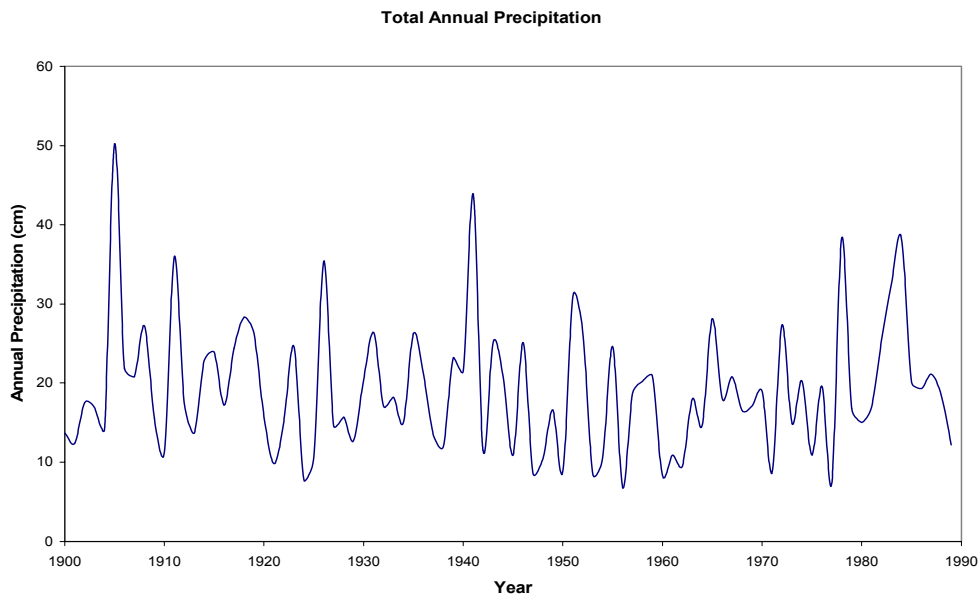
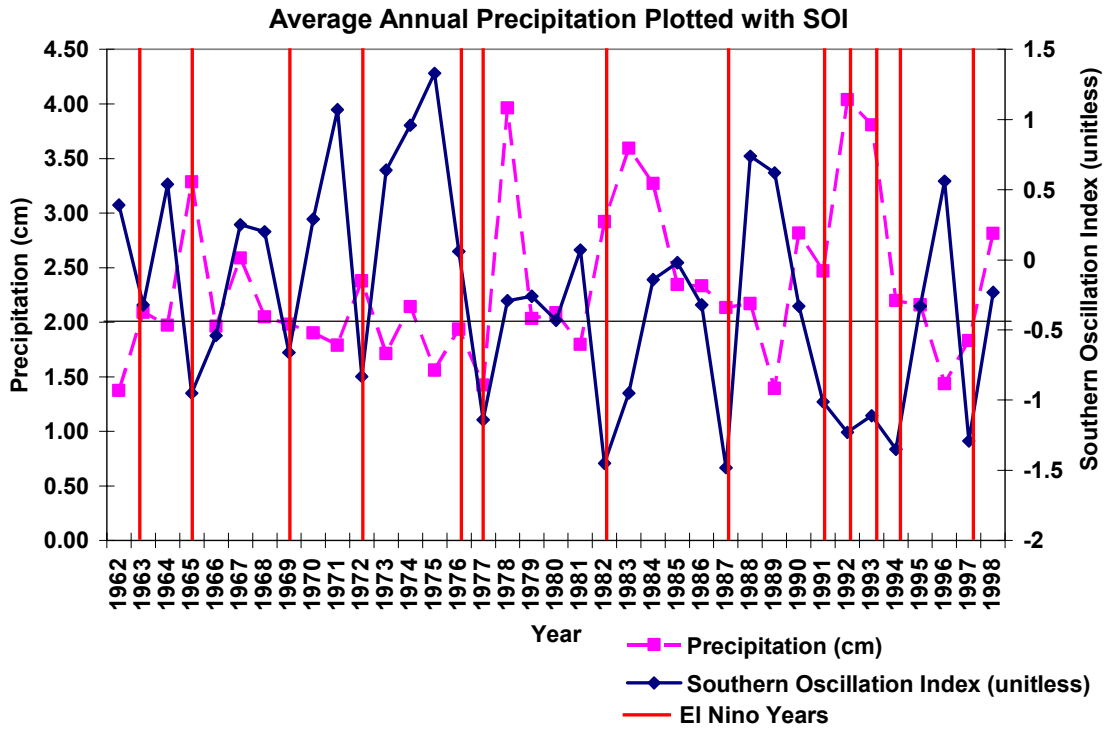


Figure 5. Average annual precipitation data, Climate Zone 6, 1900- 1989 (data from CLIMVISA).

2.2.2. Temperature

The summer season is from May to September with daytime temperatures of 30° - 40°C and night time temperatures of 10° – 20° C (Figure 6). Winter months are mild, although rare but severe frosts can occur (Dimmitt, 2000).

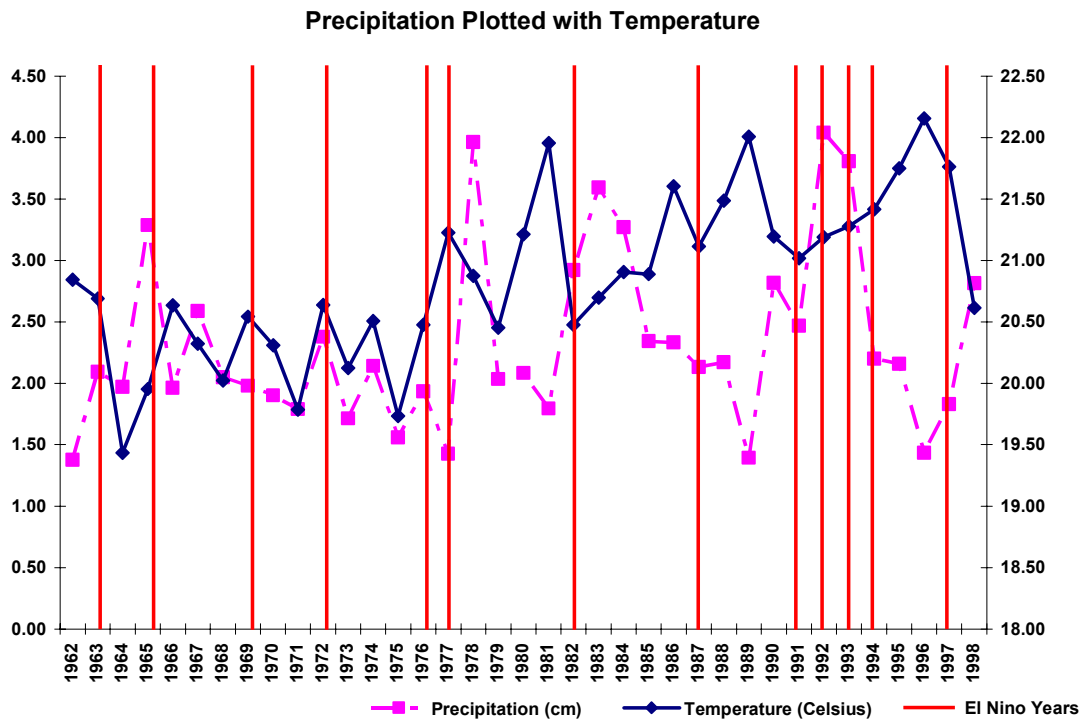


Figure 6. Average annual temperature plotted with average annual precipitation, Climate Zone 6, 1896-2003 (data from CLIMVISb).

2.2.3. El Niño - Southern Oscillation (ENSO)

The Southern Oscillation consists of two components, El Niño and La Niña. This system is commonly referred to as ENSO, El Niño Southern Oscillation. ENSO is comprised of both warm (El Niño) and cold (La Niña) sea surface temperature extremes (Figure 7). These extremes are the result of changes in atmospheric circulation in the tropical Pacific (Kousky and Bell, 2000).

The southwestern U.S. is strongly influenced by the Southern Oscillation Index (SOI), with cool and wet conditions prevailing during winter, and warm conditions dominating throughout the spring (Cook et al., 2000). During an El Niño period storm tracks are displaced further south (Figure 8). Consequently, Arizona winters are characterized by cooler temperatures and increased precipitation that is approximately 50-75% higher than during a La Niña period (Brown, 1999). This relationship is important to understand because increased precipitation promotes growth of non-native grasses, which are adapted to winter rainfall regimes. The resulting increase in these grasses leads to higher availability of fine fuels to burn (Esque and Schwalbe, 2000). During moist El Niño periods, and due to high suppression fire policies, growth of invasive grasses increases fuel loads. Consequently, during subsequent dry La Niña periods the probability of intense fires increases.

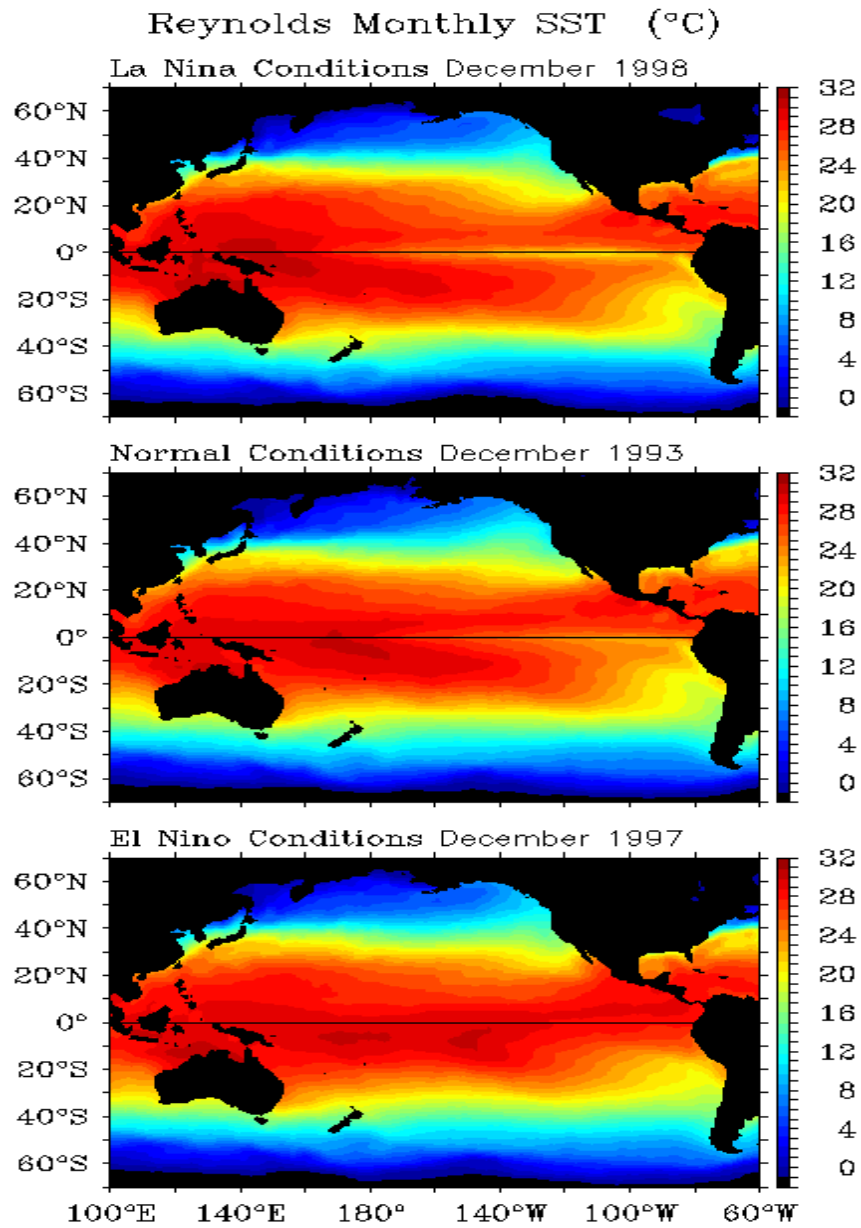


Figure 7. Differences in sea surface temperatures during, La Niña, normal conditions, and El Niño (from NOAA website <http://www.cdc.noaa.gov>).

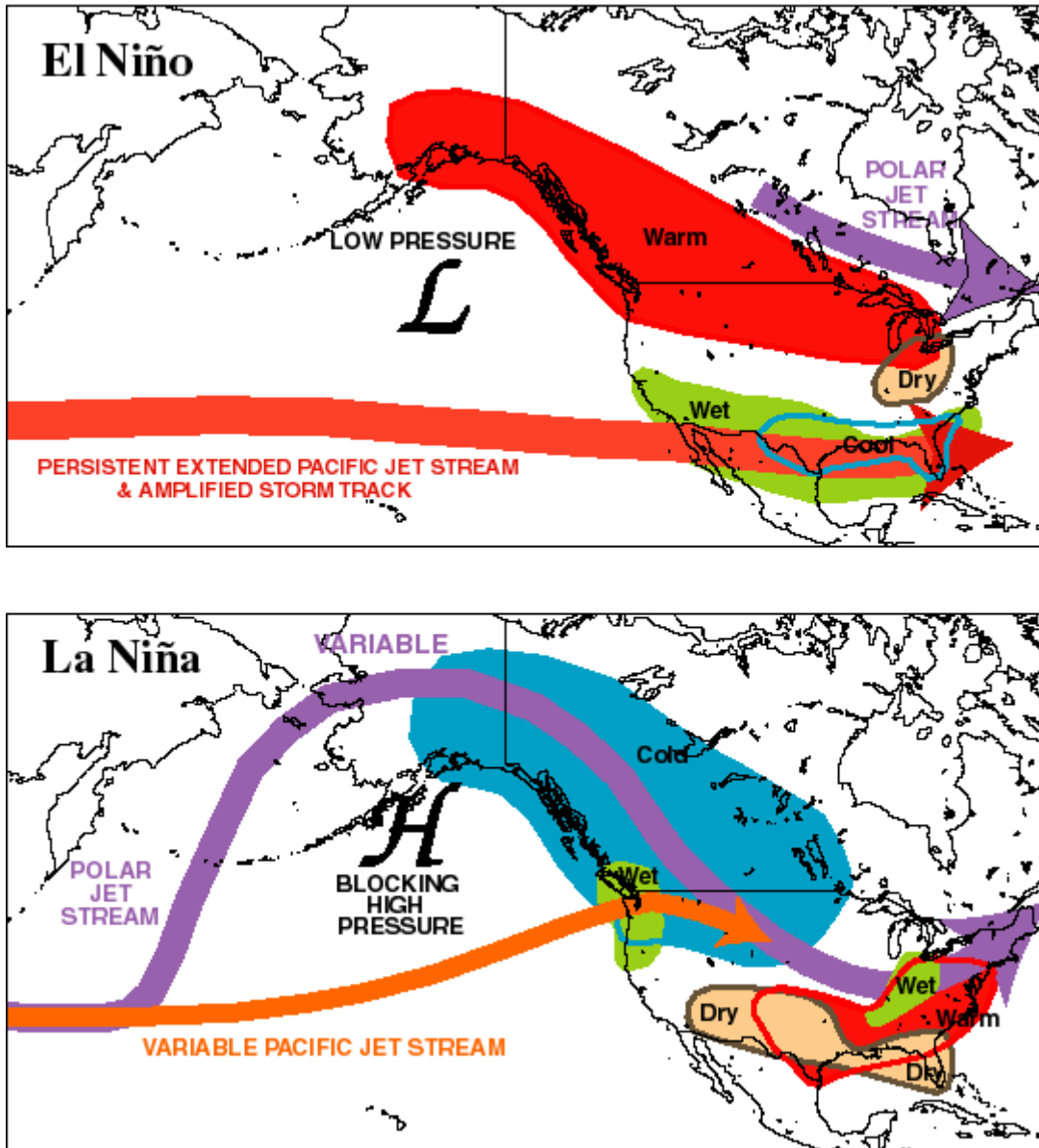


Figure 8. Illustrates changes in jet stream during El Niño and La Niña conditions (from NOAA website <http://www.cdc.noaa.gov>).

2.2.4. Drought

On average, precipitation in the study area is very low. Combined with high rates of evapotranspiration, there is significant potential for drought. Palmers Drought Severity Index (PDSI) is used to determine dryness based on combined temperature and rainfall data. Figure 9

shows PDSI values from 1895 to 2003 for NOAA’s climate zone 6, which includes the study area. Palmer index values typically range from +6.0 to -6.0, where -4.0 or less indicates extremely dry conditions (Table 1). PDSI is a useful index for predicting potential forest fire intensities based on prolonged dryness (Climate Prediction Center, 2000).

Figure 9. Average annual PDSI, Climate Zone 6, 1895-2003 (data from CLIMVISc).

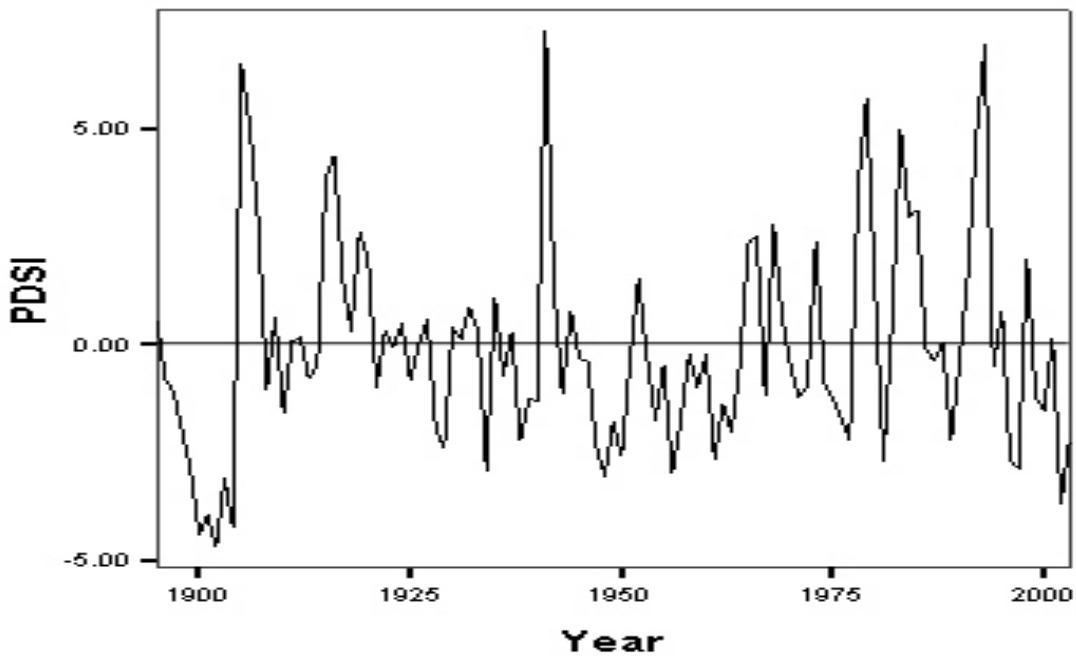


Table 1. Description of PDSI values.

PDSI Value	Description
4.00 or more	Extremely wet
3.00 to 3.99	Very wet
2.00 to 2.99	Moderately wet
1.00 to 1.99	Slightly wet
0.50 to 0.99	Incipient wet spell
0.49 to -0.49	Near normal
-0.50 to -0.99	Incipient dry spell
-1.00 to -1.99	Mild drought
-2.00 to -2.99	Moderate drought
-3.00 to -3.99	Severe drought
-4.00 or less	Extreme drought

2.3 Vegetation

Ecologically, the study area is defined as Upland Sonoran desert (Figure 10) (Dimmitt, 2000). Upland Sonoran desert vegetation is comprised of a variety of drought tolerant shrubs, thorny shrubs and cacti depending upon soil moisture content and elevation. Lower elevations are dominated by paloverde, creosote, triangle leaf bursage, jojoba, prickly pear, cholla and mesquite. The upper elevations are dominated by paloverde, ocotillo, saguaro, barrel cactus, cholla, white thorn and brittlebush (Figure 11). Blue paloverde is common in drainages and mesquite is very abundant on the broader alluvial plains (Dimmitt, 2000). In general, vegetation density is sparse (Figure 12) with less than 20% perennial cover (Wentz et. al, 2002).

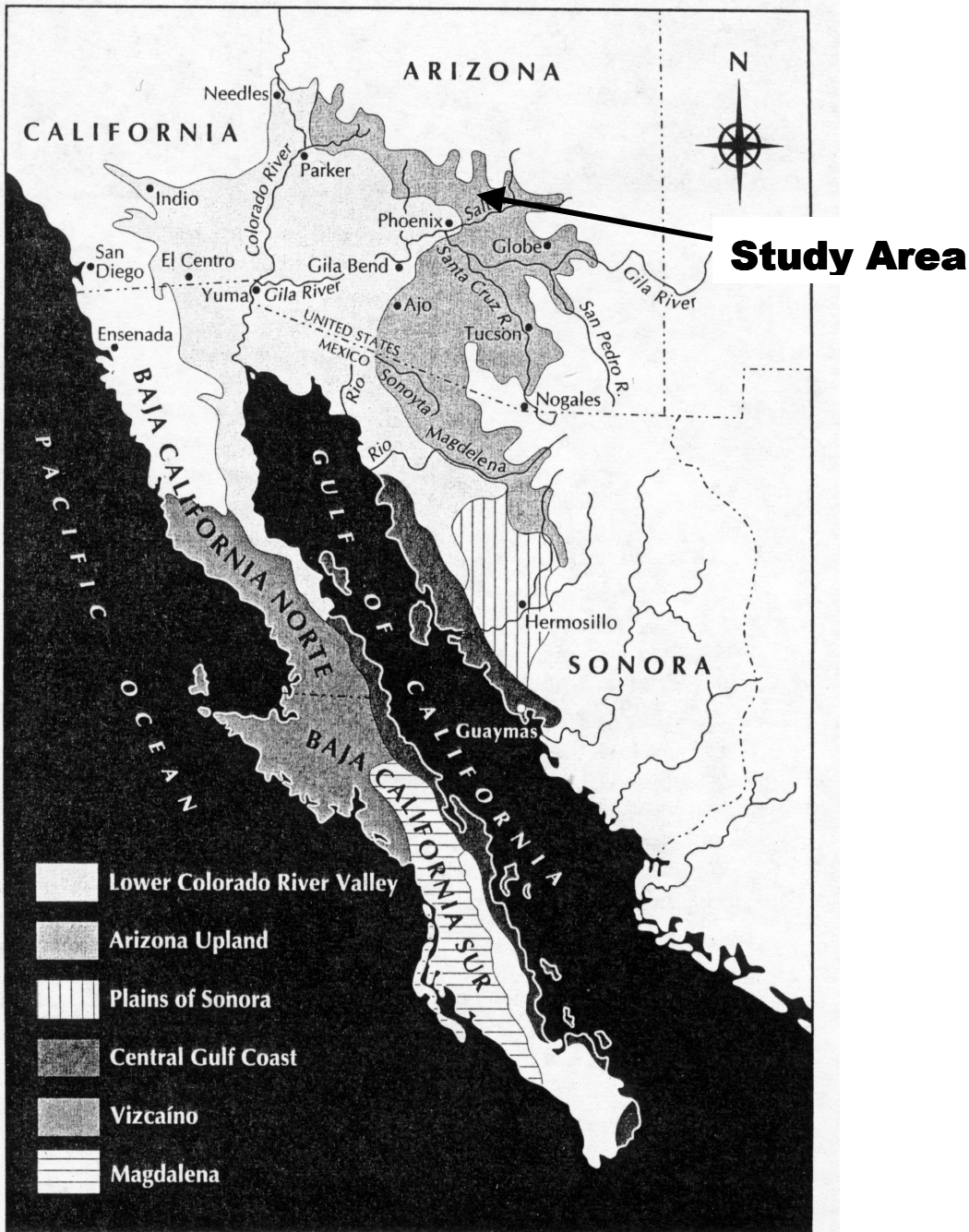


Figure 10. Map of the Sonoran Desert (from Dimmit, 2000).

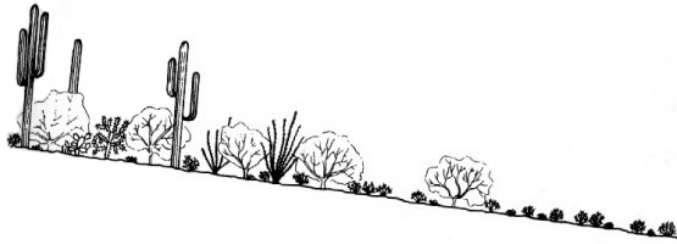


Figure 11. Stylized cross section along Upland Sonoran Desert bajada (from MacMahon, 2000).

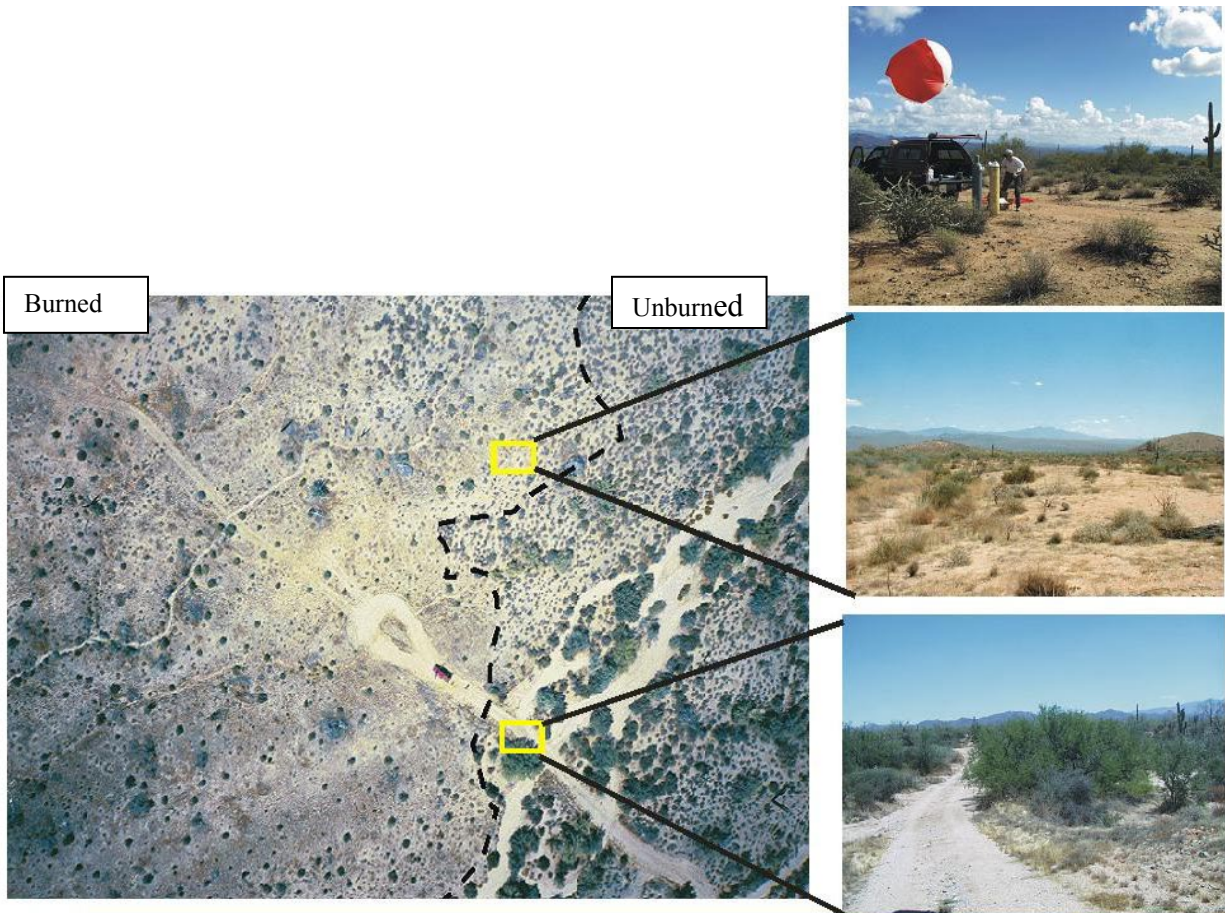


Figure 12. Aerial and surface views showing vegetation type and abundance in burned versus unburned areas. Aerial photographs were collected by Dr. Ramon Arrowsmith (ASU) using a 35 mm camera attached to a weather balloon.

2.4 Fire Management

Even though fires have occurred naturally in the study area, historically, fire is not part of floral succession for this ecosystem. Arid conditions that characterize this area result in sparse vegetation and fire intolerant plant communities (Esque and Schwalbe, 2000). In 1966 the state land department authorities adopted a fire management policy of prevention and suppression with respect to all unincorporated state and private lands. Rapid expansion of urban centers such as the Phoenix metropolitan area has increased the economic and environmental value of rural areas, resulting in aggressive fire suppression policies. Non-native or exotic grasses, such as Mediterranean Red Brome and African Bufflegass, were introduced into the Sonoran Desert by rangeland farmers for livestock. Human disturbance of rural lands combined with wet winters, dry summers and aggressive fire suppression policies have promoted the growth and spread of non-native grasses. These exotic grasses are the primary fuel for desert fires (Esque and Schwalbe, 2000). These grasses are pre-adapted to winter rainfall climates and chaparral vegetation fire regimes. They also provide enough fuel and structure to ignite surrounding desert shrubs and trees. Existing vegetation is not pre-adapted to fire, and as a result suffers considerable damage and/or mortality from burning. Once burned these exotic opportunistic grasses are able to quickly re-vegetate and invade open niches left by destruction of native flora. Re-vegetation by these invaders occurs quickly and is typically more dense than before initially burning. Once grasses become established a positive feedback process known as the grass/fire cycle begins (D'Antonio and Vitousek 1992).

Human development of rural areas also causes habitat fragmentation and soil compaction which results in weakening of the natural ecosystem and facilitation of invasions by exotic grasses. Accidental fires by people also contribute to the establishment of a grass/fire cycle in an

already weakened environment (D'Antonio and Vitousek 1992). These fire cycles are resulting in long lasting and permanent changes to the composition and diversity of vegetation in the study area (Esque and Schwalbe, 2000).

2.5 Previous Work

2.5.1 Remote Sensing

Various remote sensing techniques have been developed for use with different instruments/scanners to map fires. In the 1960's fire mapping was done with aerial infrared scanners. Isaacson et al. (1971) showed that satellite imagery was useful for quick evaluation and characterization of fire scarred landscapes. Benson (1978) later used Landsat to test satellite imagery for fire characterization. Much of the work done after 1980 to map burned and burning areas has employed medium to coarse resolution satellite sensors such as the Advanced Very High Resolution Radiometer (1.1 km resolution), the Along Track Scanning Radiometer (1 km resolution) and the Moderate Resolution Imaging Spectroradiometer (250 m – 1 km resolution).

Many techniques have been utilized to map burned landscapes using remotely sensed data sets from the above mentioned sensors. Some examples include visual analysis, density slicing, vegetation indices (Pereira, 1999), principle component analysis (Patterson and Yool, 1998), image classification routines (Barbosa et al., 1999) and multitemporal analysis (Eva and Lambin, 1998). These techniques are not sensor specific, and can therefore be used with a majority of remotely sensed data. Burned area mapping with the aforementioned techniques using moderate to coarse resolution sensors has had limited success., because there are a number of land cover types such as bare soil, urban areas and rock outcrops that are consistently confused with burned vegetation (Brown, 1990; Chuvieco, 1988; Florsheim, 1991).

Previous work has also focused on evaluating vegetation recovery and fire scar detection in tropical, temperate, and alpine ecosystems (Patterson and Yool, 1998; Jakubauskas et al., 1990). There has been little to no work done to characterize fire scarred landscapes over multiple wavelengths in semi-arid to arid environments (Barbosa et al., 1999). In addition, little work has been done to evaluate the temporal evolution of burned landscapes adjacent to urban areas.

The Central Arizona-Phoenix Long Term Ecological Research (CAP LTER) project is a National Science Foundation funded program, which has sponsored general studies of metropolitan Phoenix and its surrounding areas using spaceborne sensors such as Landsat TM and Spaceborne Imaging Radar (SIR-C). Stefanov et al. (2001) utilized Landsat Thematic Mapper (TM) data, provided by the CAP LTER program to characterize land cover classifications for the Phoenix Metropolitan area. That study integrated remote sensing data with other data sets such as land use, spatial texture and digital elevation models, to increase classification accuracy. It also resulted in the creation of land cover/land use algorithms designed to aid city officials in urban planning for this rapidly developing area.

2.5.2. *Geomorphology*

Fire is an important factor with respect to both short term and long term landscape evolution. Most previous geomorphological investigations have concentrated on the effects of fires on temperate, tropical or alpine landscapes. Little work has been done to investigate the effects of burning on channel development, runoff and sediment transport in semi-arid landscapes in close proximity to rapidly developing urban areas.

In arid regions, a number of studies have investigated runoff and erosion rates as a result of fires. Some workers determined that an increase in erosion occurs after burning, (Diaz-Fierros et

al., 1987) whereas others concluded that erosion rates slightly decrease following a fire (Lavee et al., 1995; Kutiel et al., 1995). Lavee et al. (1995) concluded the main controlling factor for erosion was fire intensity. Intense fires characteristically consume most or all of the vegetation and alter soil properties through the combustion of soil organic matter. Vaporization of organics reduces the infiltration capacity of surface sediments. These surfaces are more likely to contribute to overland flow and increased erosion shortly after burning (Garcia et al., 2000). Low to moderate intensity fires result in patchy surfaces that are characterized by partially burned plants with branches, twigs and stems contributing to surface roughness. Less intensely burned areas show little to no increase in erosion and sediment yield (Lavee et al, 1995).

The removal of vegetation and alteration of soil properties following intense fires typically results in overland flow during heavy rainstorms (Bull, 1997). Scarps of existing channels, rills and gullies are weakened by the removal of vegetation, and during rain events hillslope runoff is concentrated in these areas resulting in headward erosion, gully development, channel piracy and channel incision (Bull, 1997). Drainage density is therefore increased within the burned area by headward migration of channel scarps (Schumm,1977).

Almost all previous geomorphological investigations have concentrated on the effects of fires on temperate, tropical or alpine landscapes. This study made a preliminary effort to investigate the effects of burning on channel development, runoff and sediment transport in semi-arid landscapes in close proximity to rapidly developing urban areas.

METHODOLOGY

3.1. Fieldwork

Two successful field campaigns were completed in McDowell Mountain State Park (Figure 13) during August of 2001 and August of 2002. The following goals of the fieldwork were accomplished: (1) to perform vegetation surveys and collect balloon aerial photography for validation purposes, (2) to collect GPS and spectral measurements, (3) detailed field mapping, and (4) to monitor sediment transport and erosion.

3.1.1. *Field Validation*

In order to characterize vegetation in burned versus unburned areas, two 90 by 90 meter grid surveys were conducted, one each in a burned and unburned area (Figure 14). Each survey consisted of four transects, two from north to south, and two from east to west. At approximately 3 meter intervals, a one meter radius was visually inspected for percentage of burned/unburned vegetation component coverage. These data are used to validate the classification accuracy of the ASTER image data and fused data sets.

High spatial resolution balloon aerial photography was also collected (Figure 1 & Figure 15) for validation purposes. Photographs were collected with two 300 gram helium filled weather balloons fitted with a harness system that holds an Olympus D-340L digital camera. Refer to Arizona State University Active Tectonics, Quantitative Structural Geology and Geomorphology website for details on balloon aerial photography (<http://activetectonics.la.asu.edu/kites/balloon.html>).

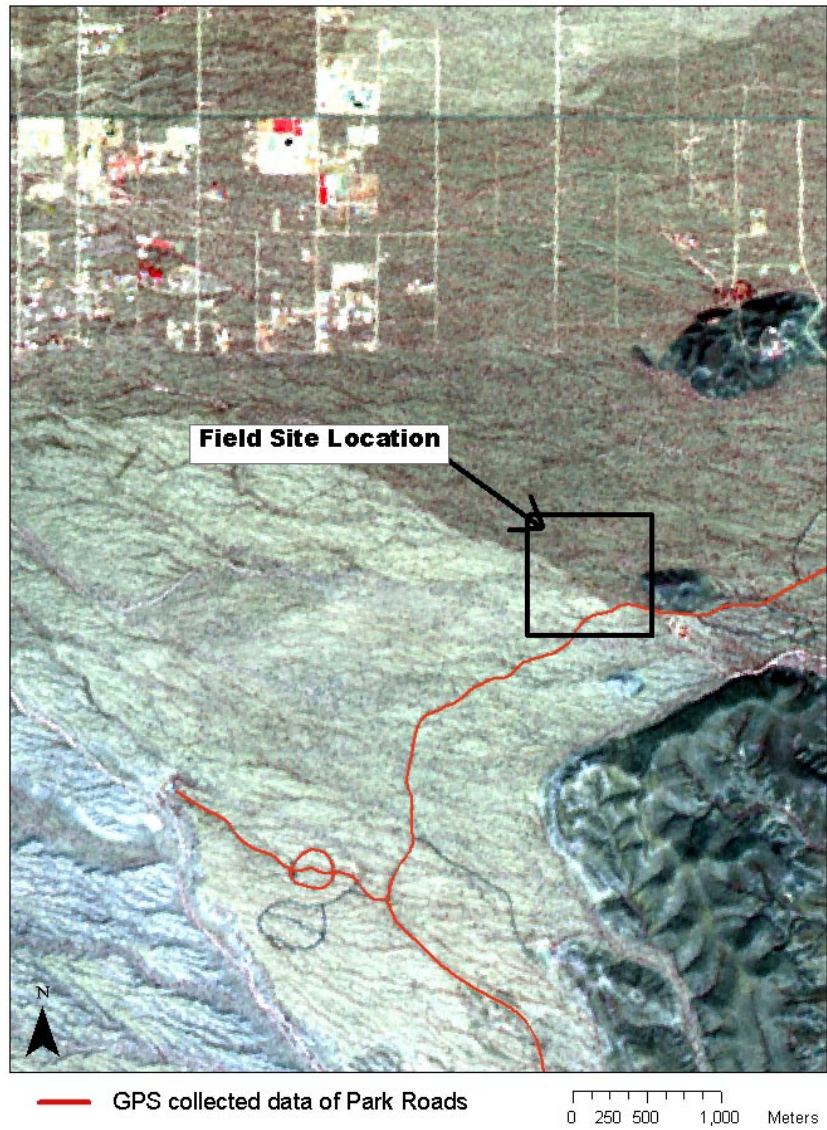


Figure 13. ASTER VNIR image, 15 m resolution with bands 3, 2, 1 in red, green, and blue respectively. GPS collected road data is overlain on this image, and the black box denotes the location of McDowell Mountain State Park showing the field site location.

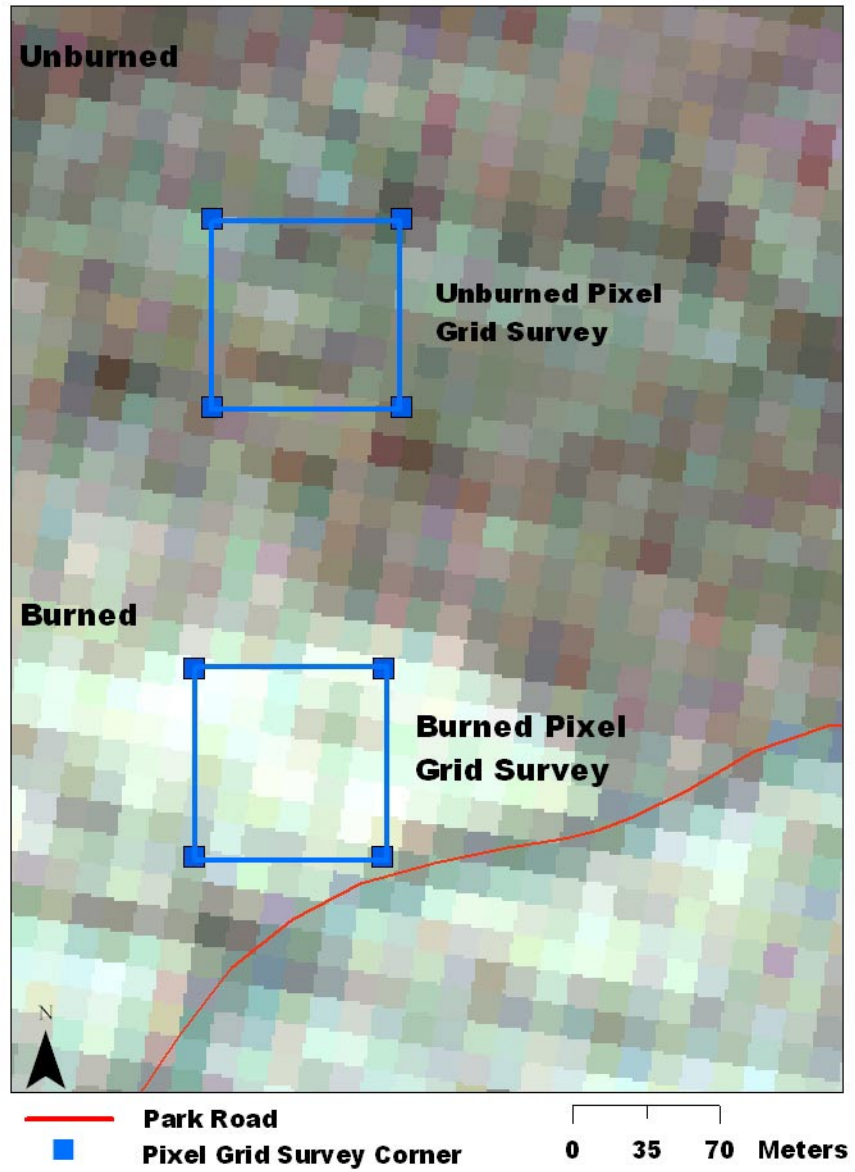


Figure 14. Blue squares denote location of 90 by 90 meter pixel grid surveys.

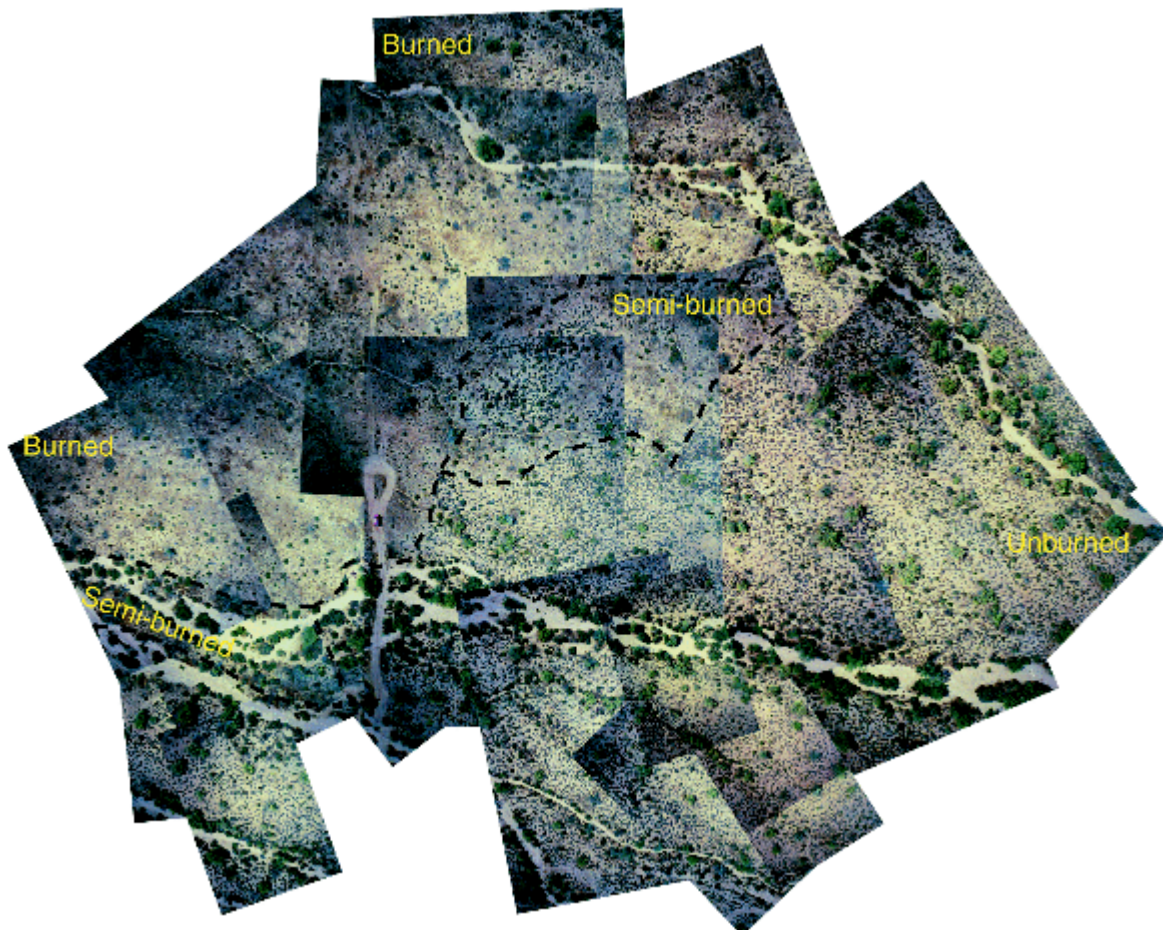


Figure 15. Balloon photography mosaic of Dynamite fire scar. Photos by Dr. Ramon Arrowsmith and Aaron Redman, ASU (pick up truck for scale).

3.1.2. GPS and Spectral Measurements

Real time differential GPS (dGPS) data were collected using a Trimble Pro XRS receiver with a TSC1 assay surveyor data logger. GPS points were collected in order to precisely map scar boundaries, locate sediment traps and other points of interest. GPS was also used to collect topographic relief information within the scars, and to navigate to anomalous areas in the image data for further investigation (Figure 16).

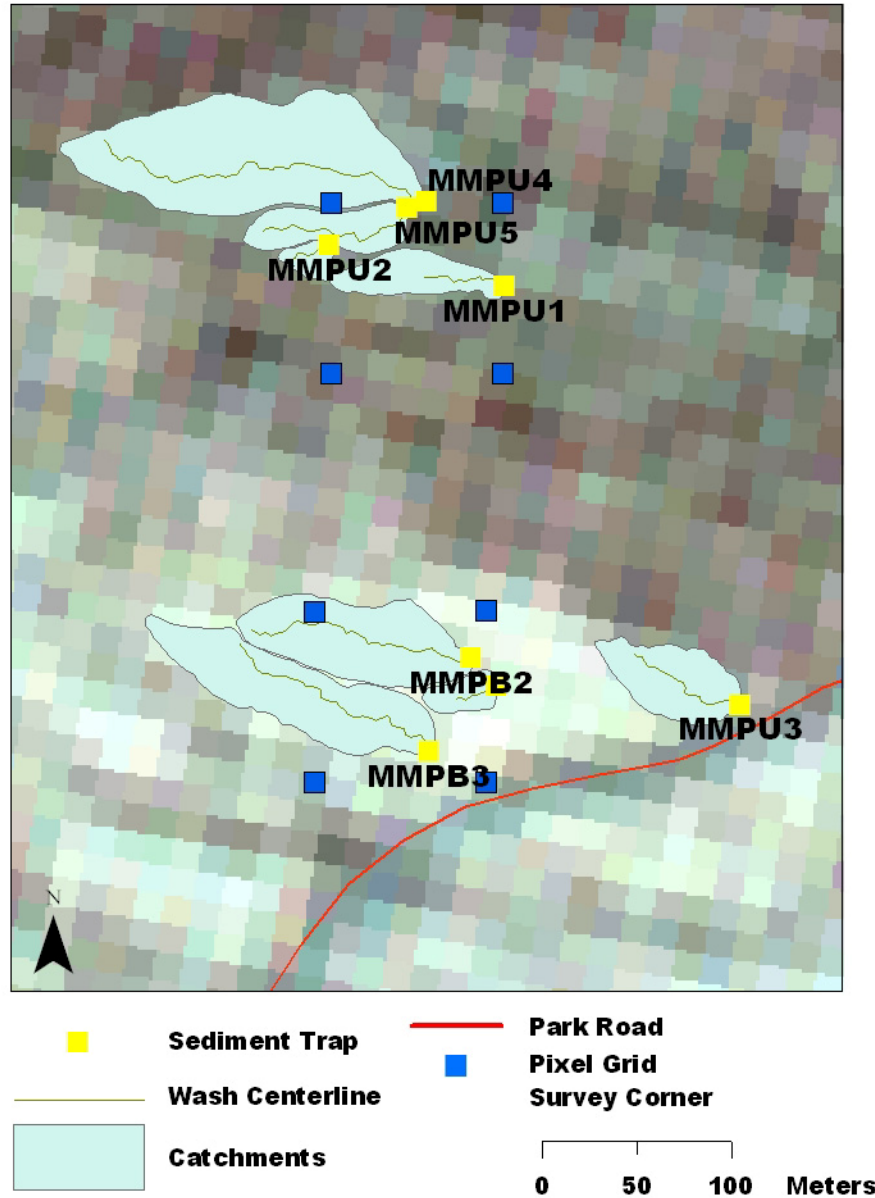


Figure 16. Collected GPS points that show sediment trap locations, catchment area, and survey points.

VNIR field spectra was collected using an Analytical Spectral Devices (ASD) FieldSpec Pro handheld portable spectrometer. The FieldSpec Pro collects information from 0.35 – 1.10 μm with a sampling interval of 0.0014 μm over the entire wavelength range (Figure 17). Spectra were obtained for various land cover components of the study area (Figure 18).

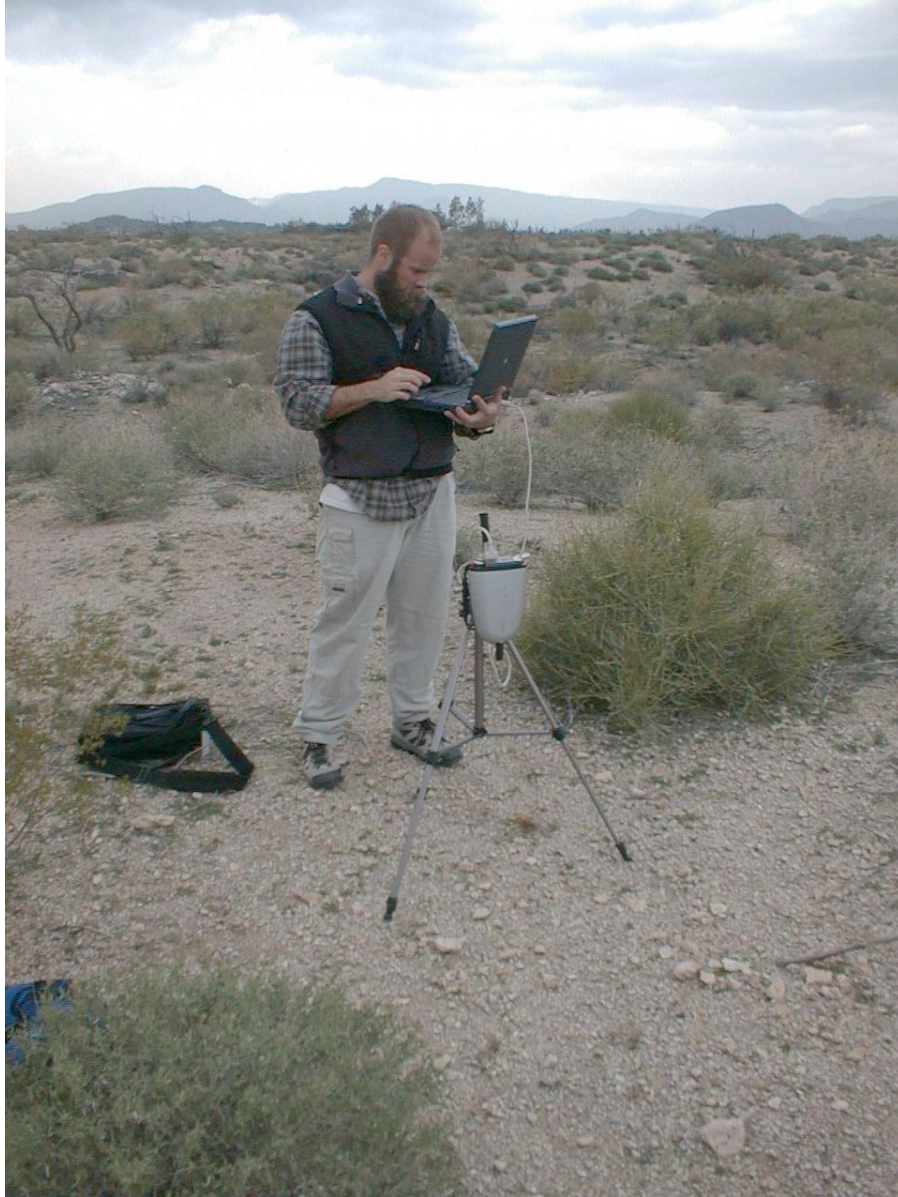


Figure 17. Dr. Michael Ramsey collecting ground cover spectra with the field spectrometer.

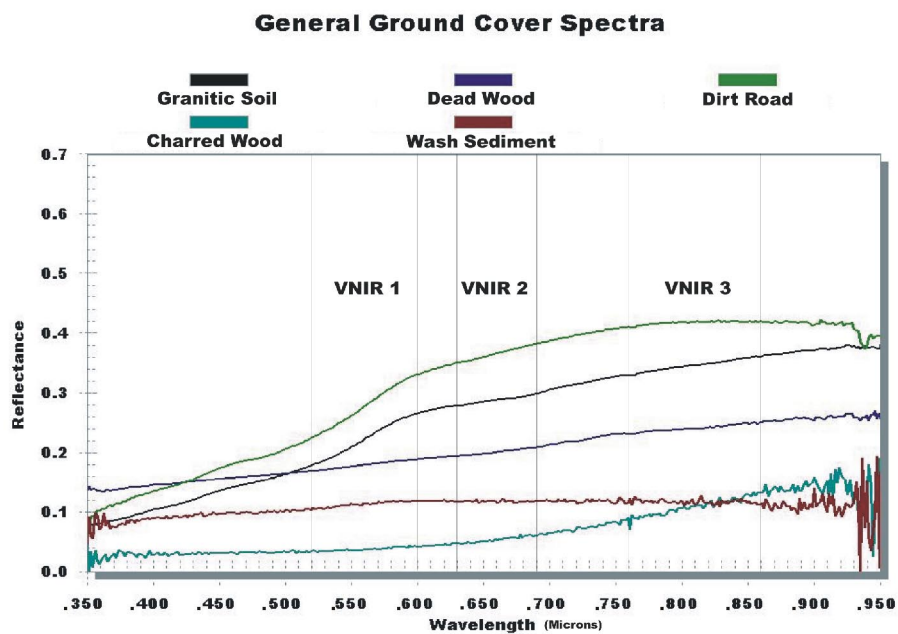
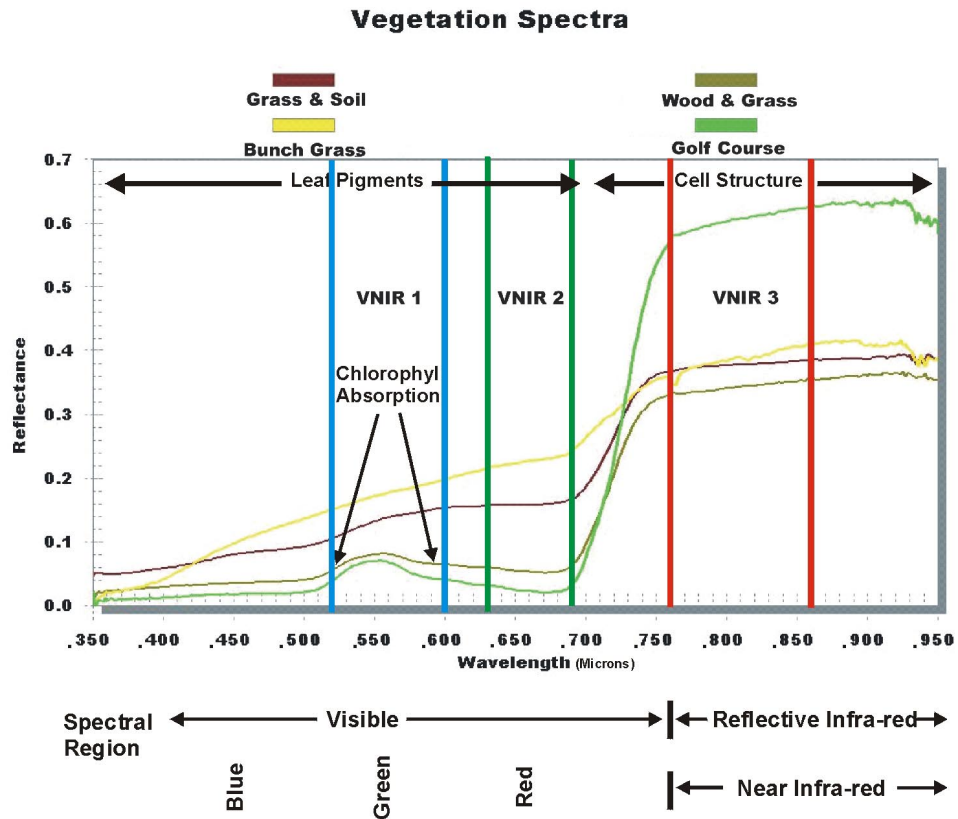


Figure 18. Vegetation and ground cover spectra collected with the field spectrometer. VNIR regions correspond to the spectral response regions of the ASTER VNIR data set. VNIR 1, 2, and 3 correspond to ASTER bands 1, 2, and 3 respectively.

3.1.3. Detailed Field Mapping

A real time kinetic (RTK) Leica GPS total station was used to conduct a small survey within a previously burned area. Points collected with the total station were used to construct a detailed map of a small drainage area bounded by burned landscape on one side and unburned landscape on the other. The purpose of this survey was to compare drainage network densities between burned and unburned catchments, and to test the ability of the equipment to compile a high resolution elevation data set..

A soil production and erosion study was performed in both the burned and unburned areas. A Leica total station surveying instrument was used with a 1 meter diameter template to survey 8 points at 50 cm radii every 45°. Surveying and sampling procedures were conducted and developed by Dr. Ramon Arrowsmith (http://kokkik.la.asu.edu/Fires_and_Floods/). Regolith samples were taken from the center point position of the survey template. Depth to regolith was determined to be the point at which the soil changed from unconsolidated to fairly or completely indurated. Curvature for each point was calculated by determining the slope (S_i) between the first four outer points, and the central point: $S_i = (H_o - H_i) / \text{dist}$, where H_o is the height of the central point and H_i is that of the i^{th} outer point. For the second set of four outer points slope was determined using the equation: $S_i = (H_i - H_o) / \text{distance}$. Once the slopes were calculated, the curvature was then calculated using the equation: $(\text{slope}(i+4) - \text{slope}(i)) / (dd(i+4) + dd(i)) / 2$.

3.1.4 Sediment Transport and Erosion Monitoring

In order to monitor sediment flux, traps were installed in both burned and unburned catchments (Figures 16, 19 & 20). Three traps, two small and one large, were installed in the burned area. Five traps, two small and three large, were installed in the unburned area. The

traps used in this project were based on a Gerlach trough design (Gerlach, 1967). They are composed of galvanized steel, and designed with lids to allow only sediment from the channel to enter. Holes were drilled into the base of each trap to prevent them from filling with water and overflowing (Figure 19). Each trap is also equipped with a ramp to allow small invertebrates to escape should they become trapped inside (Figure 19). Traps were monitored and sampled after heavy rains.

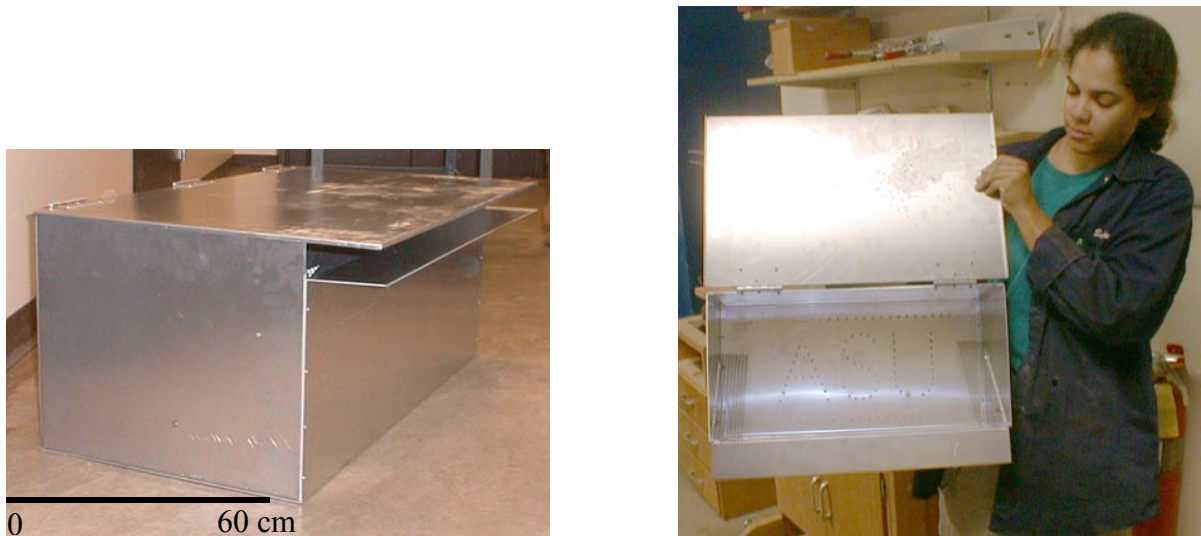


Figure 19. Side view of a large sediment trap, and the inside of a small sediment trap (notice the mesh ramps for wildlife conservation).

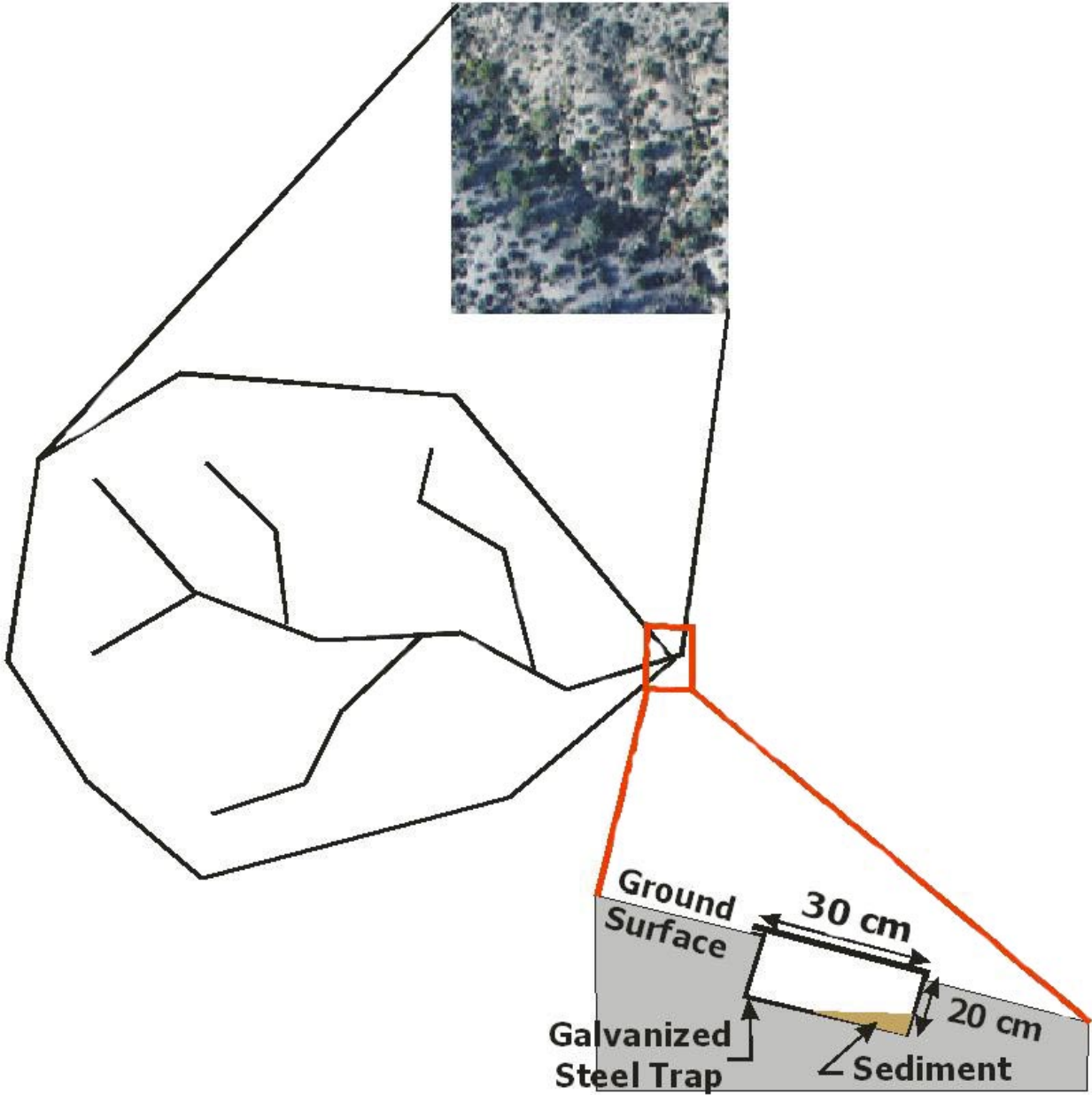


Figure 20. Schematic example of sediment trap installation and location.

3.2.Laboratory Analysis of Sediment Samples

Sediment collected from traps were analyzed for grain size and organic content in the Sedimentology Lab at Edinboro University, Edinboro, PA. The following methodology was used to prepare the samples for grain size analysis:

1. Soil aggregates were broken with mortar and pestle;
2. Samples were divided using a sample splitter;
3. Each sample was treated with H₂O₂ to remove organics;
4. Samples were dry sieved with mesh sieves into > 2 mm, 1 – 2 mm and < 1 mm size fractions;
5. Each size fraction was oven dried at 105 °C;
6. A dry weight for each fraction was obtained;
7. The < 1 mm size fraction was then analyzed for silt and clay size particles using a Coulter Counter LS Laser Diffractometer;
8. Grain size is plotted as weight percent for each sample.

Total carbon was determined by igniting each sample in a controlled muffle furnace for two hours at 550° C, and comparing pre- and post-combustion weight (Singer and Janitzky, 1986). This method is generally reproducible within 10% and has a detection limit of 0.1%. Loss on ignition is calculated based on the following equation:

$$\text{LOI (\%)} = \frac{(\text{Weight at } 105^{\circ}\text{C} - \text{Weight at } 550^{\circ}\text{C})}{(\text{Weight at } 105^{\circ}\text{C})} * 100$$

3.3.Remote Sensing Data Sets

The primary datasets used for this study were: ASTER visible near infrared (VNIR), short wave infrared (SWIR) and thermal infrared (TIR), Landsat TM 5, and SIR-C (Figure 21). ASTER is a high spatial resolution multi-spectral imager that is orbiting in a sun-synchronous polar orbit on NASA's Earth Observing System (Terra) (Yamaguchi et al., 1998). ASTER has a swath width of 60 km, and 14 bands which range spectrally from 0.5 - 12 μ m, and a spatial resolution ranging from 15 – 90 meters (see Table 2). ASTER's nominal repeat time is 16 days for all 14 bands, and up to 5 days for the 3 VNIR and SWIR bands. There are several ASTER data products available to the user community. This project focused on level 2 surface radiance and reflectance data product that was collected September 19, 2000. For more detailed information regarding the ASTER instrument refer to Yamaguchi et al.1998.

Table 2. Description of ASTER channels.

Subsystem	Band Number	Spectral Range (microns)	Spatial Resolution (m)
VNIR	1	.52 - .60	15
	2	.63 - .69	15
	3 nadir looking	.76 - .86	15
	3 backward looking	.76 - .86	15
SWIR	4	1.60 - 1.70	30
	5	2.145 - 2.185	30
	6	2.185 - 2.225	30
	7	2.235 - 2.285	30
	8	2.295 - 2.365	30
	9	2.36 - 2.43	30
TIR	10	8.125 - 8.475	90
	11	8.475 - 8.825	90
	12	8.925 - 9.275	90
	13	10.25 - 10.95	90
	14	10.95 - 11.65	90

Landsat TM 5 is a multispectral scanner with 7 channels ranging spectrally from 0.45 – 12.4 μ m and spatially from 30 – 120m resolution (see Table 3). This sensor has a sun-synchronous polar orbit with a repeat time of 16 days. The Landsat image used in this project was acquired from path 37, row 37 on September 8, 1999.

Table 3. Description of Landsat TM 5 channels.

Subsystem	Band Number	Spectral Range (microns)	Spatial Resolution (m)
Visible blue	1	0.45 - 0.52	30
Visible green	2	.52 - .60	30
Visible red	3	.63 - .69	15
Near-Infrared (NIR)	4	.78 - .90	15
Middle-Infrared (MIR)	5	1.55 - 1.75	30
Thermal-Infrared (TIR)	6	10.4 - 12.5	120
Middle-Infrared (MIR)	7	2.09 - 2.35	30

Spaceborne Imaging Radar – C (SIR-C) is an instrument that has flown twice aboard the space shuttle (Freeman et al., 1995). This instrument collects information at two radar frequencies, L-band (23 cm) and C-band (6 cm) in four polarizations (HH, HV, VH, VV). The radar image used in this project was collected on October 4, 1994.

Digital orthophoto quarter quads (DOQQs) from the United States Geological Survey (USGS) were also used for field validation purposes. These images measure 3.75 minutes longitude by 3.75 minutes latitude with a spatial resolution of 1 meter.

National Land Cover Data (NLCD) is a free data set produced by the USGS, and was obtained from the EROS data center (Figure 22). This data set is a land cover classification comprised of 21 classes derived from early to mid-1990’s Landsat Thematic Mapper data.

Vector data is information defined by points, arcs and polygons used to model locations and shapes. These data were obtained from the Arizona Land Resource Information System (ALRIS). ALRIS is run by the Administration and Resource Analysis Division of the Arizona State Land Department, and was established by the Arizona State Legislature in 1982. The goal of this agency is to provide data and support services for Arizona's GIS community. The following vector data were obtained from this source: soil type, vegetation type, urban centers, towns, city locations, roads, geology, digital elevation model and slopes (Figure 23).

Digital elevation models (DEMs) are produced by the USGS, and are derived from topographic maps. This project used four 10 meter resolution DEM's which were obtained from GIS Data Depot. A DOS program called SDTS2DEM was used to convert the SDTS formatted file to DEM format. Grid files were created from the DEM files in ArcToolbox, and ArcMap was used to create slope coverages (Figure 24). USGS DEM's were chosen over ASTER DEM's because of spatial resolution. ASTER's 30 m resolution was not adequate to model elevation changes, because slopes in the study area are very shallow, less than 10 degrees. DEM's were converted into slope coverages using spatial analyst in ArcMap (Figure 25).

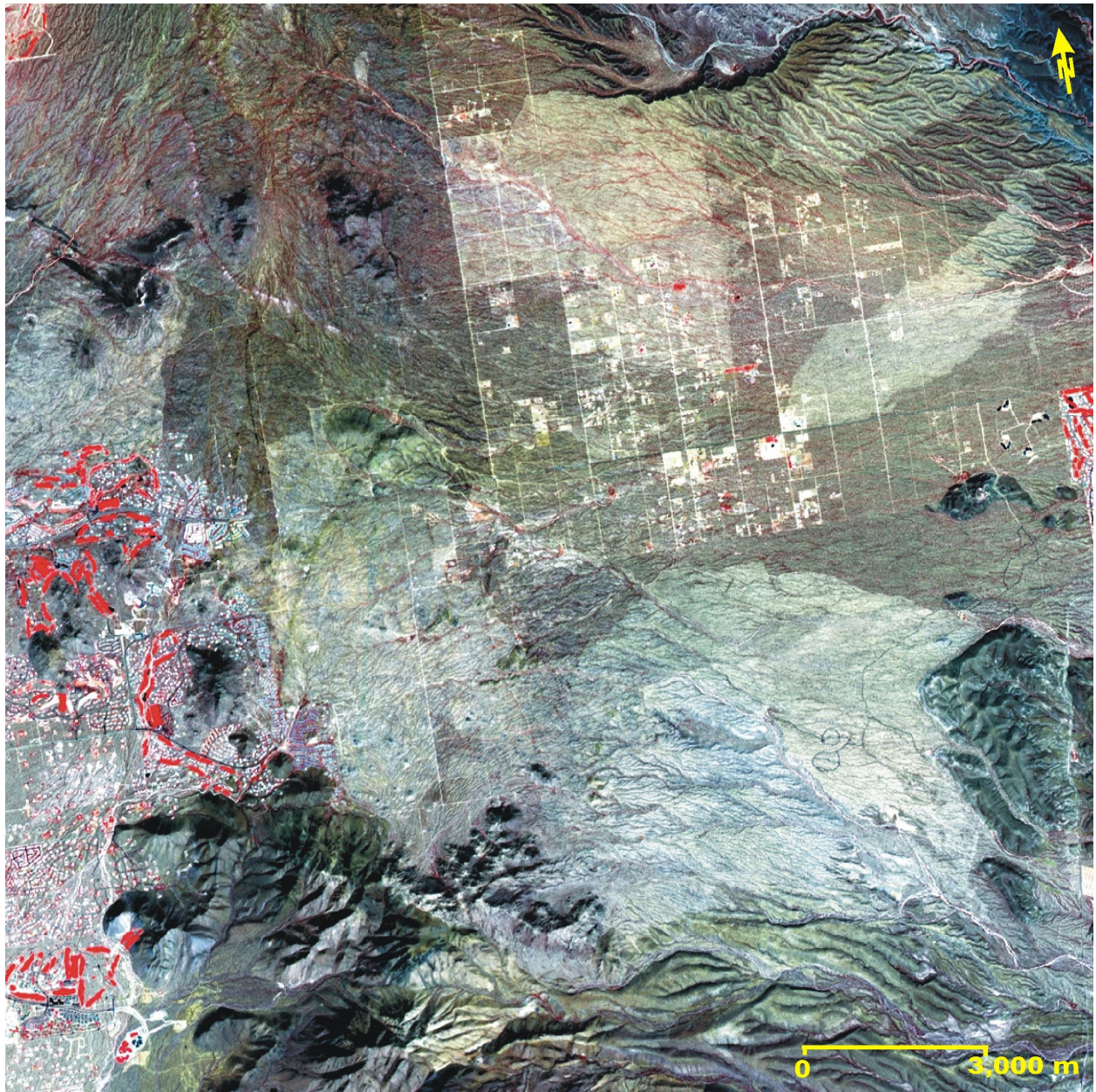


Figure 21. a) September 19, 2000 ASTER VNIR data set with band 3 in red, band 2 in green and band 1 in blue.

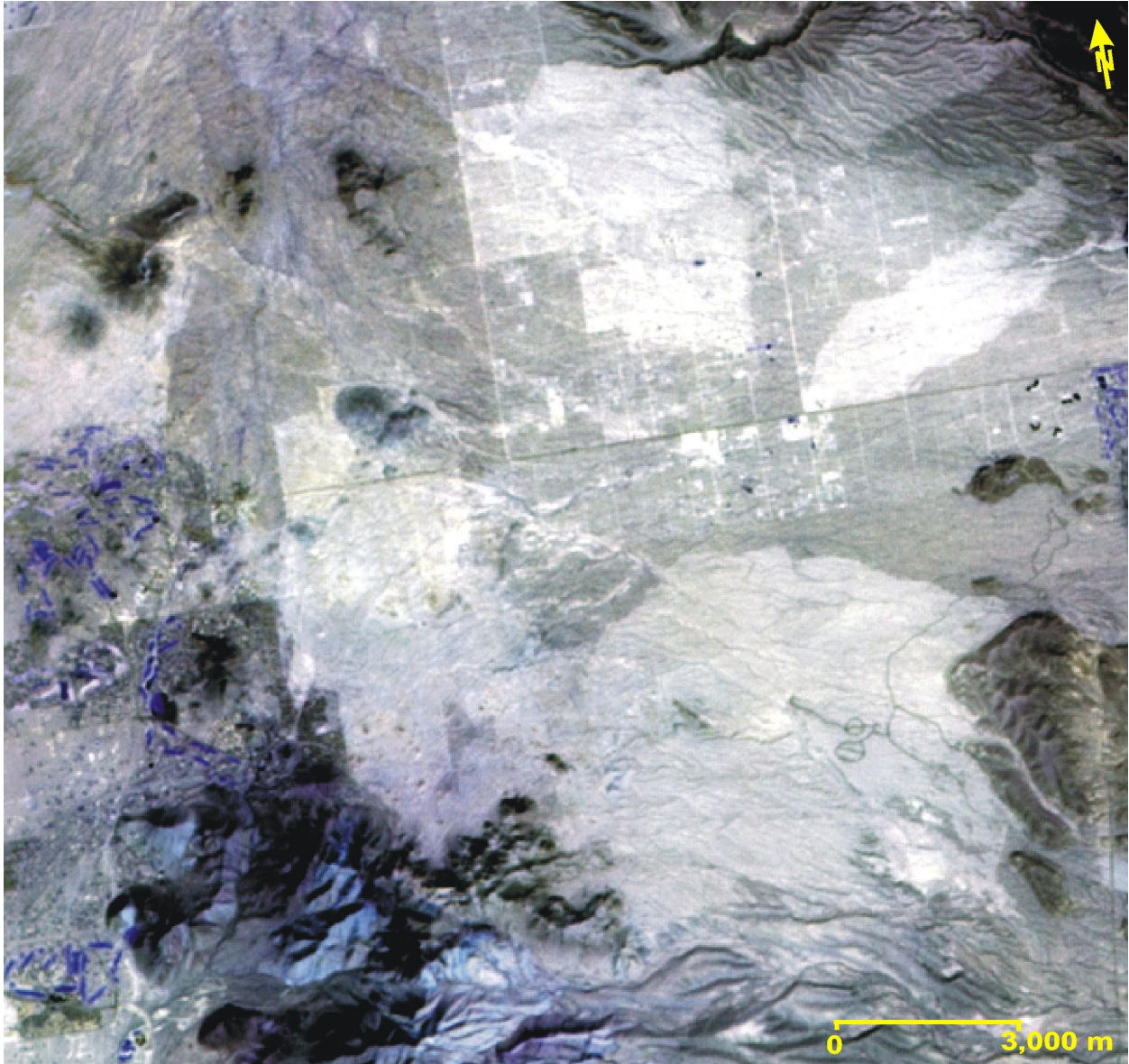


Figure 21. b) September 19, 2000 ASTER SWIR data set with band 6 in red, band 5 in green and band 4 in blue.

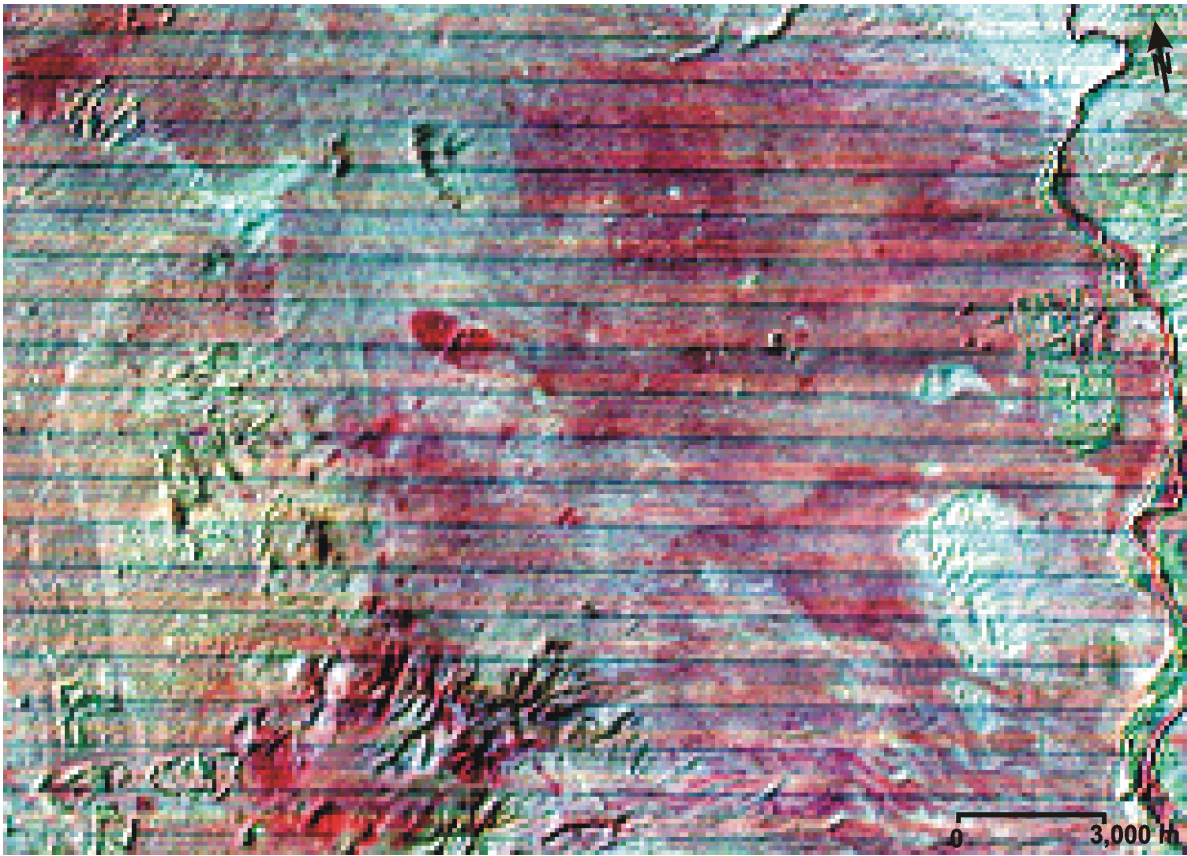


Figure 21. c) September 19, 2000 ASTER TIR data set with band 13 in red, band 12 in green, and band 11 in blue.

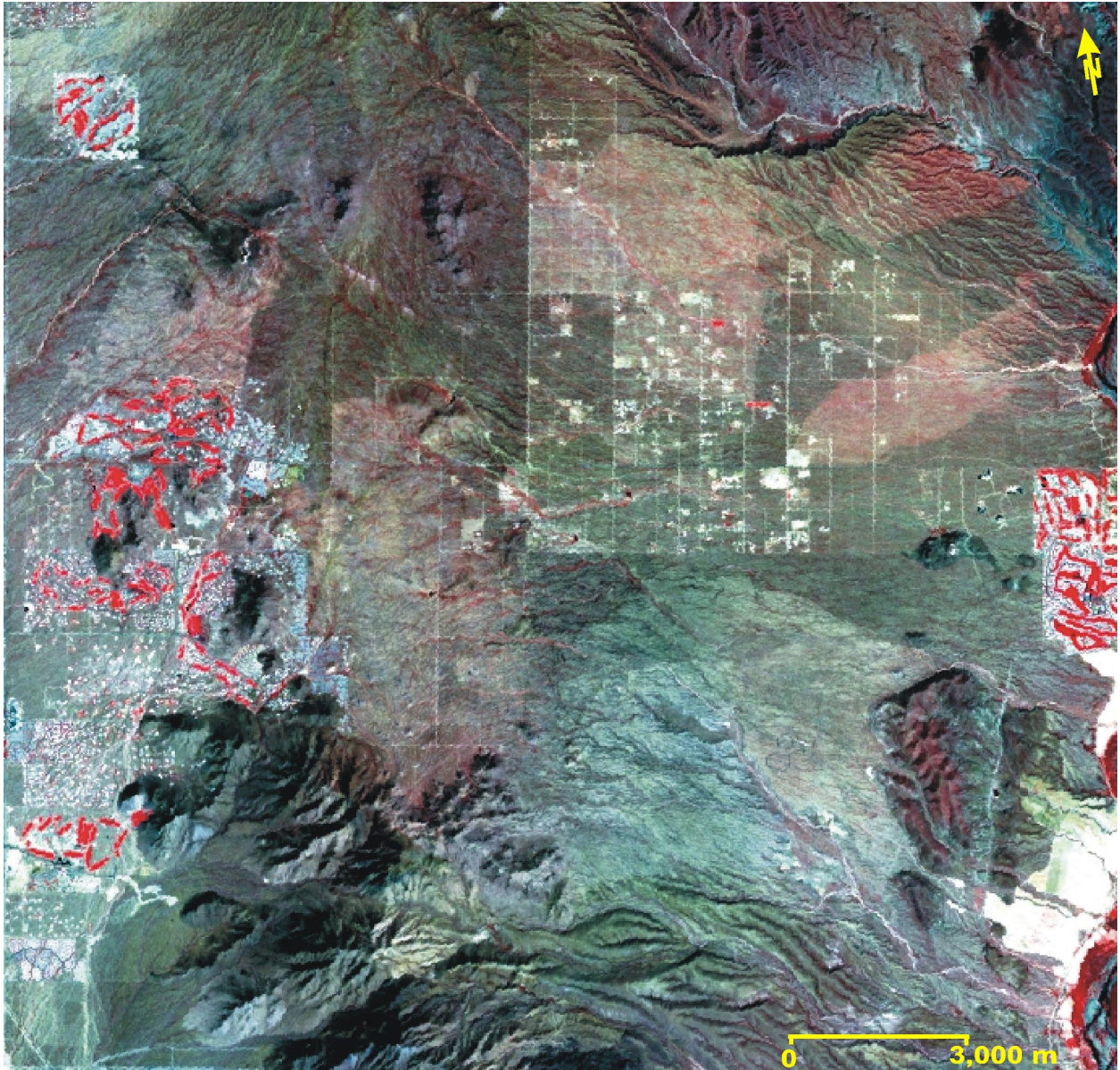


Figure 21. d) September 8, 1999 Landsat TM image with band 4 in red, band 3 in green, and band 3 in blue.

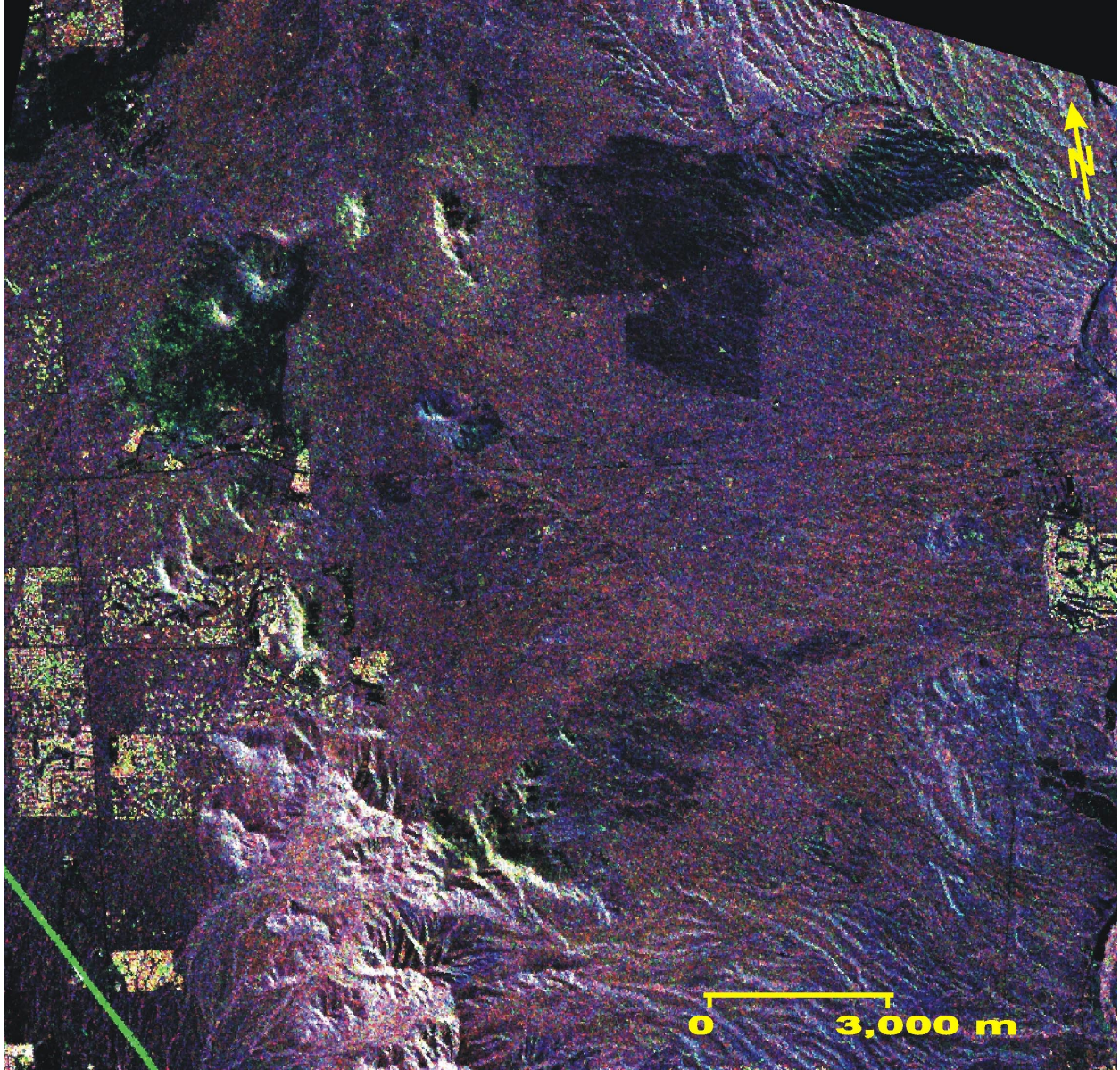
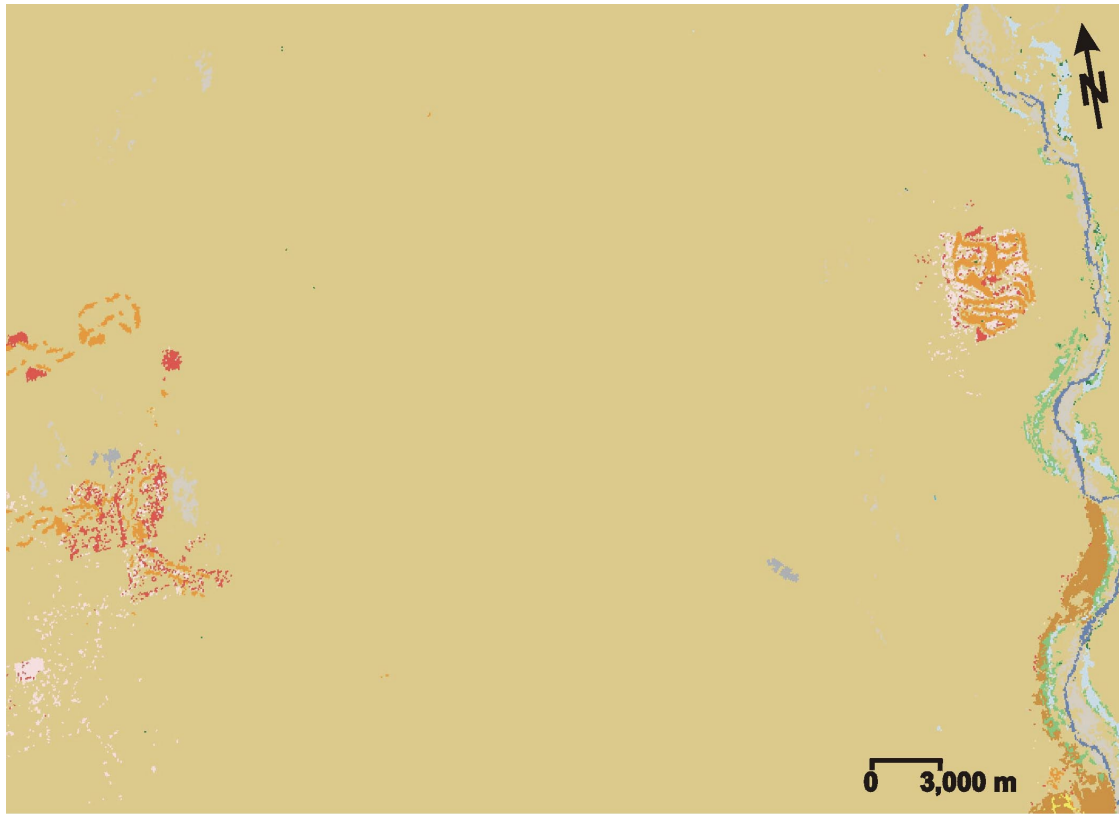


Figure 21. e) October 4, 1994 SIR-C data set with Lhv in red, Lhh in green, and Chv in blue.



National Land Cover Dataset Classification System Legend		
Color Key	RGB Value	Class Number and Name
	102, 140, 190	11 - Open Water
	255,255,255	12 - Perennial Ice/Snow
	253, 229, 228	21 - Low Intensity Residential
	247, 178, 159	22 - High Intensity Residential
	231, 86, 78	23 - Commercial/Industrial/Transportation
	210, 205, 192	31 - Bare Rock/Sand/Clay
	175, 175, 177	32 - Quarries/Strip Mines, Gravel Pits
	83, 62, 118	33 - Transitional
	134, 200, 127	41 - Deciduous Forest
	26, 129, 78	42 - Evergreen Forest
	212, 231, 177	43 - Mixed Forest
	220, 202, 143	51 - Shrubland
	187, 174, 118	61 - Orchards/Vineyards
	253, 233, 170	71 - Grasslands/Herbaceous
	252, 246, 93	81 - Pasture/Hay
	202, 145, 71	82 - Row Crops
	121, 108, 75	83 - Small Grains
	244, 238, 203	84 - Fallow
	240, 156, 054	85 - Urban/Recreational Grasses
	201, 230, 249	91 - Woody Wetlands
	144, 192, 217	92 - Emergent Herbaceous Wetlands

Figure 22. National Land Cover Data Set is derived from Landsat TM mosaics and has a spatial resolution of 30 meters.

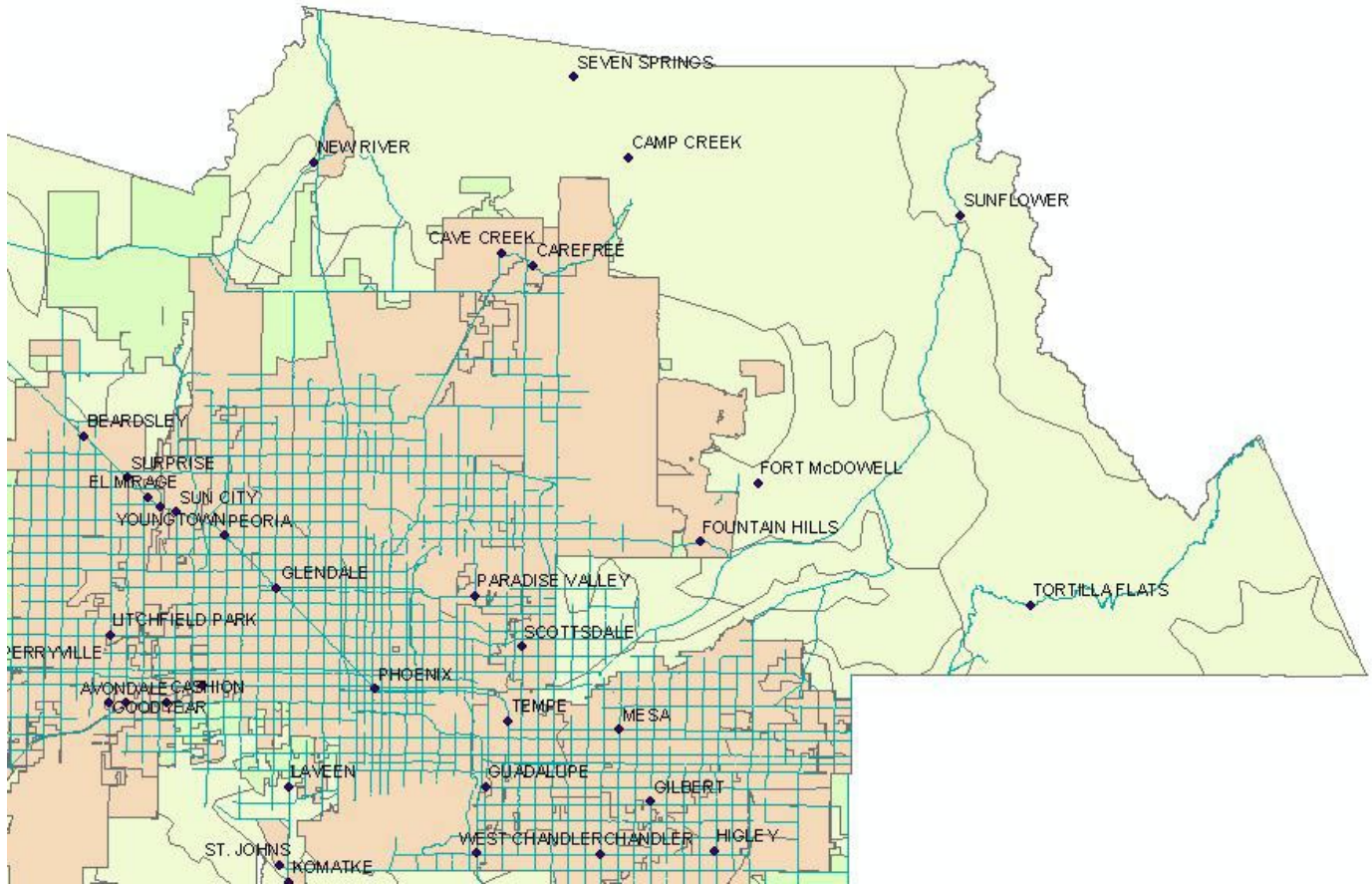


Figure 23. Example vector data sets provided by ALRIS. Roads, urban areas and cities are shown.

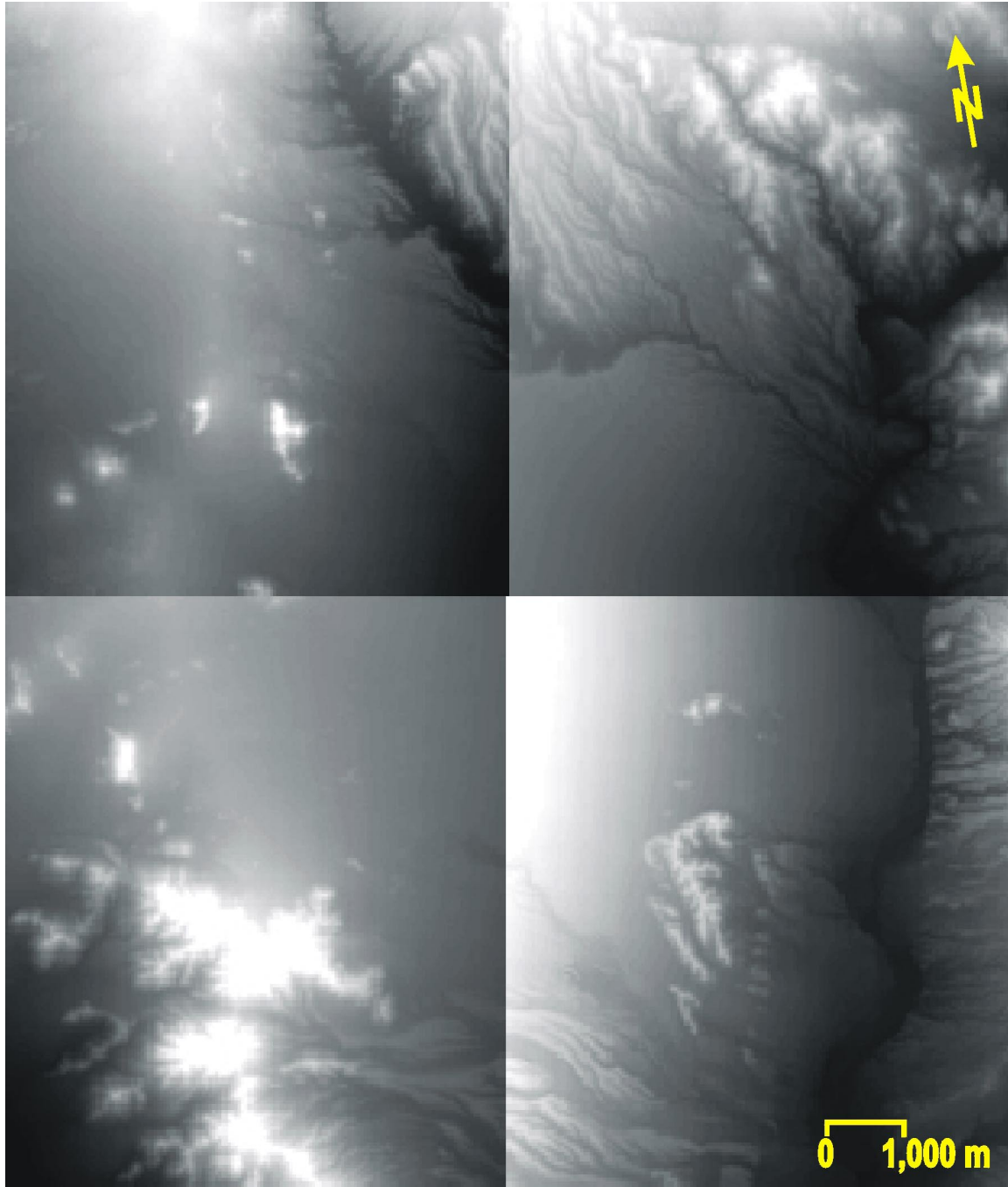
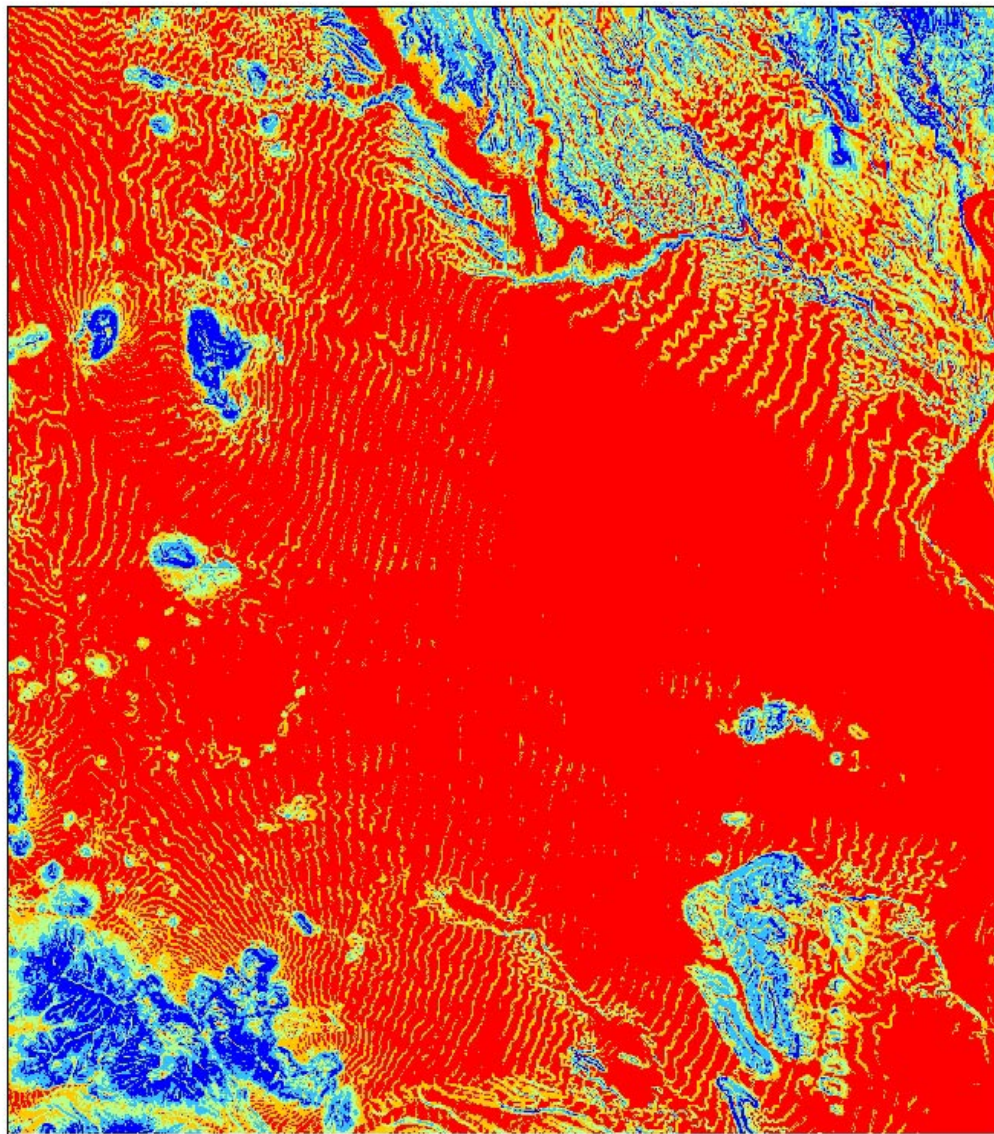




Figure 24. USGS ten meter DEMs obtained from GIS Data Depot. Four 7.5 minute USGS quadrangles were mosaicked and converted to grid files using ArcMap and ArcToolbox.



Legend

Value

	0 - 3.199601412
	3.199601413 - 8.111279488
	8.111279489 - 13.51969242
	13.51969243 - 20.55604553
	20.55604554 - 50.60664749



0 1,600 3,200 6,400 Meters

Figure 25. Slope mosaic of study area derived from USGS ten meter DEMs in ArcMap. Value is equal to slope measured in degrees.

3.4.Data Processing

Image processing was performed on Sun Blade 100 workstations and PC's using the Environment for Visualizing Images (ENVI) software by Kodak Inc., ERDAS Imagine, and Environmental Systems Research Institute (ESRI) ArcGIS software in the Image Visualization and Infrared Spectroscopy (IVIS) laboratory at the University of Pittsburgh.

The flowchart in Figure 26 illustrates the methodology used to process and extract data for submission to an expert classification system (Stefanov et al., 2001). Only level 2 ASTER data was used for this project, which is calibrated and atmospherically corrected using a look up table approach combined with atmospheric information obtained from other climatological data sets. Calibration and atmospheric correction for the Landsat TM data was performed using ENVI's calibration routine. ENVI 4.0 automatically imports georeferencing information for ASTER and Landsat scenes. All images and vector data sets were subsequently georegistered to the September 2000 ASTER VNIR image, which was defined in a UTM Zone 12 North WGS-84 coordinate system. The raster data sets were georegistered using ENVI's map registration routine that employs a rotation, translation and scaling algorithm using ground control points to warp one image to another. A minimum of 6 ground control points were selected for each scene warped, with an average RMS error of 0.7. The coordinate systems for the vector data sets were redefined using ArcToolbox. The raster data sets were then spatially resampled to 15 meters using ENVI's resize data routine, in preparation for data fusion.

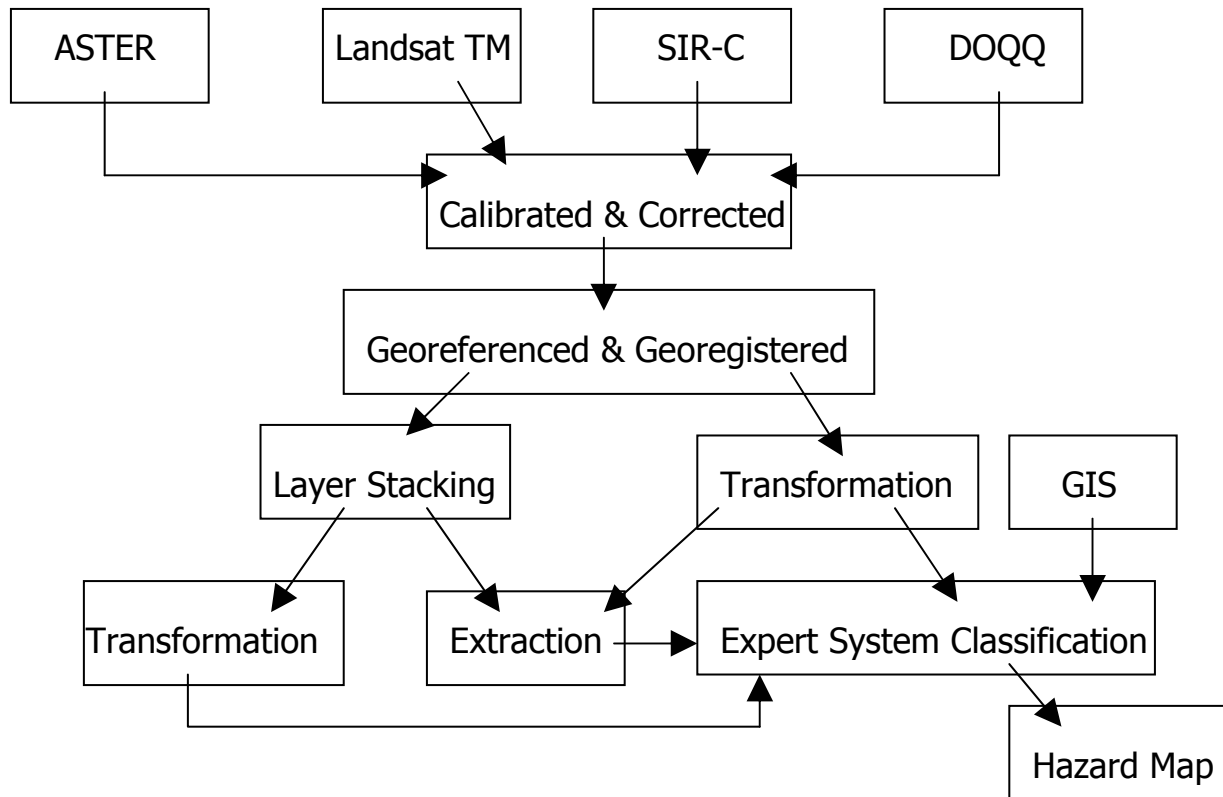


Figure 26. Flowchart describing image processing methodology employed in study.

3.5. Vegetation Indices

Vegetation reflectance is based upon cellular structure and chlorophyll content (Lillesand and Kiefer, 1994). Environmental changes such as drought or fire can result in distinctive changes in the chlorophyll content or cellular structure of vegetation (Figure 18). These changes in vegetation health can be detected through the use of band ratio techniques such as Normalized Difference Vegetation Index (NDVI) (Rouse et al., 1974) and Soil Adjusted Vegetation Index (SAVI) (Huete 1988).

NDVI is calculated by the following equation (Equation 1):

$$\frac{(\text{Near infrared} - \text{Red})}{(\text{Near infrared} + \text{Red})}$$

Near infrared is equivalent to ASTER band 3 and Red is equivalent to ASTER band 2.

NDVI equation with ASTER bands (Equation 2):

$$\frac{(\text{ASTER Band 3} - \text{ASTER Band 2})}{(\text{ASTER Band 3} + \text{ASTER Band 2})}$$

The resulting image is grayscale with values ranging from -1 to 1. Healthier plants have a higher chlorophyll content reflecting more energy in the infrared wavelength, and absorbing energy in the red wavelength (Lillesand & Kiefer 1994). Healthier vegetation is therefore brighter with the healthiest vegetation possessing values equal to 1.

SAVI is expressed as (Equation 3):

$$\text{SAVI} = \frac{(\text{Near infrared} - \text{Red})}{(\text{Near infrared} + \text{Red} + L)} \quad (L + 1)$$

where NIR and Red are near-infrared and red reflectance, and L is a dimensionless constant. L ranges from 0 – 1 depending on the amount of visible soil; L = 0 for high vegetation densities and L = 1 for low vegetation densities.

SAVI equation with ASTER bands (Equation 4):

$$\text{SAVI} = \frac{(\text{ASTER Band 3} - \text{ASTER Band 2})}{(\text{ASTER Band 3} + \text{ASTER Band 2} + 1)} \quad (1 + 1)$$

SAVI is useful in areas where plant cover is low and it is necessary to adjust for background soil brightness. Stefanov et al. (2001) determined SAVI was a better approximation of vegetation vigor in a semi-arid area with sparse vegetation cover. Therefore, this study utilized SAVI to determine vegetation vigor instead of NDVI. The band math routine in ENVI was used to extract SAVI data from the ASTER VNIR image.

Tasseled Cap is another index that is commonly used with Landsat data to evaluate vegetation vigor. This transformation technique compresses spectral data into a few bands (similar to a principle component analysis) that are useful for interpreting specific scene characteristics such as brightness, greenness, and wetness.

3.6.Data Fusion

Data fusion combines two or more different images to form one new image. Fusing data from multiple sources improves the quantity/quality of information that can be obtained from a single source. Benefits of fusion include image sharpening by combining high resolution data with low resolution data, improvement of registration accuracy, and improvement of classification accuracy by combining reflectance (ex. ASTER) data with roughness data (ex. SIR-C). In addition, change detection can be achieved by combining images from different time periods (Lei et al 2001), and information loss can locally be corrected by combining a cloud free image with a cloudy image.

Data fusion was performed using ENVI to produce two separate images for analysis. The first image was created by layer stacking the ASTER VNIR, SWIR and ASTER SAVI data sets together. The second image was produced by layer stacking the ASTER VNIR, SWIR, Landsat TM and SIR-C data sets together.

3.7.Classification

Classification is a common data extraction technique utilized to interpret remote sensing image data. Image classification is accomplished by using an algorithm to assign a pixel to a single spectral class. There are two main methods for classification: supervised and

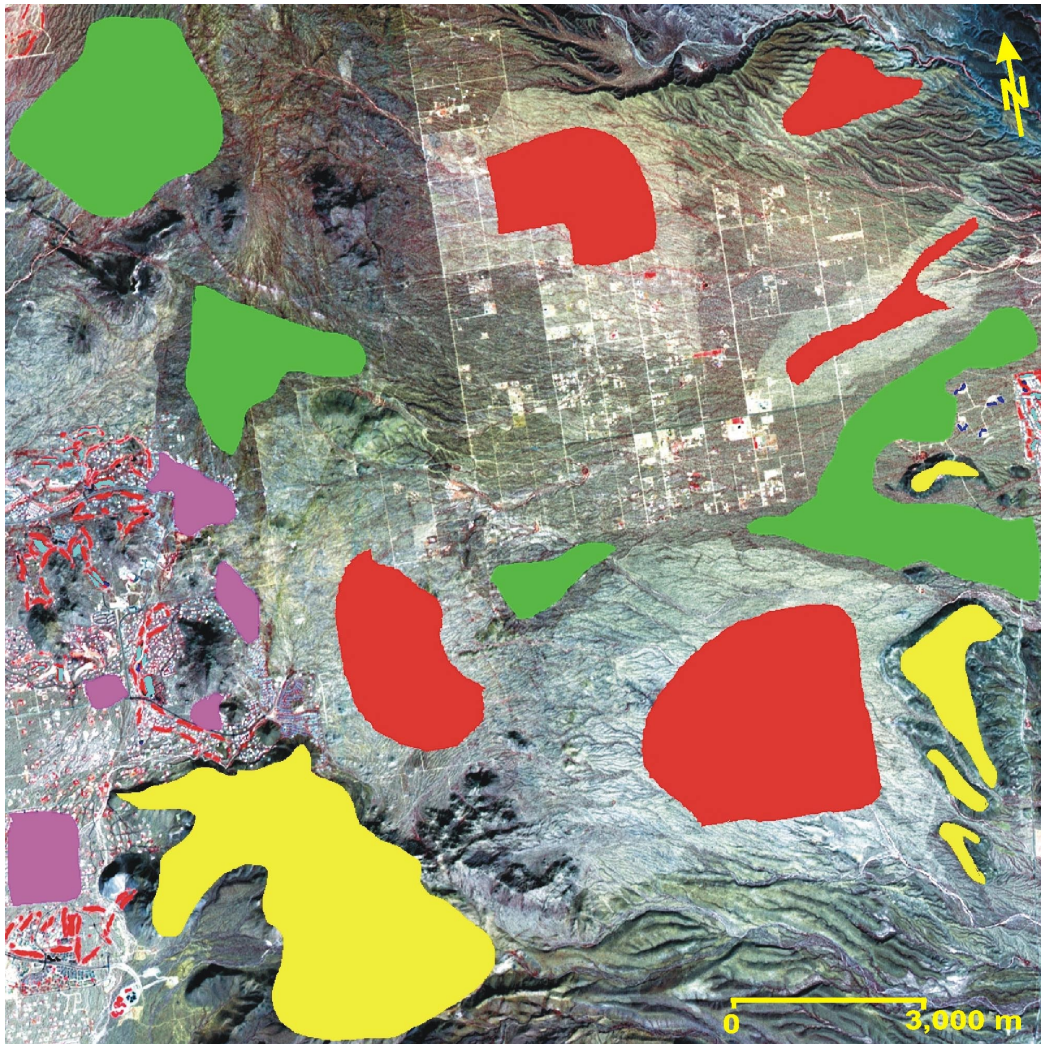
unsupervised. A supervised classification is performed using training regions selected by the user. The classification algorithm determines a spectral signature that it assigns to each target class (Vincent, 1997). Pixels will either be assigned to a target class or classed as “other”. Unsupervised classification techniques use statistical methods (such as minimum spectral distance) to form data clusters. Each pixel in the image is assigned to the cluster to which it is most spectrally similar. The user must review each computer generated class to determine which if any discrete ground class it corresponds to (Vincent, 1997).

This project uses the maximum likelihood classification technique and the decision tool classifier in ENVI. The maximum likelihood routine applies the following equation (to each pixel in the image) (Equation 5):

$$g_i(x) = -\ln \mathbf{COV}_i - (x - m_i)^T * (\text{sum over } i \text{ of all } (x - m_i))$$

The variables are defined as: i is the class, x is the pixel, \mathbf{COV}_i is the covariance matrix of class i , and m_i is the mean spectrum for class i . The pixel is assigned to a class based on the highest probability that it belongs to that class. This probability is calculated based on the following equation: $\text{probability} = g_i(x) / (\text{sum over } i \text{ of all } g_i(x))$. A pixel remains unclassified if its highest probability is less than a threshold value entered by the user.

Training regions were chosen based on field and land use data (Figure 27). A maximum likelihood classification routine was run with the Landsat, ASTER VNIR, ASTER SWIR, and fused datasets.









Color	Class	Definition
	Burned	Mixed dead and healthy desert vegetation
	Unburned Desert Vegetation	Healthy desert vegetation
	Water	Standing or flowing water
	Bedrock	Bare/exposed rock
	Vegetation	Actively photosynthesizing vegetation (golfcourses)
	Urban	Disturbed residential, commercial or industrial areas

Figure 27. ASTER VNIR image overlay with training regions that were chosen based on field investigations.

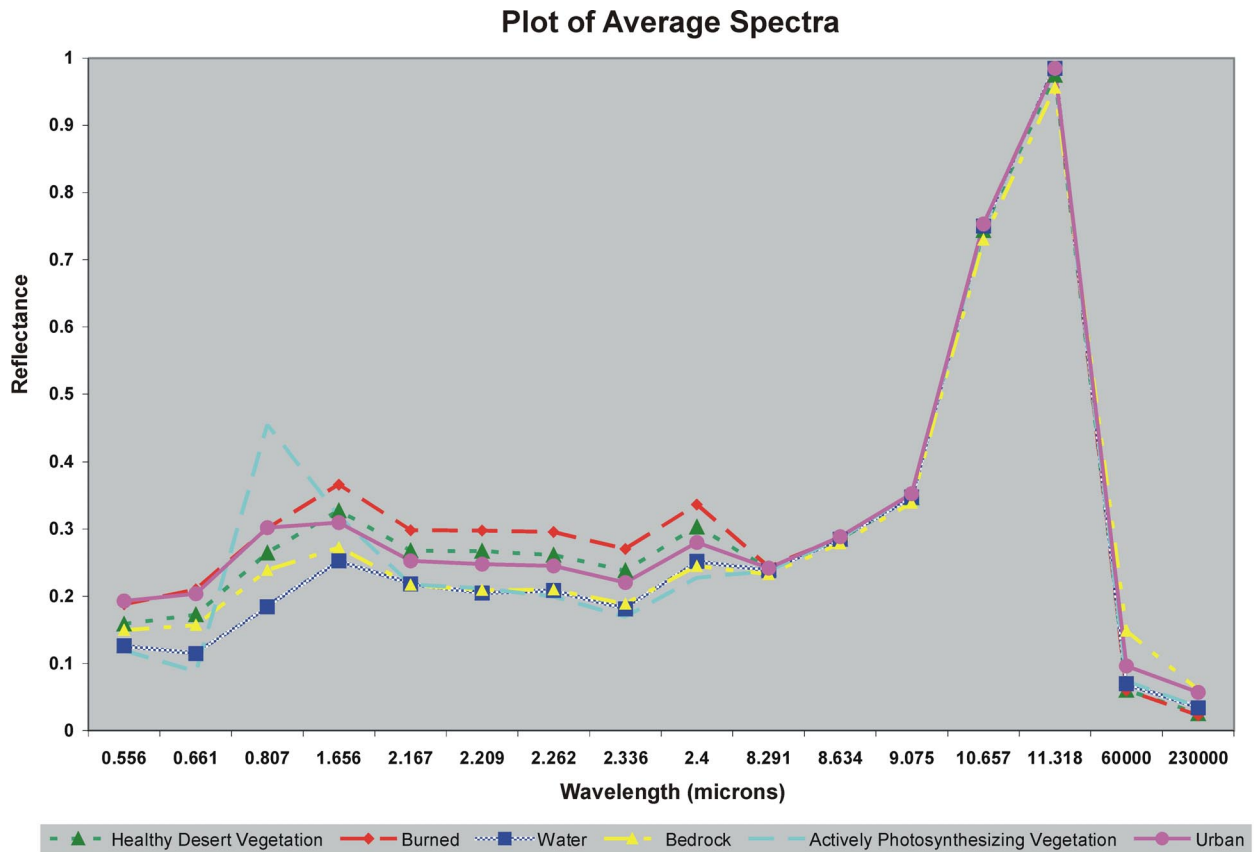


Figure 28. Average spectra for training regions over ASTER VNIR and SWIR, TIR, and SIR-C wavelengths.

A decision tree classifier is a non-parametric, multistage, hierarchical decision based classifier. The tool is implemented with an initial expression that results in two subclasses or another expression node (Figure 29). The classification progresses by moving down the tree until a class is reached. Multiple images from various sources can be submitted to this tool at different spatial resolutions and projections. The user specifies a base image, projection, spatial resolution, and ENVI does the resampling and reprojection of input data during the execution of the classifier.

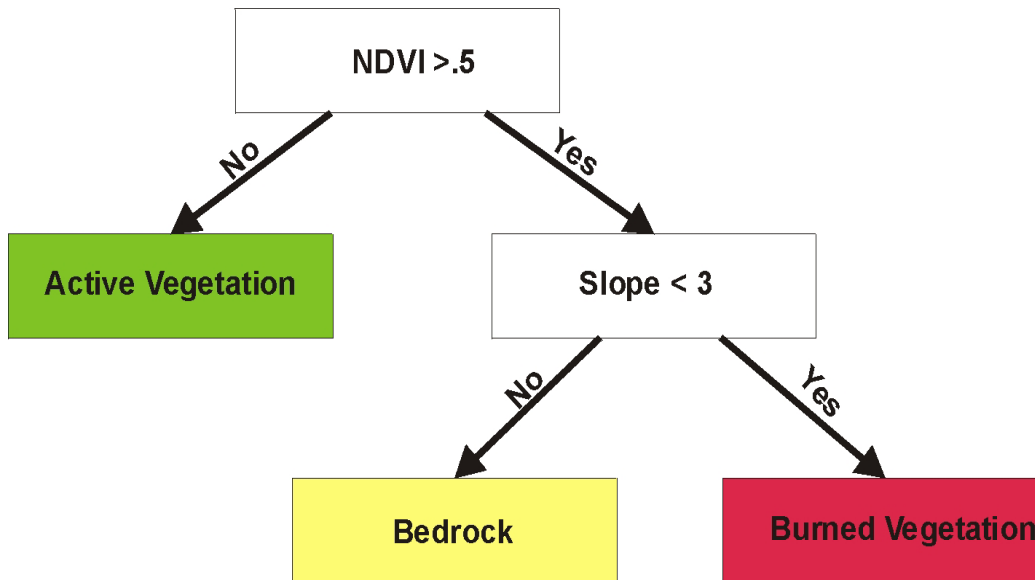


Figure 29. Decision Tree Tool example. White boxes represent expression or decision nodes, and colored boxes represent leaves or daughter classes.

3.8. Classification Accuracy Assessment

Error matrices are an effective method for assessing classification accuracy (Story and Congalton, 1986). Accuracy assessment for this project was accomplished through the use of error matrices generated in ENVI. Target classes produced from supervised classification routines were compared with land cover types obtained from field data. Overall accuracy, errors of omission/commission, user's accuracy and producer's accuracy are reported. Overall accuracy is the sum of all pixels classified correctly divided by the total number of samples. How well a certain area is classified is measured by the producer's accuracy, which also measures errors of omission. This measurement is determined by the number of correctly classified pixels of a reference class divided by the total number of pixels in the reference class. The user's accuracy measures the probability that a classified pixel actually represents the same class on the ground. This is also known as commission error, and is determined by dividing the

number of pixels correctly classified by the number of pixels in that class (Story and Congalton, 1986).

3.9. Image Segmentation

A discontinuity adaptive Markov Random Field (DA-MRF) routine is utilized as an automated method for fire scar recognition in ASTER NIR, SAVI and SWIR data sets. This algorithm works by employing a low pass (smoothing) filter over the image, and preserving edge information. Remote sensing image analysis (RESIMA) application software is used to employ this algorithm. This software was developed to complement material provided during the 1999 and 2000 International Geoscience and Remote Sensing Symposiums (IGARSS), and is provided free of charge for student use.

3.10. Change Detection

Classification images from two different time periods were analyzed for differences or change. Change is evaluated based on the class of a pixel in the initial image being classified as its equivalent class in the final image. This change is calculated using ENVI, which produces a class mask that is color coded the same as the final state classification image. However, pixels that changed classes are assigned the class values into which they have changed.

3.11 Hazard Map

GIS has been used successfully in previous work to combine various vector data sets such as slope, aspect and elevation with Airborne Visible/Infra-red Image Spectrometer (AVIRIS), AVHRR and Landsat data to produce fire hazard maps (Yool et al., 1985; Chuvieco and

Congalton, 1989; Chuvieco and Salas, 1996). Most fire hazard maps are developed for temperate and alpine ecosystems, and contain one or more of the following criteria: fuel load, slope, aspect, and vegetation moisture. This project utilizes ESRI's ArcGIS software package to combine vector data with the remote sensing data to produce a hazard map for the study area. Each data set is represented in the map as an individual layer. These data were made available to the public by publishing it to the World Wide Web through the use of ESRI's ArcIMS software. The map can be accessed through this URL, <http://aster.eps.pitt.edu/fires> which is hosted by the IVIS laboratory.

ANALYSIS & RESULTS

4.1 Geomorphology Results

Two main goals were addressed with the geomorphology study: (1) to investigate the rate and development of channelization and (2) to investigate the relationship between fires and sediment flux. A detailed topographic survey using an electronic total station combined with a GPS was completed in order to address the first goal. Initial survey results from this mapping project indicate an increased channelization in burned areas (Figure 30).

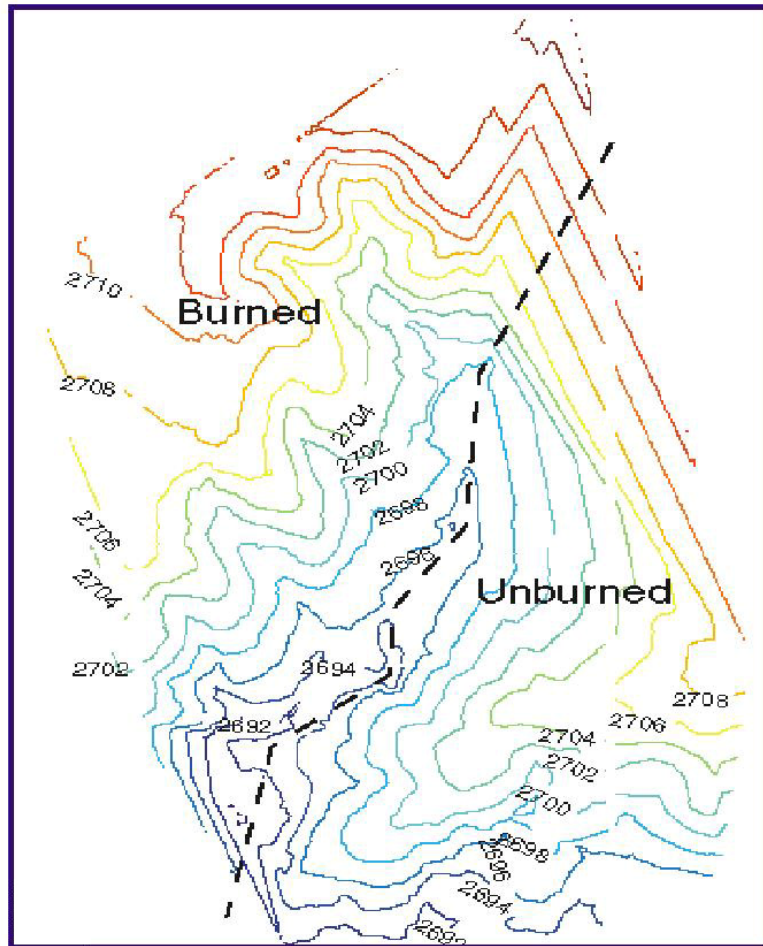


Figure 30. Contour map produced from the detailed field survey using GPS and an electronic total station illustrates the increased drainage density that is apparent in the burned area versus the unburned area.

Investigation of the relationship of fires and sediment flux was addressed through the installation and monitoring of sediment traps, and a soil erosion study in McDowell Mountain Park (Figure 14). During the study period there was one major rain event that occurred in February 2003 (Figure 31). During this event the traps were monitored and sampled (Figure 32). Trap samples were analyzed for grain size and carbon content. Grain size analysis for burned catchments resulted in plots that were very similar (Figure 33). The mean for the burned catchment was within the silt size class (Table 4). Grain size analysis for the unburned catchment also resulted in plots that were similar for all of the traps but one (Figure 34). MMPU4 is a large trap located in a channel with the largest catchment area for all of the traps in the study (Tables 5 & 6). This resulted in coarser size fractions captured in this trap, most likely due to higher velocity flows that carried fines through the trap leaving only coarse fractions behind. The mean size class for the unburned catchment was also in the silt class size (Table 7). A plot comparing average grain size for each size class in burned versus unburned areas did not reveal any distinct differences between the two areas (Figure 35).

Total carbon for each area is reported as percent Loss on Ignition (LOI, Table 8). The mean carbon content for the burned area was 6.32% as compared to 11.04% for the unburned area. This demonstrates that there is more organic matter in the unburned catchments compared to the burned catchments.

The soil erosion study conducted in McDowell Mountain Park (Figure 36) revealed a mean regolith depth of 13.3 cm in the burned transect compared to 11.9 cm in the unburned transect. The mean curvature was 0.023 for the burned area compared to 0.019 in the unburned area. Curvature comparisons for the burnt and unburned transects are plotted in Figure 37.

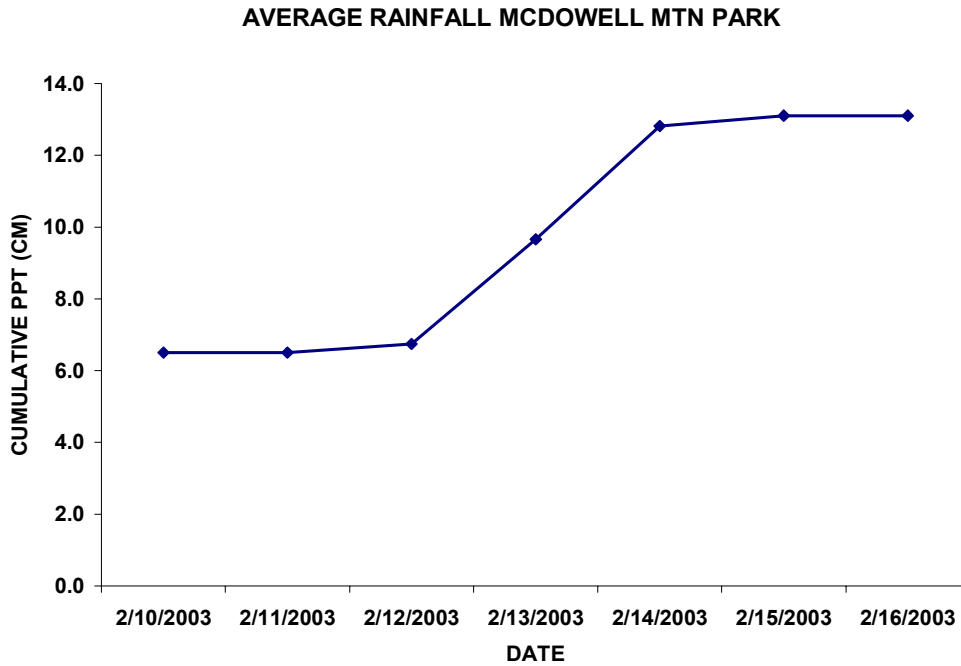


Figure 31. Average rainfall during sediment trap sampling event (data from McDowell Mtn. Park rain gauge).

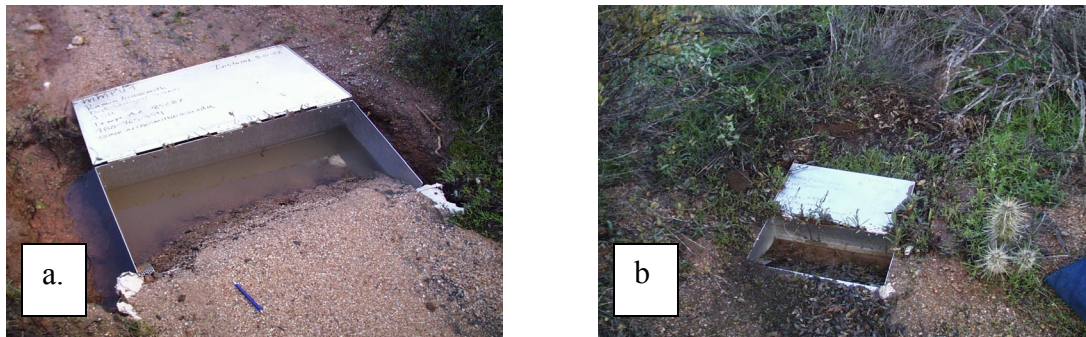


Figure 32. a) Sampling of large sediment trap, MMPU4, in unburned catchment. b) Sampling of small sediment trap, MMPU5, in unburned catchment.

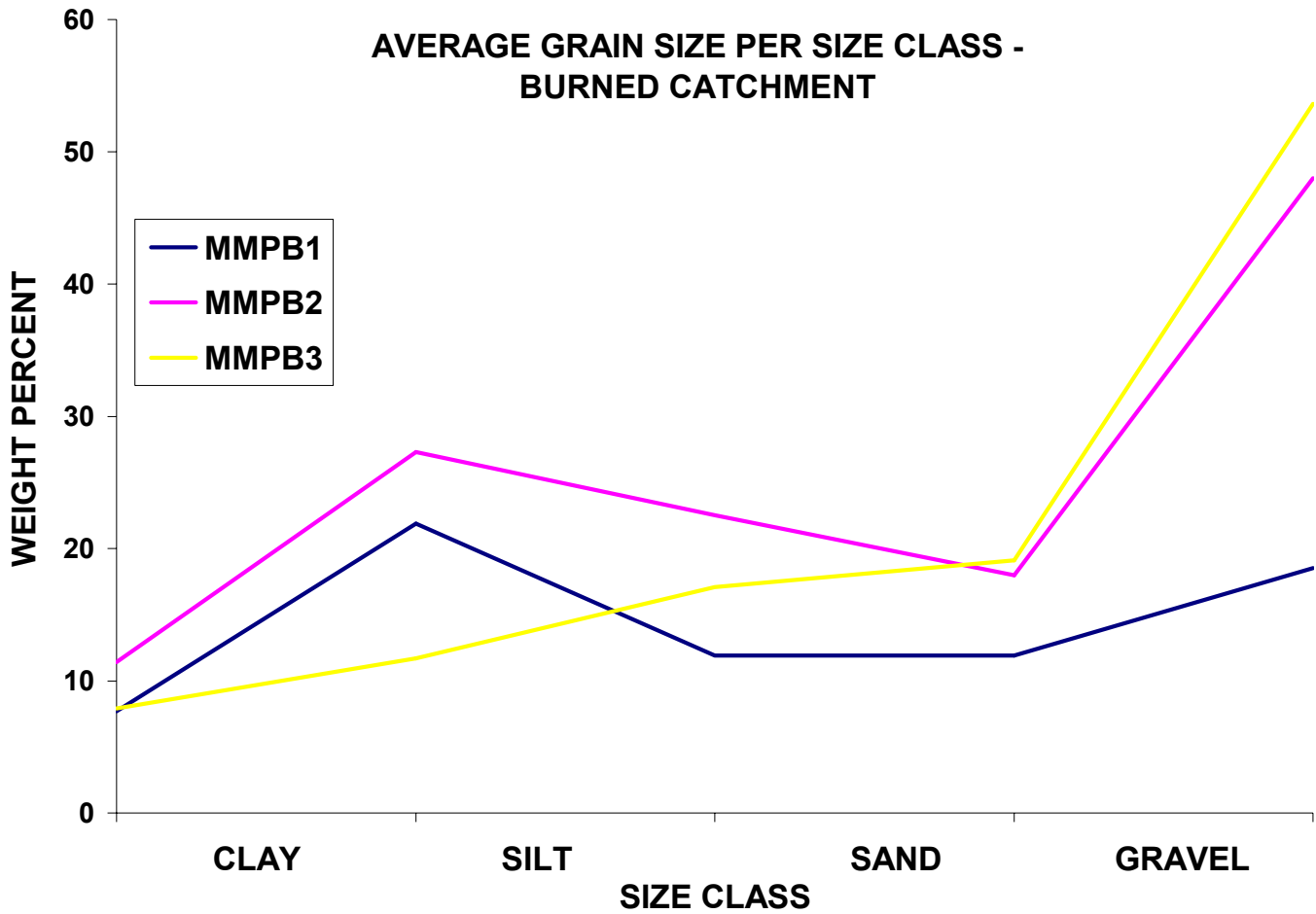


Figure 33. Grain size plot of burned catchment.

Table 4. Grain size analysis statistics for burned catchment.

BURNED CATCHMENT		
sample #	MEAN	STD DEV
MMPB1	14.4	5.7
MMPB2	25.4	13.9
MMPB3	21.9	18.3

Table 5. Contributing area to each trap in burned catchment.

BURNED CATCHMENT	
TRAP #	AREA (M ²)
MMPB1	616
MMPB2	4091
MMPB3	4643

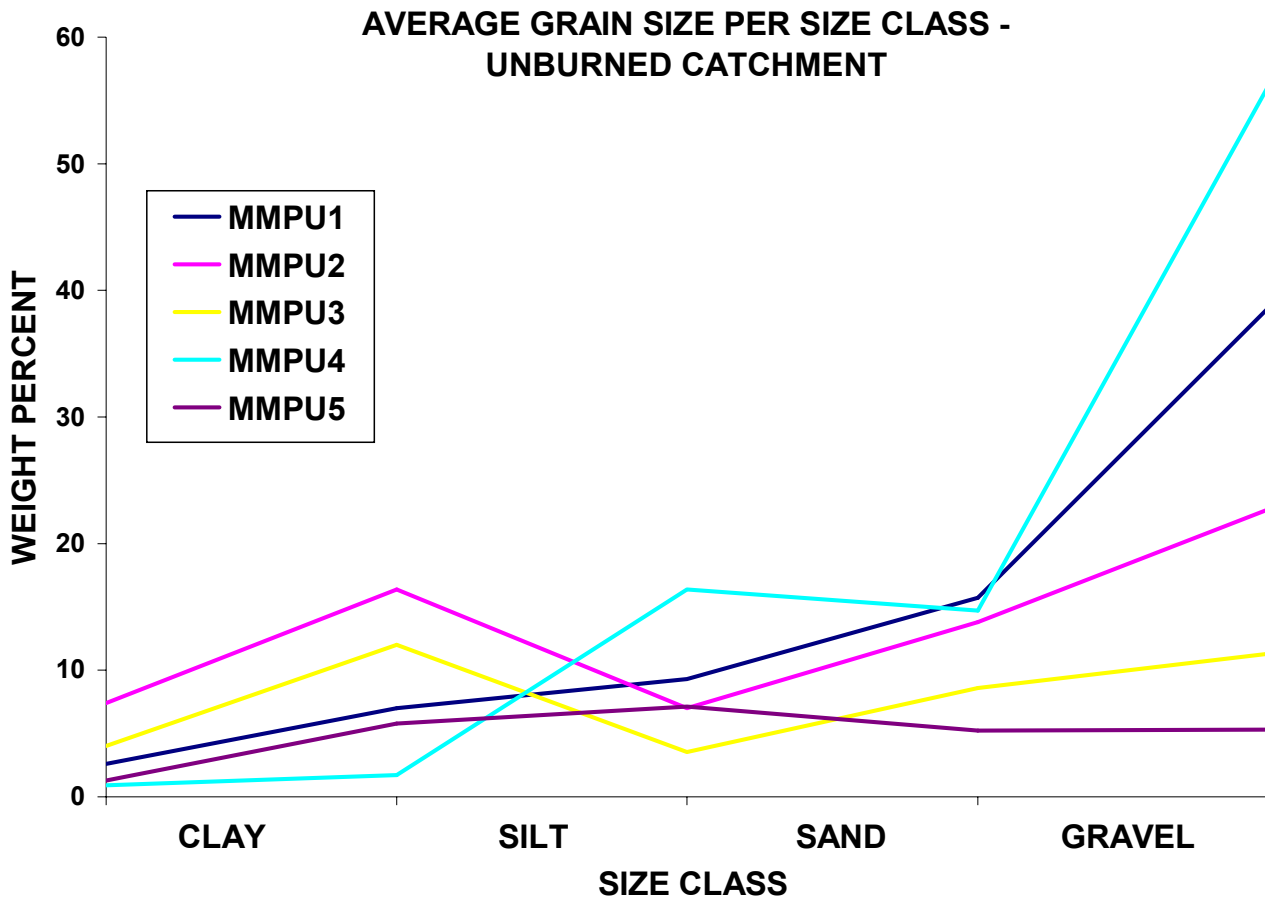


Figure 34. Grain size plot for unburned catchment.

Table 6. Contributing area to each trap in unburned catchment.

UNBURNED CATCHMENT	
TRAP#	AREA (M ²)
MMPU2	415
MMPU1	1555
MMPU5	1669
MMPU3	2256
MMPU4	8833

Table 7. Grain size analysis statistics for unburned catchment.

UNBURNED CATCHMENT		
sample #	MEAN	STD DEV
MMPU1	14.6	14.2
MMPU2	13.5	6.7
MMPU3	7.9	4.0
MMPU4	18.0	22.5
MMPU5	5.0	2.2

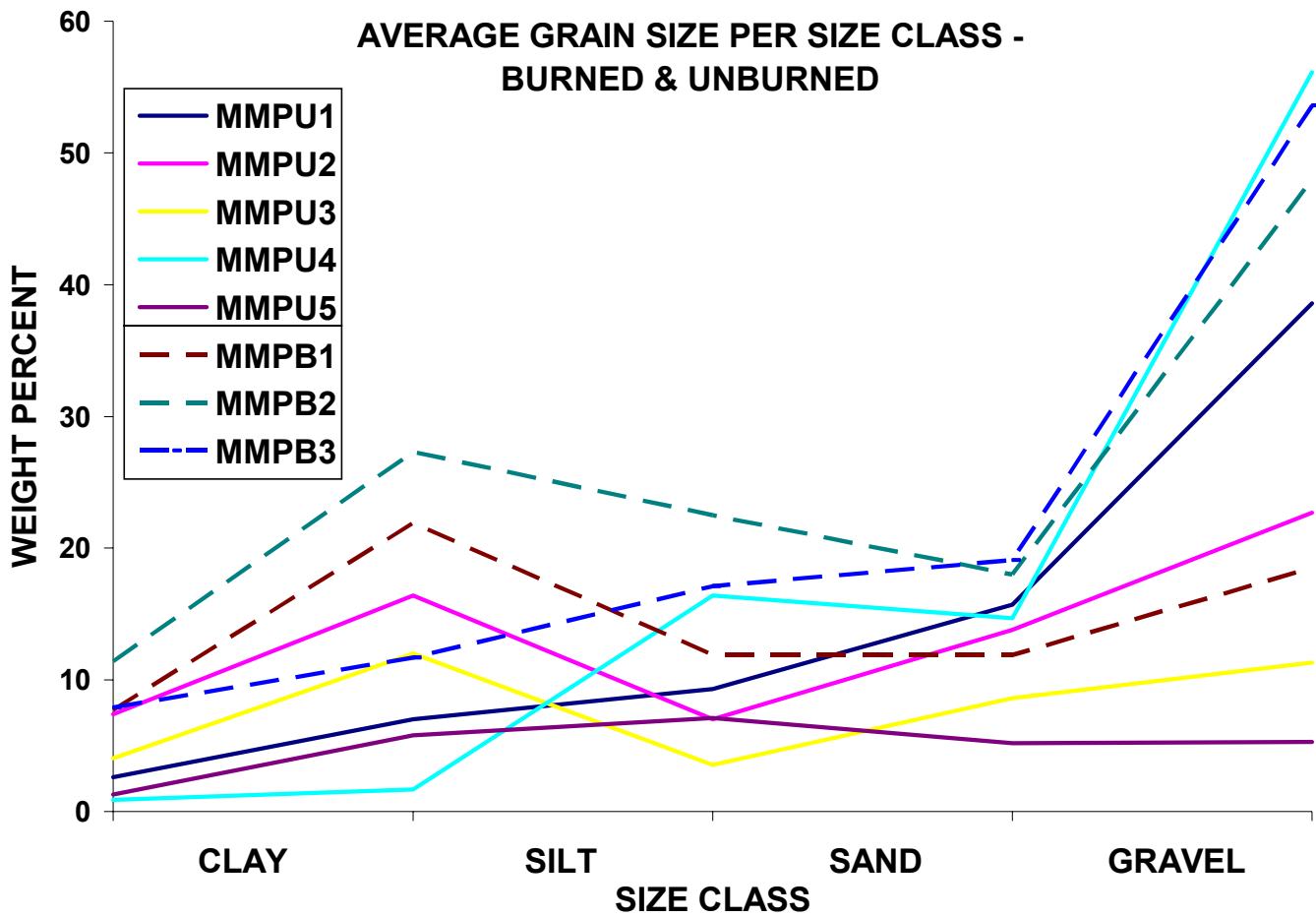


Figure 35. Plot of average grain size in burned versus unburned catchments.

Table 8. Percent LOI for burned and unburned areas.

Burned Areas		
Sample #	LOI %	
MMPB1	10.6219	
MMPB2	5.4415	Burned Mean = 6.32
MMPB3	2.8987	Burned Std dev = 3.94
Unburned Areas		
Sample #	LOI %	
MMPU1	5.4465	
MMPU2	7.8406	
MMPU3	16.2235	
MMPU4	1.5161	Unburned Mean = 11.04
MMPU5	24.1620	Unburned Std dev = 9.1

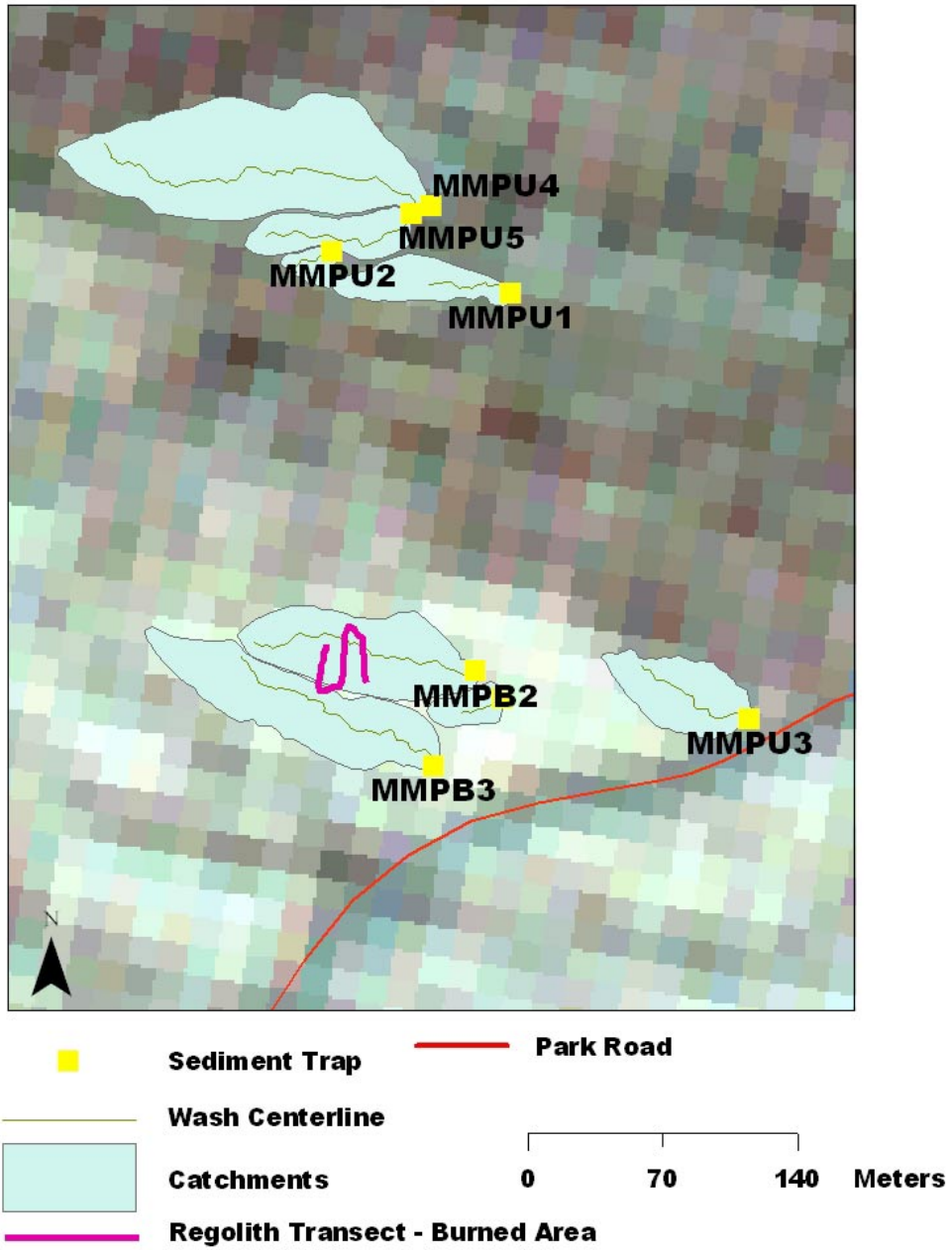


Figure 36. Map showing the location of the regolith study transect in the burned area.

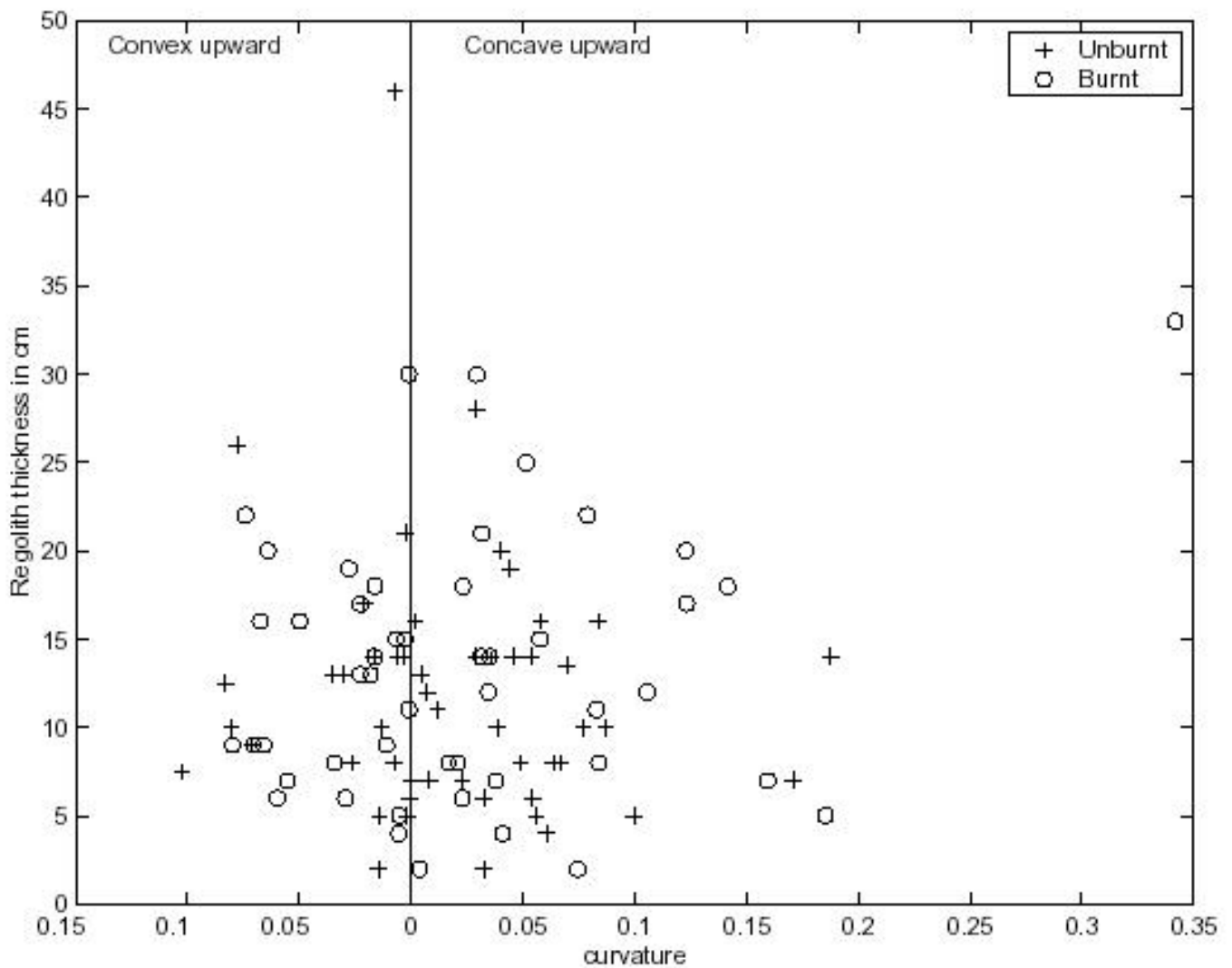


Figure 37. Regolith curvature comparison for burned and unburned transects (from Arrowsmith, 2002).

4.2 Remote Sensing

In order to determine if the increased spatial resolution of ASTER improves the classification accuracy of burned areas, maximum likelihood classifications were performed on ASTER VNIR (bands 1 – 3, 15 m resolution), ASTER SWIR (bands 4 – 9, 30 meter resolution) and Landsat TM (bands 1 – 5 and 7, 30 meter resolution). These data sets were chosen in order

to compare classification results between ASTER and Landsat data sets, and also to determine if spatial resolution has an effect on classification accuracy. Results for initial maximum likelihood classification of ASTER VNIR, ASTER SWIR and Landsat TM data sets are shown in Figures 38, 39 and 40. The overall accuracy for each classification image is listed in Table 9. The κ coefficient is also reported for each image. Kappa is another commonly used measure for classification accuracy, which includes errors of omission and commission. It can be used to determine whether results are significantly better than random, or to determine if two similar matrices are significantly different. Kappa values greater than 80% are significantly better than random, and values less than 40% are poor (Congalton and Story, 1998).

Table 9. Maximum likelihood classification accuracy results.

Image Data	Overall accuracy (%)	Overall κ (%)
ASTER VNIR	73.71	60
ASTER SWIR	71.50	57
Landsat TM	71.18	57

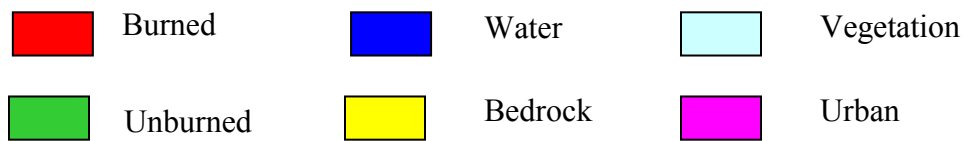
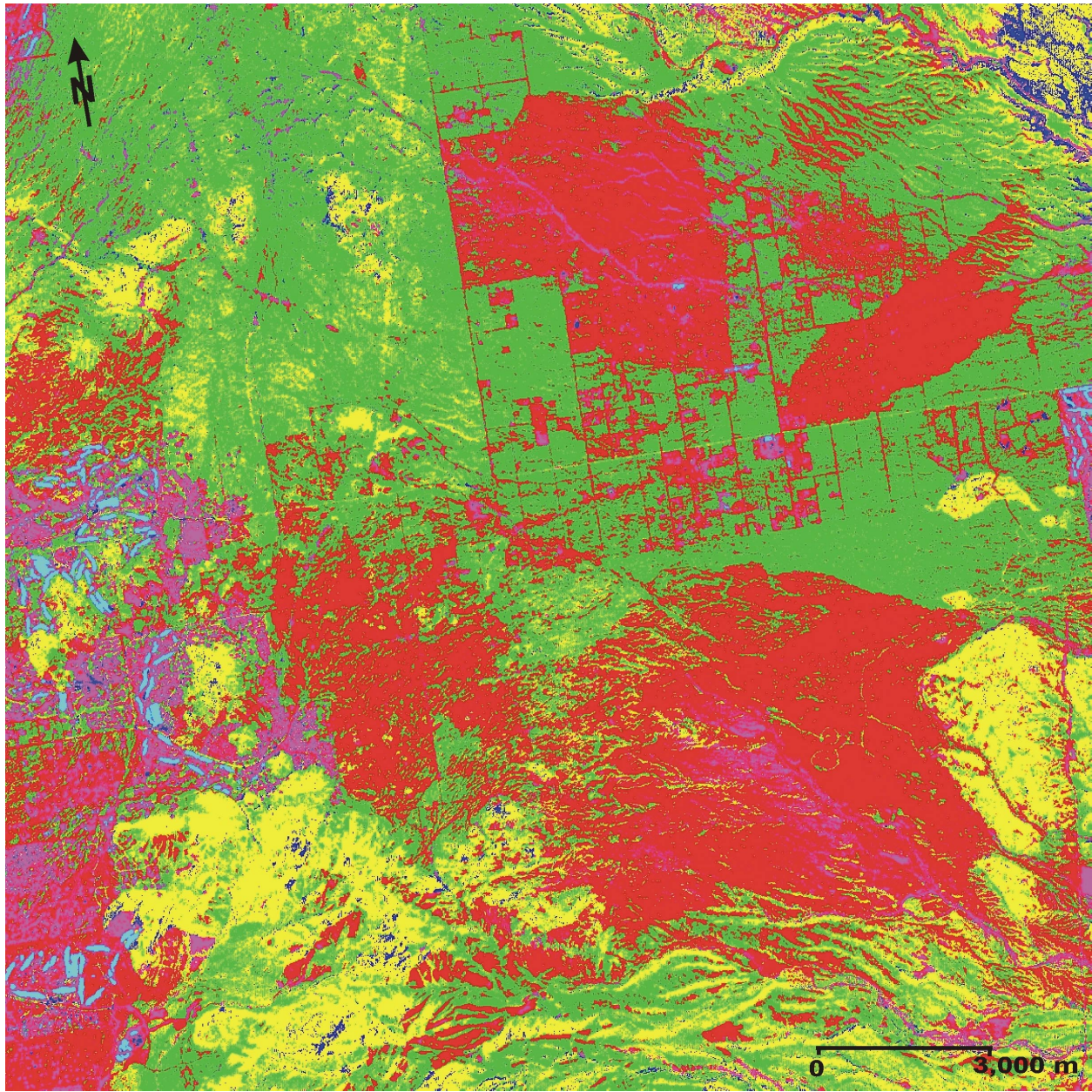


Figure 38. Maximum likelihood classification September 19, 2000, ASTER VNIR (bands 1-3).

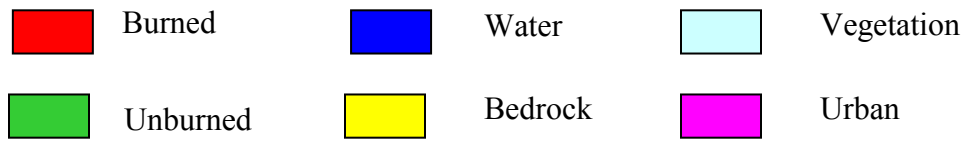
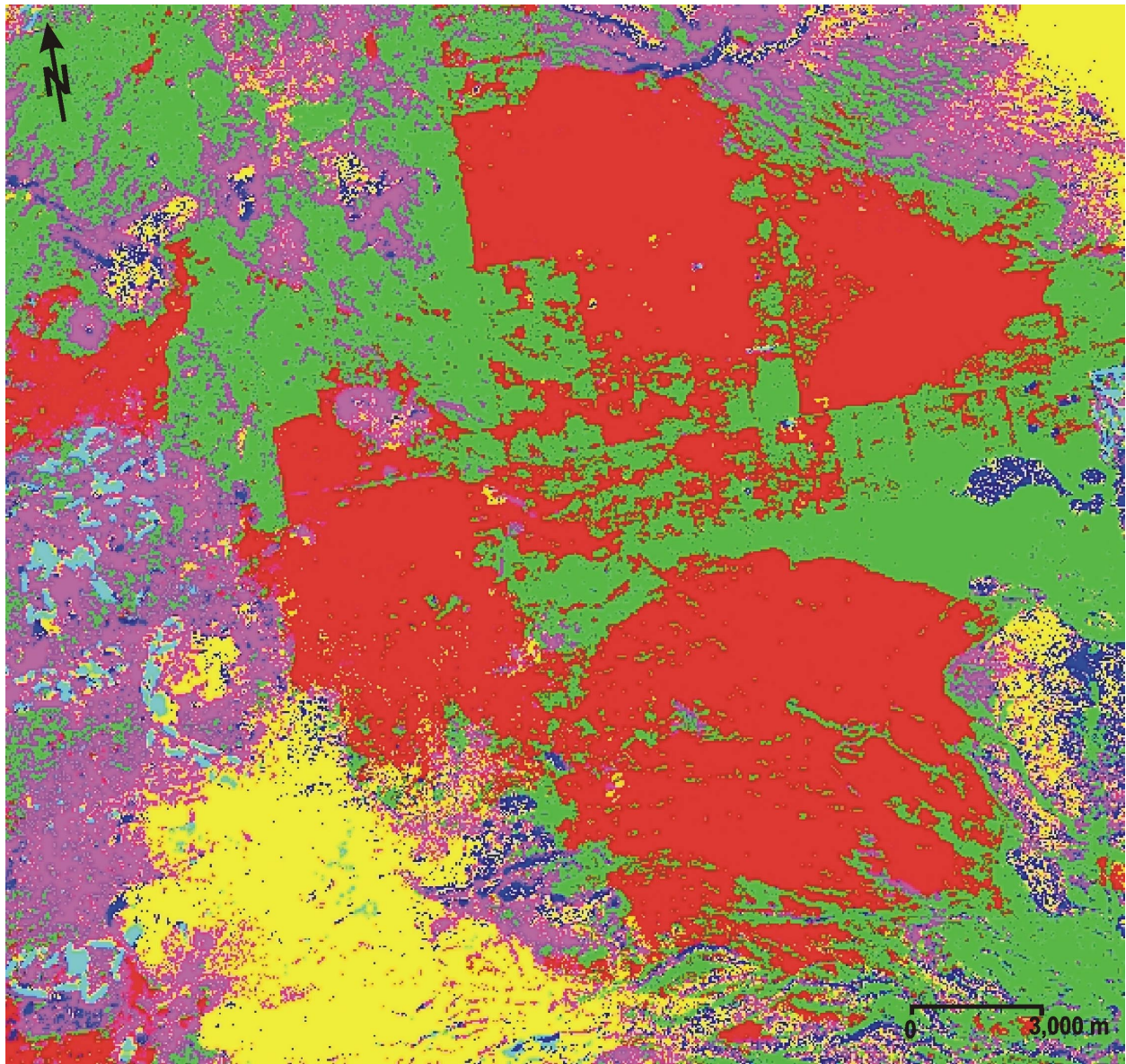


Figure 39. Maximum likelihood classification image of September 19, 2000 ASTER SWIR (bands 4-9).

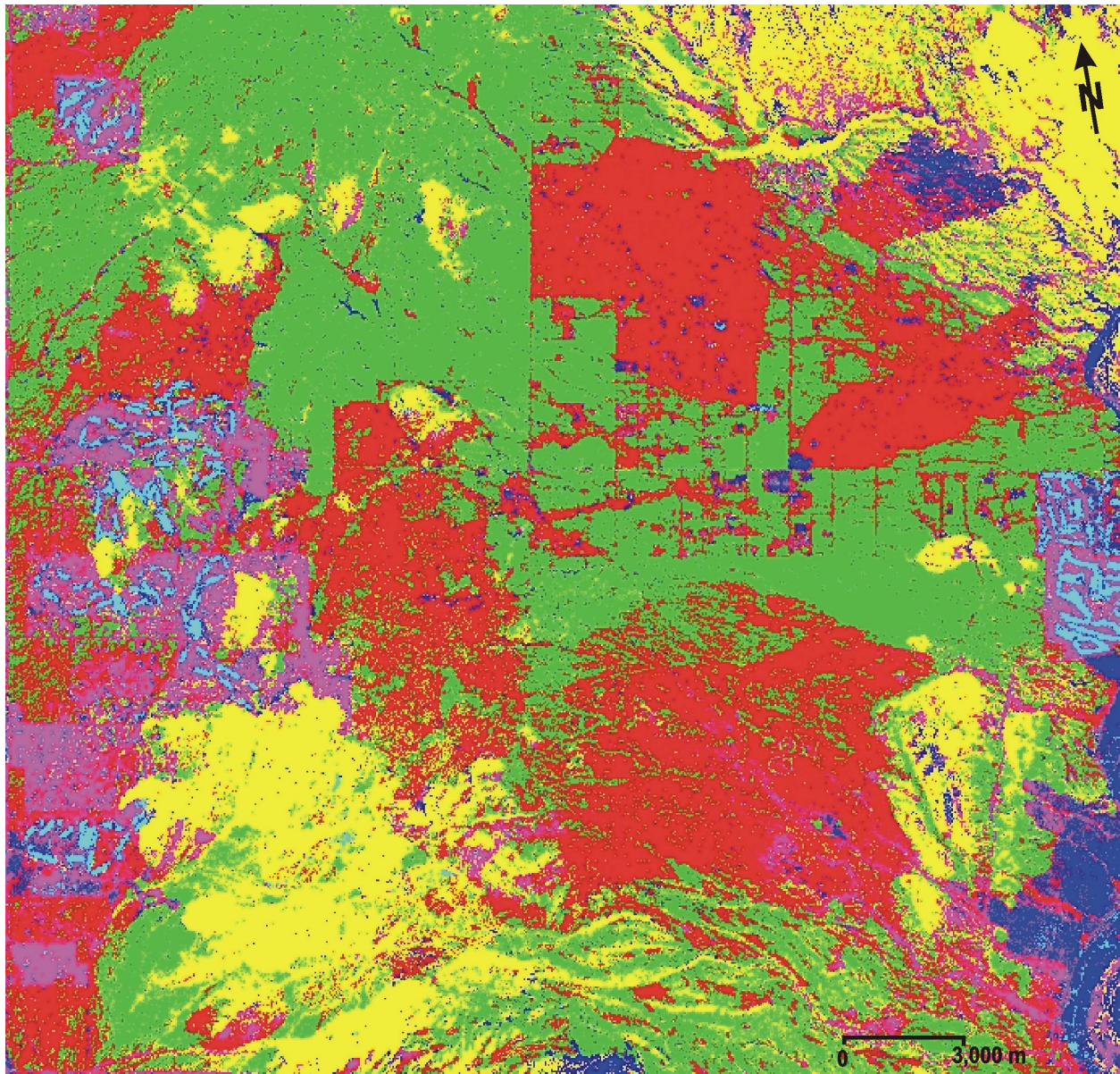


Figure 40. Maximum likelihood classification image Landsat TM (bands 1-5 & 7) September 8, 1999.

A primary goal of this project was to use only ASTER data for burned area characterization, therefore the first three data sets chosen for fusion were ASTER image data

only. The data fusion technique is used here to help improve classification accuracy. Classification accuracy was established using only ASTER data, other data sets were added to enrich the spectral information available for classification. For example, adding the tasseled cap data set added brightness (albedo) and greenness information, and including the SIR-C data added surface texture information. Data fusion resulted in four combined data sets (Table 10). A number of maximum likelihood classification routines were conducted with these data sets. The overall accuracy of each classification image is reported in Table 10. The combined ASTER VNIR/SWIR, ASTER SAVI, Landsat TM tasseled cap, and SIR-C data set resulted in the highest overall classification accuracy (Figure 41). A majority filter was applied to this data, increasing the overall accuracy to 88.99%.

Table 10. Fused data set description, and classification accuracy.

Data Set	Bands	Overall accuracy (%)	Overall κ (%)
Fused Data Set 1	ASTER VNIR and SWIR	77.68	66
Fused Data Set 2	ASTER VNIR, SWIR, and TIR	67.77	52
Fused Data Set 3	ASTER VNIR, SWIR, and SAVI	78.66	67
Fused Data Set 4	ASTER VNIR, SWIR, SAVI, Landsat TM Tasseled Cap, Sir-C	81.75	71

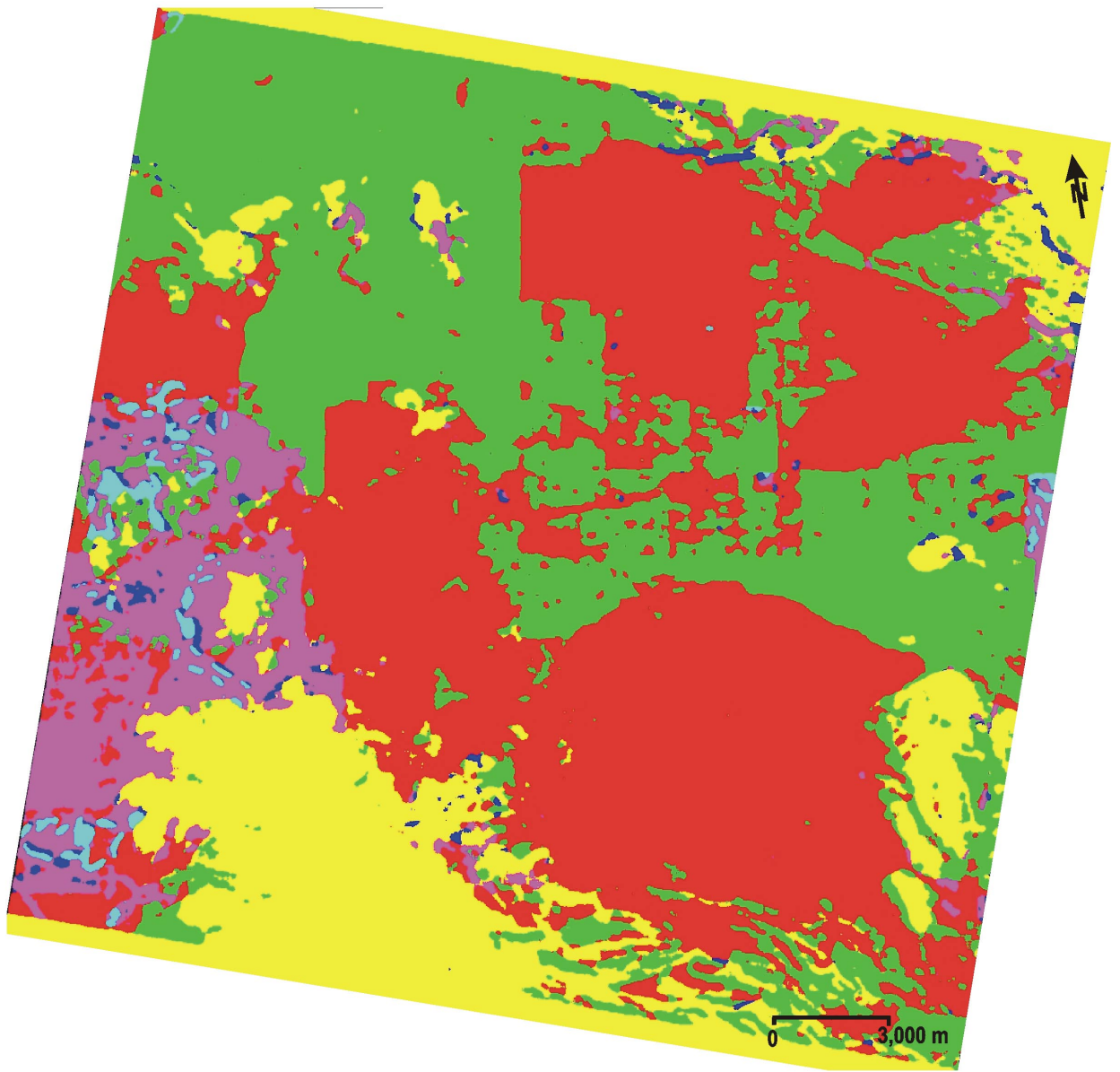


Figure 41. Resulting maximum likelihood classification image of Fused data set 4 with a 9 X 9 window majority filter. Yellow band across the top and bottom of the image are a result of the data fusion technique.

The decision tree classifier resulted in classes based on a hierarchical set of conditional arguments. Results of the decision tree classifier are presented in Figure 42. To improve the results, a majority filter with a 9 X 9 moving window was applied to the classification image. The overall accuracy for this method was 90.24% with overall κ statistics of 84%. The producer's and user's accuracy are reported in Table 11.

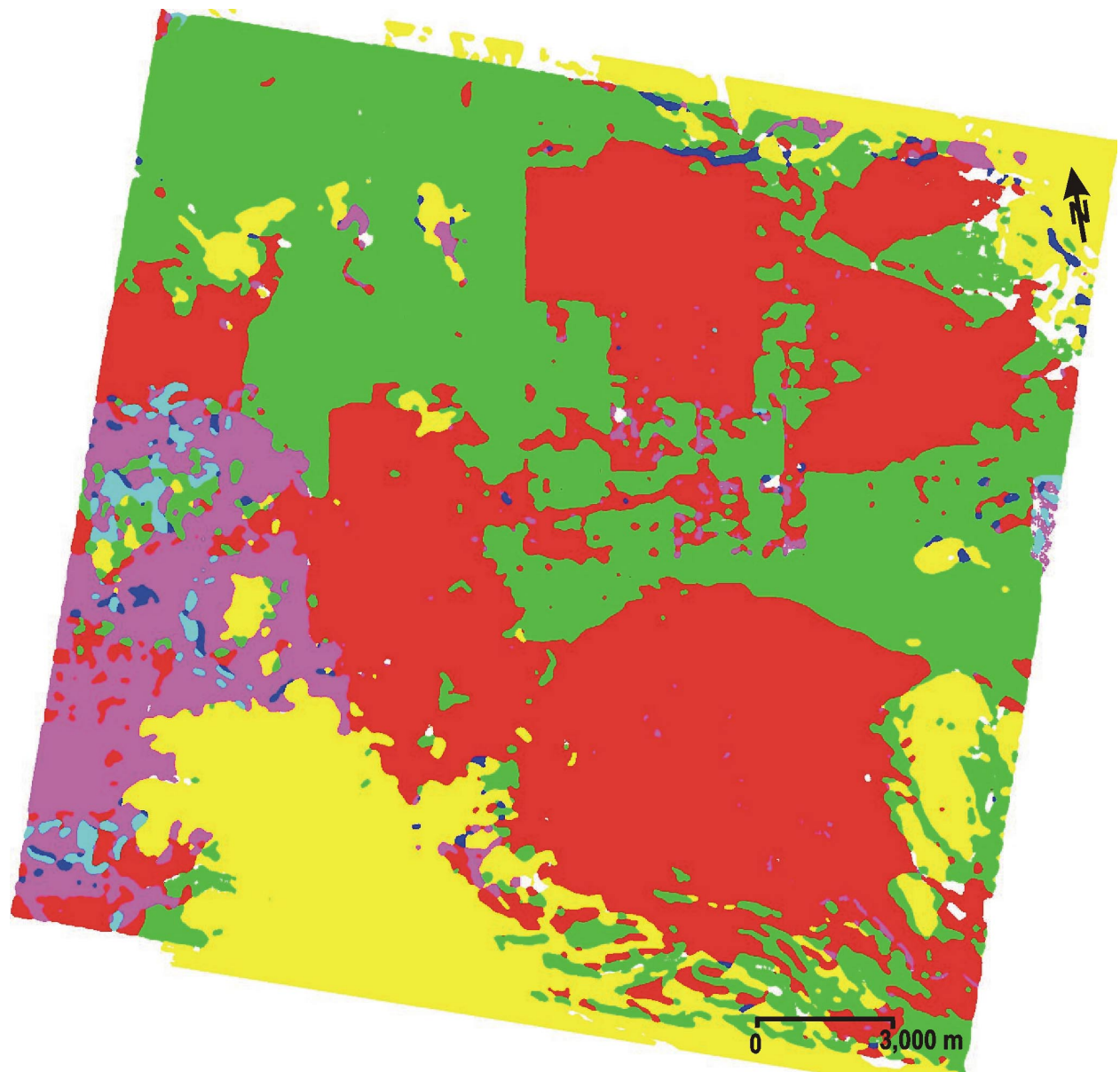


Figure 42. Decision tree classification results. Yellow band across the top and bottom of the image are a result of the data fusion technique.

Table 11. Accuracy results for decision tree classifier.

Class	Producer's accuracy (%)	User's accuracy (%)
Burned	95.85	95.07
Unburned Desert Vegetation	96.75	76.94
Water	74.02	5.02
Bedrock	81.63	95.87
Actively Photosynthesizing Vegetation	96.59	93.4
Urban	46.93	75.2

SAVI images were created using September ASTER data sets from three different years (Figures 43, 44, & 45). SAVI values of burned versus unburned areas were compared to analyze differences in vegetation health from year to year. Mean SAVI values for unburned and burned areas are listed in Table 12. These values were derived from three September, two April, and January ASTER scenes. There is no apparent trend in SAVI values over time, however the older 1988 scars have consistently higher SAVI values compared to the more recent 1995 scars.

Table 12. Mean SAVI values for burned areas listed with unburned means for comparison.

Image Date	Pinnacle/Buckhorn Fires, 1988	Camp Fire 1994	Dynamite Fire 1995	Rio Fire 1995	Unburned
4/12/00	0.476	0.487	0.449	0.451	0.492
4/02/02	0.323	0.305	0.298	0.296	0.347
1/12/02	0.368	0.329	0.324	0.338	0.390
9/19/00	0.401	0.386	0.361	0.352	0.450
9/22/01	0.351	0.335	0.318	0.327	0.382
9/16/02	0.341	0.295	0.292	0.309	0.390

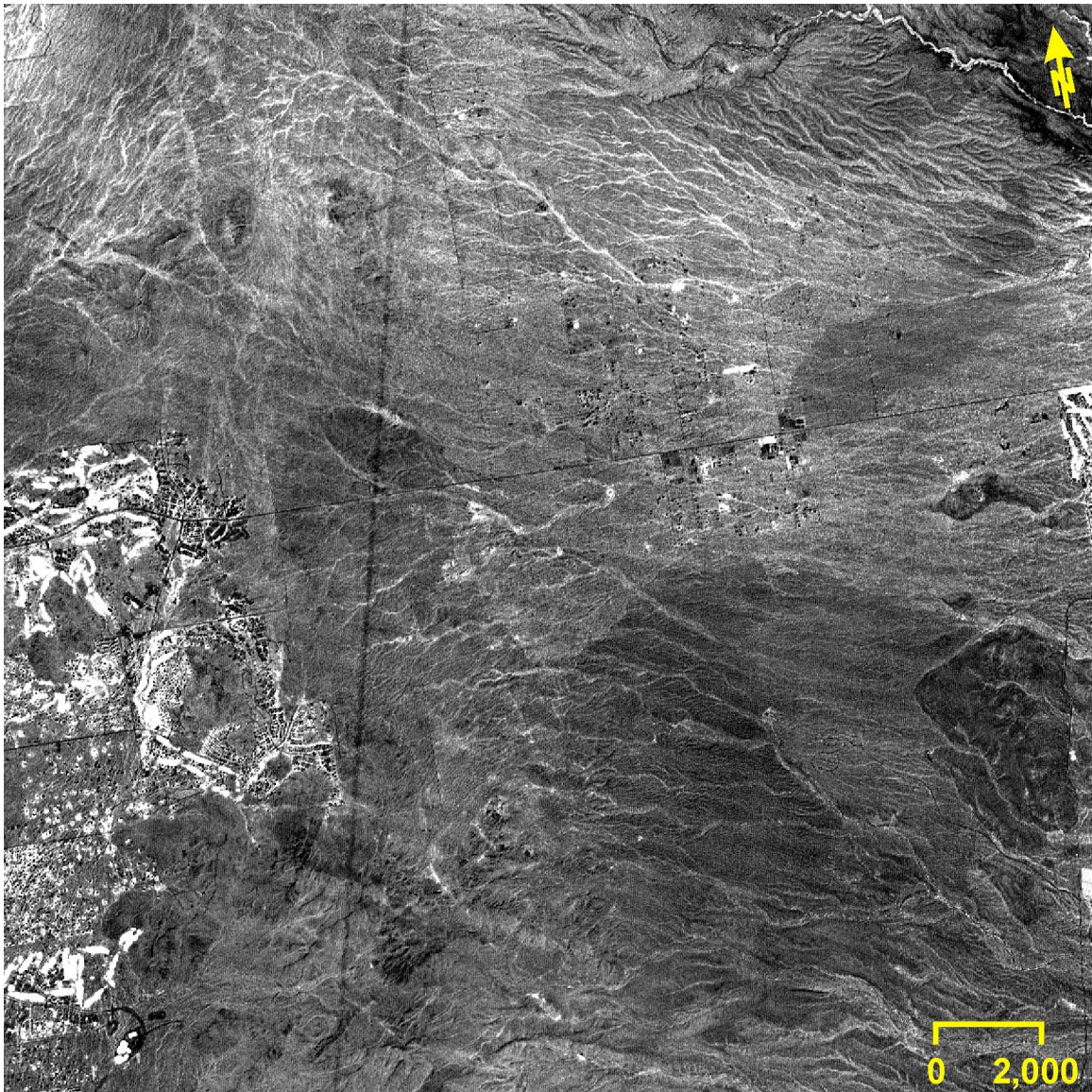


Figure 43. SAVI image data September 2000.

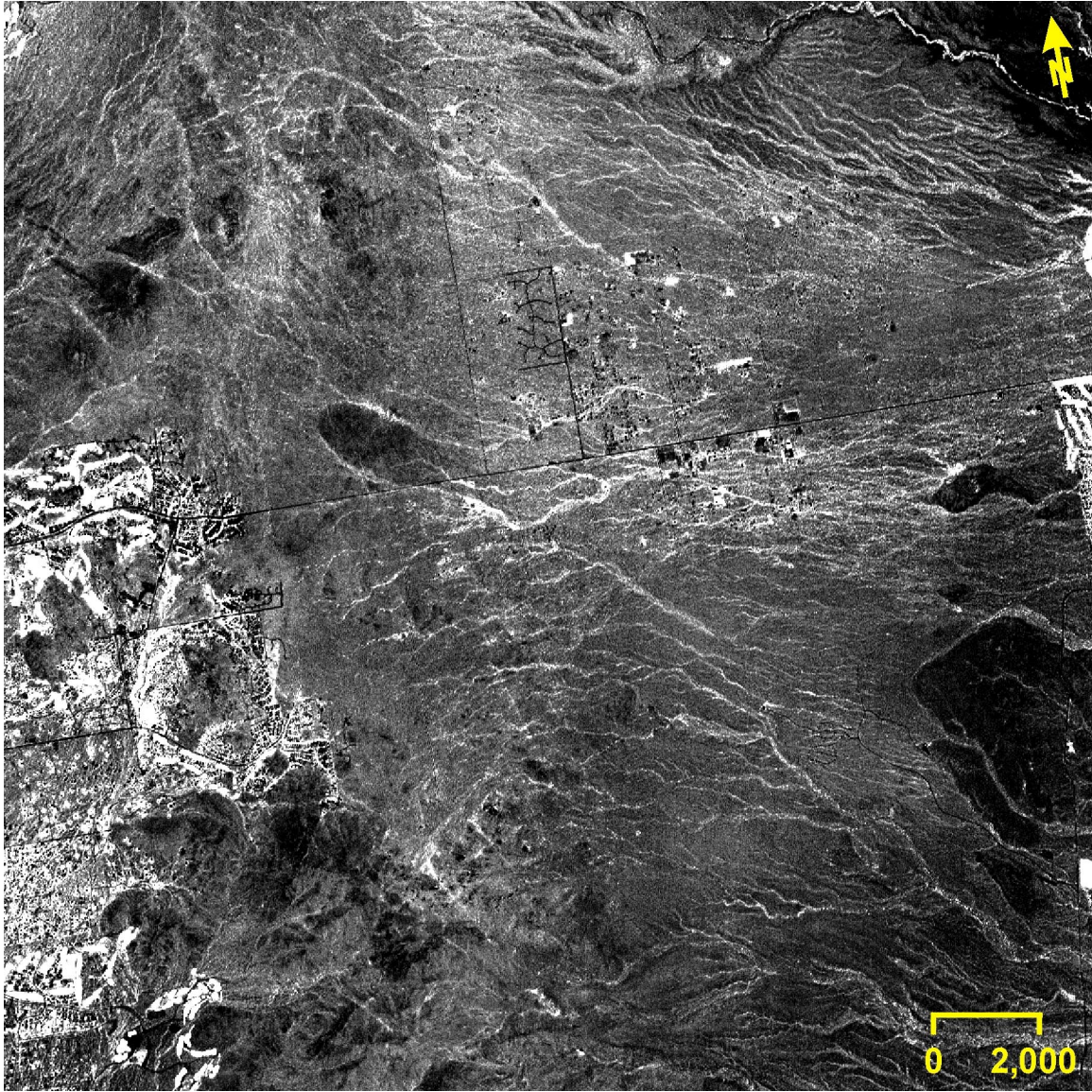


Figure 44. SAVI image data September 2001.

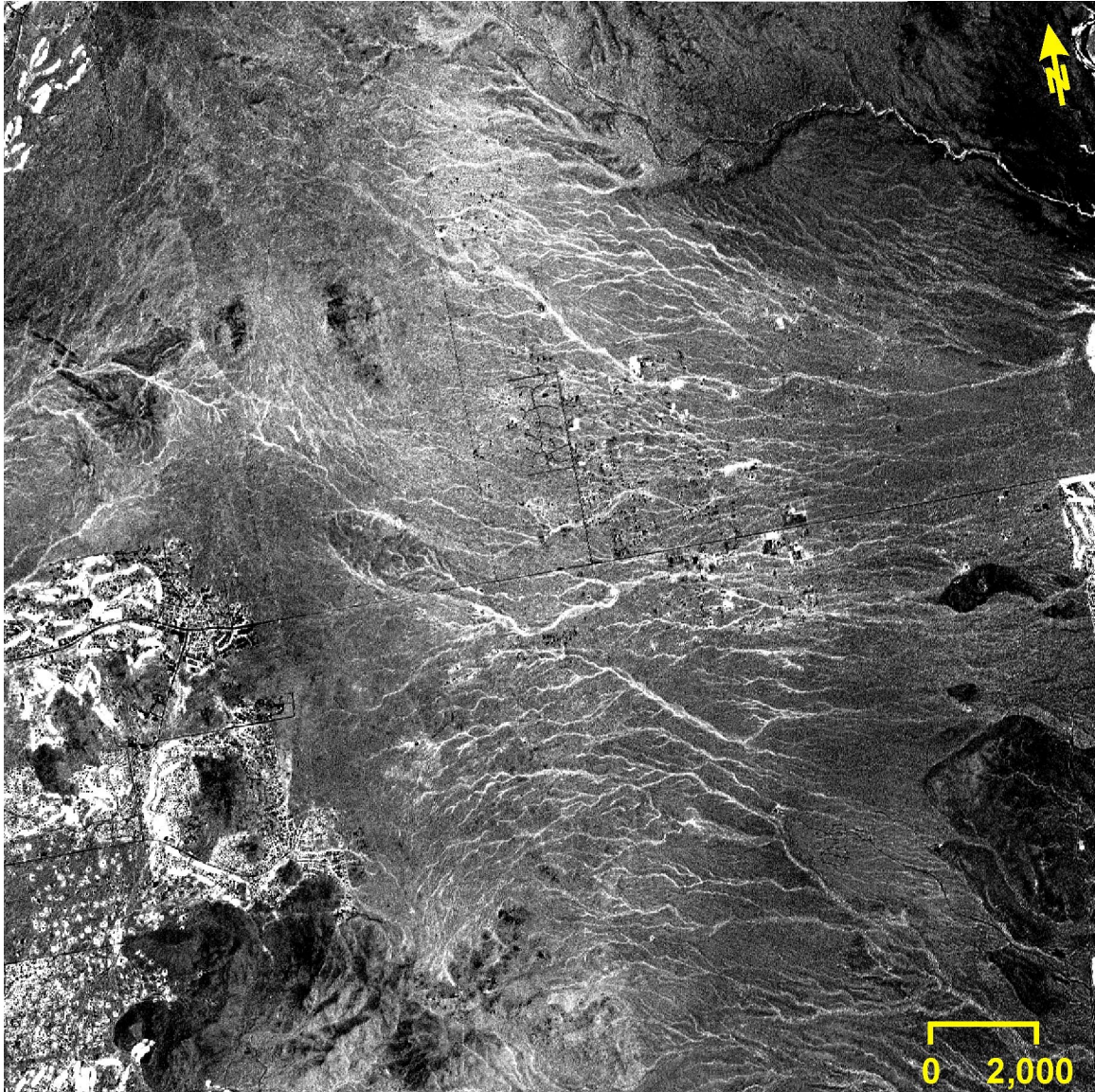


Figure 45. SAVI image data September 2002.

Image segmentation was used to automatically identify scarred areas. Results of ASTER NIR, ASTER SAVI and ASTER SWIR Band 4 utilizing the discontinuity adaptive Markov random field (DA-MRF) algorithm are illustrated in Figures 46, 47 & 48. The SWIR band produced the best image with fire scars outlined, however there is some confusion with surrounding urban areas being outlined as well.

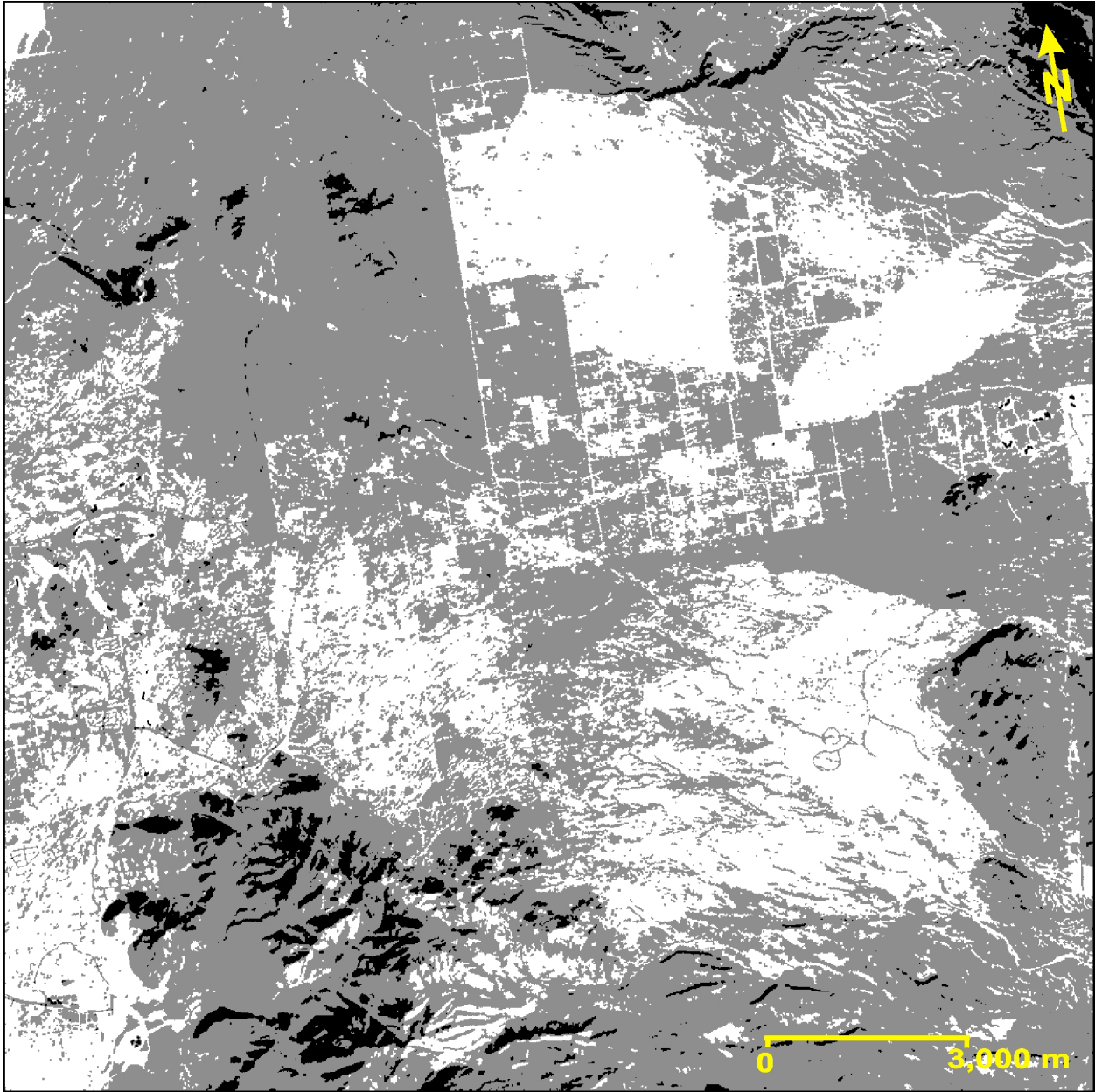


Figure 46. ASTER Segmentation images were used to automatically outline fire scarred areas. Segmentation using ASTER near infrared (band 3).

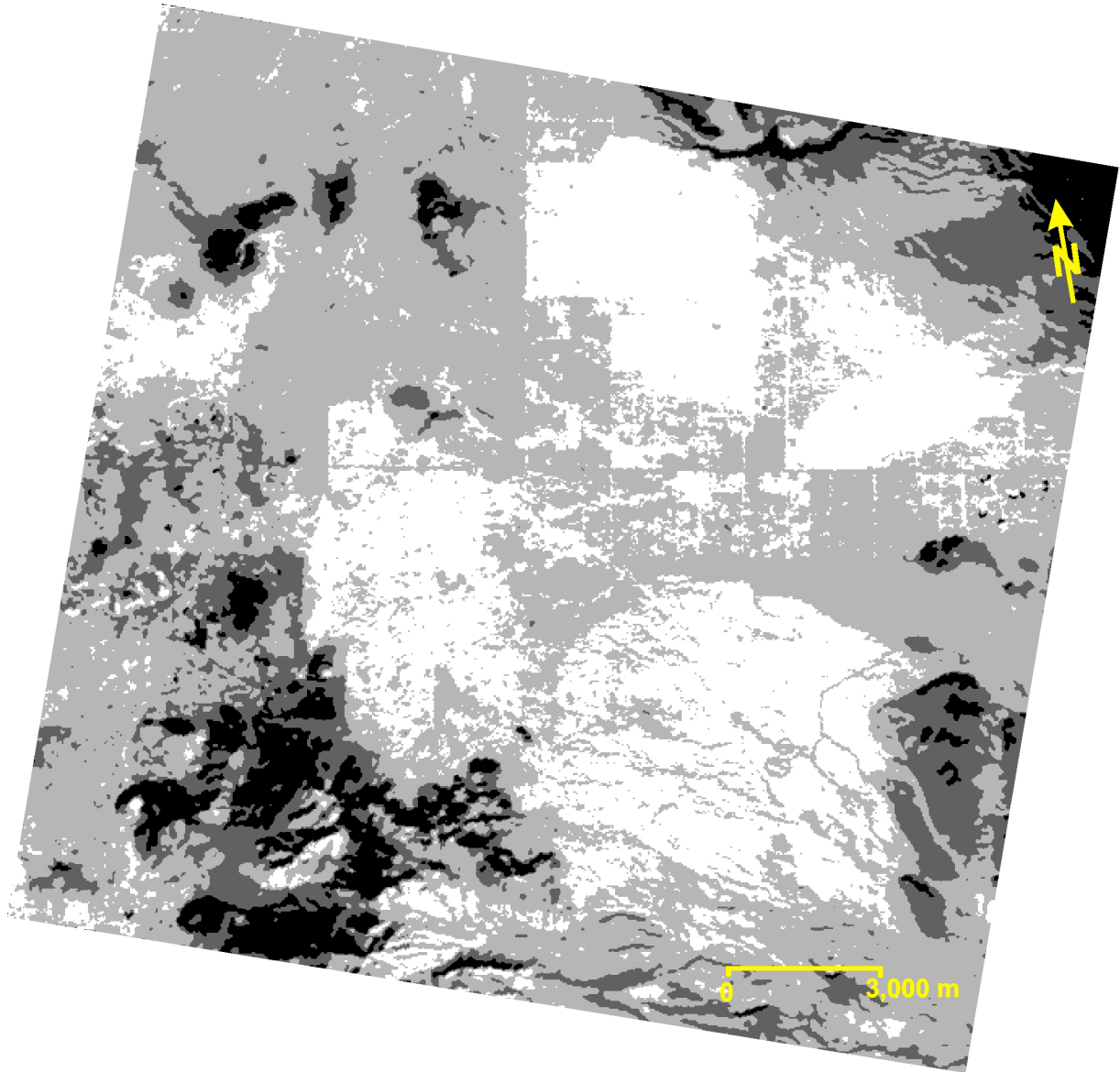


Figure 47. Segmentation image of fire scarred area. Image created from ASTER short wave infrared (band 4).

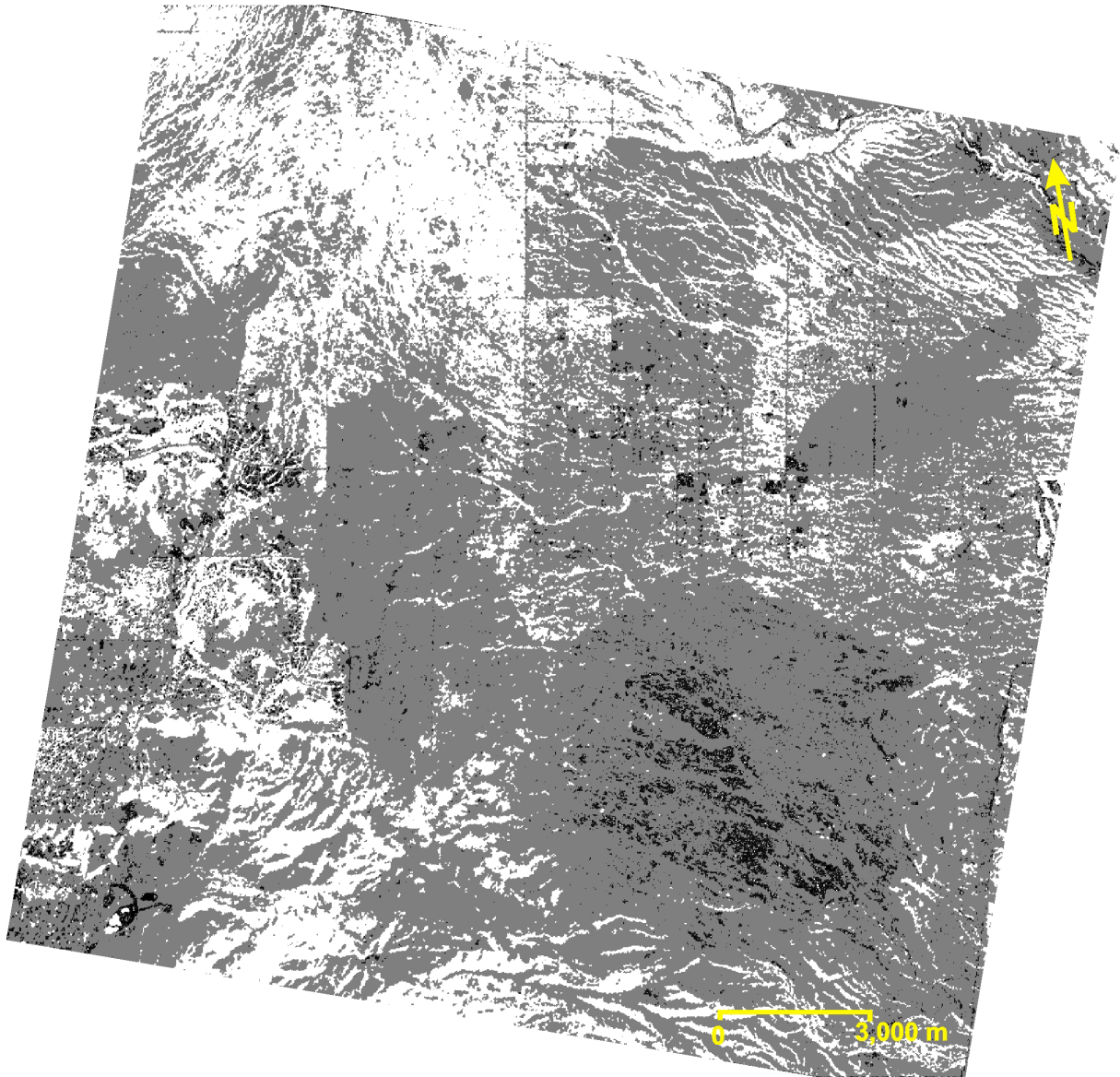


Figure 48. Image segmentation using ASTER SAVI.

Figure 49 is a class mask image produced using ENVI's change detection algorithm. Many of the pixels in the 1988 scars that were classed as burned in the 2000 image, are classed as urban in the 2002 image. A majority of the pixels in the more recent 1995 scars that were classed as burned in the 2000 image, were classed as desert vegetation in the 2002 image.

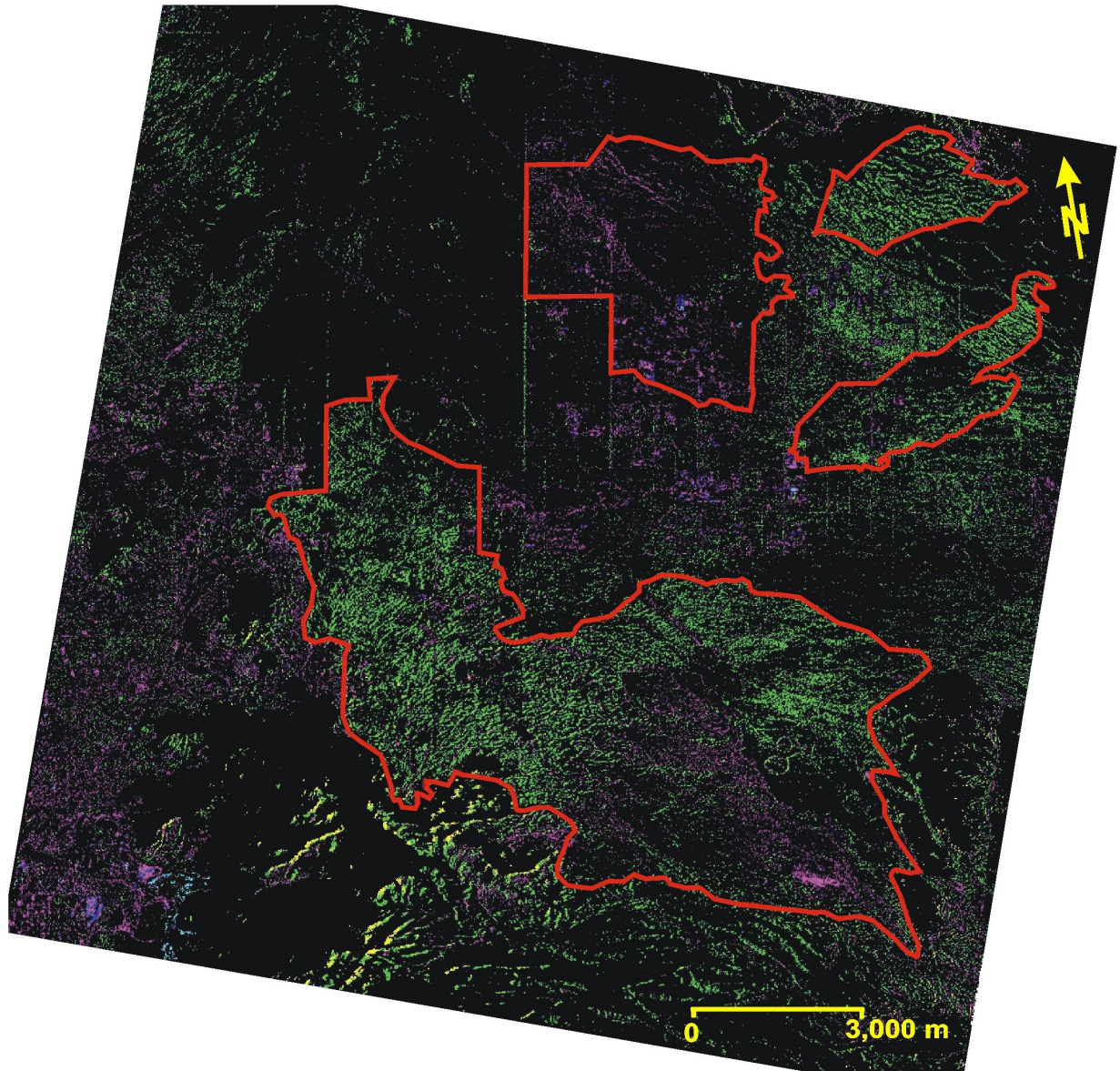


Figure 49. Change detection image illustrates the pixels that changed class from the initial image data set to the final image data set. Green pixels were originally burned pixels that were classed as unburned desert vegetation in the 2002 image. Magenta pixels were originally burned pixels that were classed as urban in the 2002 image.

The hazard map is composed of 3 layers: a classification image, roads, and urban areas. The ALRIS data sets for roads and urban areas are combined with the classification image from the decision tree classifier in ArcMap (Figure 50). A buffered urban coverage was created in ArcMap using a buffer distance of 200 feet. This coverage was converted to an ENVI vector file, and subjected to a decision tree classifier along with the resulting decision tree classification image developed earlier from fused data set 4. The final map characterizes exposed bedrock as “no risk” areas, unburned healthy desert vegetation as “low risk” areas, previously burned desert vegetation that is more than 200 meters from an urban center as a “medium risk” area, and regions that were previously burned, and within 200 meters of an urban center as a “high risk” area. This map facilitates the identification and characterization of fire scars as potential areas for future burns, and shows their proximity to urban areas. The user can also identify accessibility of burned areas to fire fighting crews, and the degree of slope which affects fire speed and intensity.

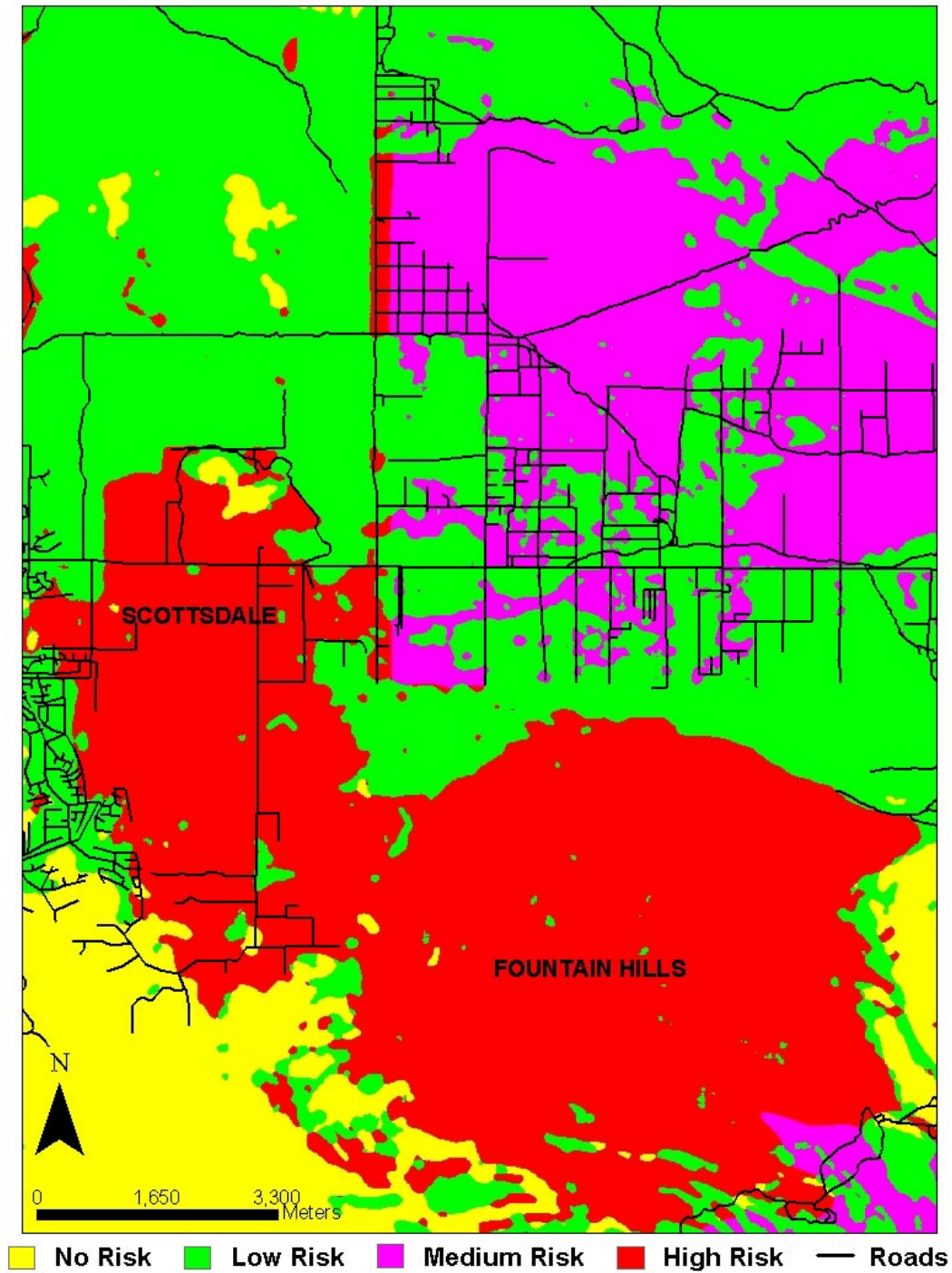


Figure 50. Hazard map produced using a buffered cities coverage intersected with the decision tree classification image, overlain with road data. No risk areas are defined by exposed bedrock, low risk areas are healthy unburned/not previously burned vegetation, medium risk areas are previously burned, but not within 200 meters of an urban center, and high risk areas are previously burned within 200 meters of an urban center.

DISCUSSION

5.1 Remote Sensing

Comparison of ASTER VNIR maximum likelihood classification with the Landsat TM classification reveals that ASTER's increased spatial resolution improved the ability of the classifier to characterize burned areas. Fusion of ASTER VNIR and SWIR data resulted in an increase in classification accuracy, however fusion with ASTER thermal data decreased the overall accuracy by approximately 10%. This decrease in accuracy is most likely due to the decreased spatial resolution of ASTER thermal data. A majority of the features in the image data are spectrally very similar (refer to Figure 27), resulting in classification errors where trying to distinguish between urban areas, burned desert vegetation, healthy desert vegetation, and bedrock. Fusion of ASTER data with Landsat tasseled cap and SIR-C data sets resulted in an increase in overall classification accuracy by approximately 3%. The brightness image from the tasseled cap data set, illuminates the albedo differences between less sparsely vegetated burned areas, and the healthier desert vegetation facilitating the separation of burned from unburned areas. Field surveys noted healthy vegetation in unburned areas was consistently taller than in burned areas. The addition of radar data enabled texture differences due to variation in vegetation height to be used to distinguish burned from unburned.

Incorporation of multiple raster and vector data sets in a multistage decision tree classifier outperformed the maximum likelihood routine. Integration of slope data resolved some of the areas where bedrock and burned pixels were confused. Using a vector data set of city locations, a SWIR texture image, and National Land Cover Data aided in the separation of urban areas from burned areas. This method is superior to the maximum likelihood classification for

this type of data because it is a nonparametric method that makes no assumptions regarding data distribution.

The attempt to relate fire scar age with vegetation vigor through the use of SAVI image data was unsuccessful. Statistically it is difficult to establish a threshold value that distinguishes between burned and unburned or senescing desert vegetation. Older scars tend to have higher mean values than more recent scars, however changes in overall values from year to year seemed to be more related to precipitation. Lack of preburn data, background reflectance from soils, shadows, and atmospheric conditions, combined with sparse vegetation coverage may contribute to the insensitivity of this index for assessing vegetation regrowth in a semi-arid region. Increasing the temporal and spectral resolution of the data sets would perhaps provide enough information to better analyze regrowth patterns.

The DA-MRF image segmentation method fairly accurately outlined fire scars in the study area. This edge detection algorithm worked best with ASTER SWIR data. Strong reflectance from soils and dry/dead vegetation in burned areas provided the best contrast for edge detection. This algorithm also has a smoothing function which homogenized small variations within boundaries, resulting in an automated characterization of burned areas. The algorithm seemed to work best in flat areas with little channelization, and fails in areas with increased slopes and channels. The Camp fire scar was not identified in this process because it is located in an area that is highly dissected.

Change detection analyses of maximum likelihood classification images from September 2000 (initial state) and September 2002 (final state) seemed to indicate more regrowth of desert vegetation in recently scarred areas compared to older scars. This might reflect the opportunistic invasion of grasses into recently burned areas. Fieldwork noted a 28% higher grass coverage in

the burned areas as opposed to the unburned areas, which supports the idea that grasses take advantage of the weakened ecosystem and open niche to invade. The change detection image also illustrates the encroachment of urbanization into previously burned areas. Most of the pixels that changed classes in the 1988 fire scars changed from burned pixels to urban pixels. This emphasizes the importance of accurately characterizing fire scarred areas, so urban planners and land management officials may accurately assess potential fire hazards related to human occupation of these areas, and the best land management practices that need to be implemented to avoid future fires.

Most fire hazard maps are developed for temperate and alpine ecosystems, and contain one or more of the following criteria: fuel load, slope, aspect, and vegetation moisture. One of the goals of this project was to develop a hazard map for this semi-arid region, however, many issues were encountered when attempting to compile this data. For example, Figure 22 shows slopes for the main study area, and on average they are less than 3 degrees. In general fire rate does not double until slopes are greater than 10 degrees (McArthur, 1973), therefore slopes in this area will have little effect on spread rate. The issue with aspect is similar to slope, in that little variation in topography results in very little difference in aspect. The study area is in a dry desert ecosystem composed of vegetation with low moisture content, therefore vegetation is always “dry” and changes in moisture content would have little bearing on fire hazard potential. Vegetation coverage in this region is by definition sparse, resulting in low fuel loading. This region did not qualify for any of the hazard criteria established by previous mapping projects. As a result, this project’s mapping effort culminated in the compilation of various data sources in order to establish an initial survey of potential fire hazards for this area. The most important coverage for this data set was the fire classification data. With the establishment of grass/fire

cycles in this region the biggest potential hazard for this area is whether or not it has burned in the past. The classification data shows burned areas, and when combined with other vector data sets such as urban areas, soils, and proximity to roads can begin to help city officials assess potential hazards.

5.2 Geomorphology

Initial field surveys seem to indicate increased drainage networks and channelization in burned areas compared to unburned areas. This result has also been documented by previous studies (Bull, 1997 and Schumm, 1977). The soil production and erosion study was inconclusive. Perhaps the rates at which these processes occur in this area are so slow as to not be observable at this scale of study, or maybe more data needs to be collected to adequately assess this process. Results from loss on ignition indicate more organic matter is present in the unburned catchments. Field data recorded 20% more vegetation in unburned areas, which seems to agree with this result. Grain size data from sediment traps is inconclusive. This could be due to the timing of the study, lack of robustness of the data set, and/or poor study design. Many of the traps are installed within channels rather than on hillslopes. This results in sediment deposition being controlled by the hydrodynamics of fluid flow within a channel, which is governed by more complex variables as compared to simple hillslope runoff. Previous studies suggest most erosion takes place immediately following a burn, and the major controlling factor on erosion is burn intensity. If the fire is not intense, there will be little to no increase in erosion. Perhaps the same study immediately following a fire would yield more conclusive results.

CONCLUSIONS AND FUTURE WORK

ASTER's increased spatial resolution and broader spectral range enabled a more detailed characterization study of fire scarred landscapes. Compared to the maximum likelihood technique, data fusion combined with a decision tree classifier provided a better method for distinguishing between feature classes that were consistently confused in previous work. (Brown, 1990; Chuvieco, 1988; Florsheim, 1991). Image segmentation using ASTER SWIR data provided a useful method for automatic detection of fire scars. The application of this type of algorithm is useful in that it can be utilized to initially screen scenes for potential scarred areas without the input of an analyst. More testing of this algorithm in other burned areas should be performed to fully assess its potential. Coding into ENVI, ArcGIS or Imagine would also facilitate the application and use of this routine. The collection of more information regarding vegetation regrowth in burned areas is very important, especially because the invasion of foreign grasses is potentially causing permanent changes to this ecosystem. Conducting field surveys of vegetation plots and utilizing higher spectral and temporal resolution remote sensing data combined with a radar data set would help to improve this investigation. Future work should also focus on improving the fire and flood hazard map for this area. Additional vector information such as proximity and travel time to the nearest fire fighting stations, and a better method for determining grass loading in burned areas would improve this map. More detailed field surveys with an electronic total station and GPS would provide better baseline data for assessing flood and erosion hazards, and determining how they relate to fire. The installation of more sediment traps on hillslopes rather than in channels, and continuous monitoring of traps over a longer period of time would also add to a better understanding of landscape dynamics as it relates to fire. Most fire research focuses on heavily forested environments in alpine, temperate

or tropical regions. However, brushy rangeland fires continue to be a threat, especially in the urban/wildland interfaces.

Characterization of fire scars through the integration of ASTER data with SIR-C, Landsat, and vector data sets provides a unique opportunity to map fire scarred landscapes in semi-arid regions. Integration of multi-temporal and multi-frequency data into a GIS resulted in a hazard map that can be utilized by urban planners and city officials to assess potential fire and flood hazard risks associated with the development of rural areas. Application of the remote sensing techniques developed in this project can be easily applied to other rapidly growing urban centers in semi-arid regions.

APPENDIX A

Appendix Title

BIBLIOGRAPHY

- Arrowsmith, J.R., 2002, Curvature and regolith calculations from the McDowell Mountain Park Rio burn fire site, Internet source:
http://kokkik.la.asu.edu/Fires_and_Floods/2002/curvandreg.pdf.
- Barbosa, P.M., Gregoire, J., and Pereira, J.M.C., 1999, An Algorithm for Extracting Burned Areas from Time Series of AVHRR GAC Data Applied at a Continental Scale: *Rem. Sens. Environ.*, v. 13, no. 4, p. 933-950.
- Benson, M.L., and Briggs, I., 1978, Mapping the extent and intensity of major forest fires in Australia using digital analysis of Landsat imagery: *Proc. of the Int. Symp. on Rem. Sens. for Obser. and Inv. of Earth Res.*, p. 1965-1980.
- Birkeland, P.W., 1999, *Soils and Geomorphology* (3rd ed.): New York, Oxford University Press, Inc.
- Brown, A.G., 1990, Soil erosion and fire in areas of Mediterranean vegetation; results from chaparral in Southern California, USA, and matorral in Andalucia, southern Spain: *Vegetation and erosion; processes and environments*, John Wiley & Sons.
- Bull, W.B., 1997, Discontinuous ephemeral streams: *Geomorphology*, v. 19, no. 3-4, p. 227-276.
- CPC (Climate Prediction Center-NOAA), 2000, Weekly Palmer drought and crop moisture Data Products Explanation, Internet Source:
http://www.cpc.ncep.noaa.gov/products/analysis_monitoring/cdus/palmer_drought/wpda_note.html.
- Chuvieco, E., and Congalton, R.G., 1988, Using cluster analysis to improve the selection of training statistics in classifying remotely sensed data: *Photogramm. Eng. Rem. Sens.*, v. 54, p. 1275-1281.
- Chuvieco, E., and Congalton, R.G., 1989, Application of remote sensing and geographic information systems to forest fire hazard mapping: *Rem. Sens. Environ.*, v. 29, p. 147-159.
- Chuvieco, E., and Salas, J., 1996, Mapping the spatial distribution of forest fire danger using GIS: *International Journal of GIS*, v. 10, no. 3, p. 333-345.
- CLIMVIS(a) (Climatic Visualization System) - Global Historical Climatology Network. Internet source: <<http://www5.ncdc.noaa.gov/cgi-bin/climvis/ghcn/tempV2.sh>> via
<http://www.ncdc.noaa.gov/ol/climate/climatedata.html>

- CLIMVIS(b) (Climatic Visualization System) - Global Historical Climatology Network, National Climatic Data Center (NCDC). Internet source: <<http://www5.ncdc.noaa.gov/cgi-bin/ghcn/precip.ghcn.cgi>> via <http://www.ncdc.noaa.gov/ol/climate/climatedata.html>
- CLIMVIS(c) (Climatic Visualization System) - Global Historical Climatological Network, National Climatic Data Center (NCDC). Climate Division Data: Arizona, section 7: Temperature, Precipitation, PDSI, PDHI data. Internet source: <http://www.ncdc.noaa.gov/onlineprod/drought/xmrg3.html>
- Congalton, R.G. and Green, K., 1999, *Assessing the Accuracy of Remotely Sensed Data: Principles and Practices*: Boca Raton, Lewis Publishers.
- D'Antonio, C.M.a.V., P.M., 1992, Biological invasions by exotic grasses, the grass/fire cycle, and global change: *Annual Review of Ecology and Systematics*, v. 23, p. 63-87.
- Diaz-Fierros, F., Benito, R.E. and Pertez, M.R., 1987, Evaluation of the U.S.L.E. for the prediction of erosion in burned forest areas in Galicia (N.W. Spain): *CATENA*, v. 14, p. 189-199.
- Dimmitt, M.A., 2000, *A Natural History of the Sonoran Desert: Biomes & Communities of the Sonoran Desert Region*: Tucson, AZ, Arizona Sonora Desert Museum Press, p. 3-18.
- Doorn, P.L., Pewe, T.L., 1991, *Geologic and gravimetric investigations of the Carefree Basin, Maricopa County, Arizona*: Arizona Geological Survey Special Paper, v. 8, p. 187.
- Esque, T., and Schwalbe, C., 2000, *Non-native Grasses & Fires Create Double Jeopardy*, Department of the Interior.
- Eva, H.D., and Lambin, E.F., 1998, Burnt area mapping in Central Africa using ATSR data: *Int. J. Remote Sens.*, v. 19, no. 18, p. 3473-3497.
- Florsheim, J.L., Keller, E.A., and Best, D.W., 1991, Fluvial sediment transport in response to moderate storm flows following chaparral wildfire, Ventura County, Southern California: *Geol. Soc. Amer. Bull.*, v. 103, p. 504-511.
- Freeman, A., Cruz, J., Alves, M., Chapman, B., Shaffer, S., and Turner, E., 1995, SIR-C Data Quality and Calibration Results: *IEEE Trans. Geosci. Rem. Sens.*, v. 33, no. 4.
- Gerlach, T., 1967, Hillslope troughs for measuring sediment movement: *Rev. Geomorphol. Dyn.*, v. 17, p. 173.
- Gimeno-Garcia, E., Andreu, V., and Rubio, J.L., 2000, Changes in organic matter, nitrogen, phosphorus and cations in soil as a result of fire and water erosion in a Mediterranean landscape: *European Journal of Soil Science*, v. 51, p. 201-210.

- Goudie, A., 1990, *Geomorphological techniques* (second ed.): London, Unwin Hyman.
- Grissino-Mayer, H.D., and Swetnam, T.W., 2000, Century-scale climate forcing of fire regimes in the America Southwest: *The Holocene* 10, no. 2, p. 213-220.
- Hendricks, D.M., 1985, *Arizona Soils*, University of Arizona College of Agriculture.
- Huete, A.R., 1988, A soil-adjusted vegetation index (SAVI): *Rem. Sens. Environ.*, v. 25, no. 295-309.
- Husson, A., 1982, Exemple d'utilisation de la Teledetection en Francd: la cartographie des feux de foret, in *Le Systeme SPOT d'Observation de la Terre: L'AQT/SFPT*: Montreal, 15-26 p.
- Jakubauskas, M.E., Lulla, K.P. and Mausel, P.W., 1990, Assessment of vegetation change in a fire-altered landscape: *Photogramm. Eng. Rem. Sens.*, v. 56, p. 371-377.
- Kutiel, P., Lavee, H., Segev, M., and Benyamini, Y., 1995, The effect of fire-induced surface heterogeneity on rainfall-runoff-erosion relationships in an eastern Mediterranean ecosystem, Israel: *CATENA*, v. 25, no. 1-4, p. 77-87.
- Lavee, H., Kutiel, P., Segev, M., and Benyamini, Y., 1995, Effect of surface roughness on runoff and erosion in a mediterranean ecosystem: the role of fire: *Geomorphology*, v. 11, no. 3, p. 227-234.
- Lillesand, T.M. and Kiefer, R.W., 1994, *Remote Sensing and Photo Interpretation* (3 ed.): New York, John Wiley & Sons.
- McArthur, A.G., 1973, *Grassland Fire Danger*: <http://www.esb.act.gov.au/firegreak/grass-behave.html>.
- McAuliffe, J.R., 1994, Landscape evolution, soil formation, and ecological patterns and processes in Sonoran Desert bajadas: *Ecol. Monogr.*, v. 62, no. 111-148.
- Menges, C.M., and Pearthree, P.A., 1989, Late Cenozoic tectonism in Arizona and its impact on regional landscape evolution: *Arizona Geological Society Digest*, v. 17, no. *Geologic Evolution of Arizona*, p. 649-680.
- Pagano, T.C., 1999, *Southwest Climate in a Nutshell*, Climate Assessment for the Southwest.
- Patterson, M.W., and Yool, S.R., 1998, Mapping fire-induced vegetation mortality using Landsat Thematic Mapper data: A comparison of linear transformation techniques: *Rem. Sens. Environ.*, v. 65, p. 132-142.
- Pereira, J.M.C., 1999, *A Comparative Evaluation of NOAA/AVHRR Vegetation Indexes for*

- Burned Surface Detection and Mapping: *IEEE Trans. Geosci. Rem. Sens.*, v. 37, no. 1, p. 217-226.
- Ramsey, M.S., and Arrowsmith, J.R., 2001, Mitigating Future fire and flood hazards in arid urban regions: Initial analysis of brush fire scars with the new ASTER instrument: *EOS Trans.*, AGU, v. 81, no. abstract, p. F549.
- Reeves, M.C., 1999, Mapping Sonoran Desert Vegetation of the McDowell Mountains Using Hyperspectral Imagery: Tempe, Arizona State University, M.S.
- Rouse, J.W., Haas, R.H., Schell, J.A., Deering, D.W., 1974, Monitoring vegetation systems in the Great Plains with ERTS: Proceedings of the Third Earth Resources Technology Satellite-1 Symposium, no. NASA SP-351, p. 301-317.
- Schumm, S.A., 1977, *The Fluvial System: Drainage Pattern Evolution*: New York, John Wiley, 411-432 p.
- Shakesby, R.A., Walsh, R.D., Coelho, O.A., 1991, New Developments in techniques for measuring soil erosion in burned and unburned forested catchments: *Portugal Z. Geomorph. N.F.*, v. 83, no. suppl.-Bd, p. 161-174.
- Singer M.J. and Janitzky, P., 1986, Field and laboratory procedures used in a soil chronosequence study: *United States Geological Survey Bulletin*, v. 648.
- Skotnicki, S.J., 1996, *Geologic Map of Portions of the Fort McDowell and McDowell Peak Quadrangles, Maricopa County, Arizona*: Arizona Geological Survey Open-File-Report, v. 96-11.
- Stefanov, W.L., Ramsey, M.S., and Christensen, P.R., 2001, Monitoring the urban environment: An expert system approach to land cover classification of semiarid to arid urban centers: *Rem. Sens. Environ.*, v. 77, p. 173-185.
- Story, M., and Congalton, R., 1986, Accuracy assessment: A user's perspective.: *Photogramm. Eng. Rem. Sens.*, v. 52, no. 3, p. 397-399.
- Tanaka, S., Kimura, H., and Suga, Y., 1983, Preparation of 1:25,000 Landsat map for assessment of burnt area on Etajima Island: *Int. J. Remote Sens.*, v. 4, no. 1, p. 17-31.
- Vincent, R.K., 1997, *Fundamentals of Geological Environmental Remote Sensing*: Prentice Hall Series in Geographic Information Science: Upper Saddle River, Prentice Hall.
- Wentz, E., Anderson, S., Stefanov, W., and Briggs, J., 2001, Desert Fire History and Effects on the Phoenix, Arizona, Metropolitan Area: Proceedings of 1st IEEE/ISPRS Joint Workshop on Remote Sensing and Data Fusion over Urban Areas.
- Yamaguchi, Y., Kahle, A.B., Tsu, H., Kawakami, T., Pniel, M., 1998, Overview of the

Advanced Spaceborned Thermal Emission And Reflectance Radiometer: IEEE Trans. Geosci. Rem. Sens., v. 36, p. 1062-1071.

Yool, S.R., Eckhardt, D.W., and Cosentino, M.J., 1985, Describing the brushfire hazard in southern California: Anal. Assoc. Am. Geograph., v. 75, p. 431-442.